DEVELOPMENT AND IN VITRO CHARACTERIZATION OF THREE DIMENSIONAL BIODEGRADABLE SCAFFOLDS FOR PERIPHERAL NERVE TISSUE ENGINEERING

A Thesis Submitted to the College of

Graduate Studies and Research

in Partial Fulfillment of the Requirements

for the Degree of Doctor of Philosophy

in the Department of Biomedical Engineering

University of Saskatchewan

Saskatoon

By

Ning Zhu

PERMISSION TO USE

In presenting this thesis in partial fulfilment of the requirements for a Postgraduate degree from the University of Saskatchewan, I agree that the Libraries of this University may make it freely available for inspection. I further agree that permission for copying of this thesis in any manner, in whole or in part, for scholarly purposes may be granted by the professor or professors who supervised my thesis work or, in their absence, by the Head of the Department or the Dean of the College in which my thesis work was done. It is understood that any copying or publication or use of this thesis or parts thereof for financial gain shall not be allowed without my written permission. It is also understood that due recognition shall be given to me and to the University of Saskatchewan in any scholarly use which may be made of any material in my thesis.

Requests for permission to copy or to make other use of material in this thesis in whole or part should be addressed to:

Head of the Division of Biomedical Engineering

University of Saskatchewan

Saskatoon, Saskatchewan S7N 5A9

Canada

ABSTRACT

Tissue engineering emerges nowadays to seek new solutions to damaged tissues and/or organs by replacing or repairing them with engineered constructs or scaffolds. In nerve tissue engineering, scaffolds for the repair of peripheral nerve injuries should act to support and promote axon growth following implantation. It is believed that substantial progress can be made by creating scaffolds from biomaterials, with growth-promoting molecules and spatially-controlled microstructure. To this end, this research aims to develop three dimensional (3D) scaffolds for peripheral nerve tissue regeneration by focusing on studies on the axon guidance, development and characterization of a novel 3D scaffold, and visualization of scaffolds by means of synchrotron-based diffraction enhanced imaging (DEI).

Axon guidance is one of crucial considerations in developing of nerve scaffolds for nerve regeneration. In order to study the axon guidance mechanism, a two dimensional (2D) grid micropatterns were created by dispensing chitosan or laminin-blended chitosan substrate strands oriented in orthogonal directions; and then used in the *in vitro* dorsal root ganglion (DRG) neuron culture experiments. The results show the effect of the micropatterns on neurite directional growth can preferentially grow upon and follow the laminin-blended chitosan pathways.

A novel 3D scaffold was developed for potential applications to peripheral nerve tissue engineering applications. The scaffolds were fabricated from poly L-lactide (PLLA) mixed with chitosan microspheres (CMs) by using a rapid freeze prototyping (RFP) technique, allowing for controllable scaffold microstructure and bioactivities

protein release. The scaffold characterization shows that (1) the mechanical properties of the scaffolds depend on the ratio of CMs to PLLA as well as the cryogenic temperature and (2) the protein release can be controlled by adjusting the crosslink degree of the CMs and prolonged after the CMs were embedded into the PLLA scaffolds. Also, the degradation properties of the scaffolds were investigated with the results showing that the addition of CMs to PLLA can decrease the degradation rate as compared to pure PLLA scaffolds. This allows for another means to control the degradation rate.

Visualization of polymer scaffolds in soft tissues is challenging, yet essential, to the success of tissue engineering applications. The x-ray diffraction enhanced imaging (DEI) method was explored for the visualization of the PLLA/CMs scaffolds embedded in soft tissues. Among various methods examined, including conventional radiography and in-line phase contrast imaging techniques, the DEI was the only technique able to visualize the scaffolds embedded in unstained muscle tissue as well as the microstructure of muscle tissue. Also, it has been shown that the DEI has the capacity to image the scaffolds in thicker tissue, and reduce the radiation doses to tissues as compared to conventional radiography.

The methods and results developed/obtained in this study represent a substantial progress in the development and characterization of 3D scaffolds. This progress forms a basis for the future tests on the scaffolds as applied for peripheral nerve injuries.

ACKNOWLEDGEMENTS

I would like to express my heart-felt gratitude to my supervisors, Prof. Daniel Chen and Prof. Dean Chapman, for their excellent guidance and tremendous support during my Ph.D. study at the University of Saskatchewan. I also would like to extend my appreciation to Prof. Chris Zhang, Prof. David Cooper, Prof. Catherine Niu, and Prof. Madan M. Gupta serving as members of my Ph.D. advisory committee and providing me with valuable comments.

I especially thank Prof. David Schreyer, Dr. George Belev, Mrs. Ruilin Zhai, Mrs. Tangyne Berry, and Mr. Doug Bitner, who provided me with numerous valuable advices and technical support in experiments. Also, my thanks go to some other former or current students in the Tissue Engineering Research Group, including Minggan Li, Xin Yan, Yijing Guang, Ning Cao, Mindan Wang, Peng Zhai, Ajay Rajaram, Christopher James Little, Huishu Hou, Chenglin Liu, Zohreh Izadifar**,** and Nahshon Bawolin, for their help and discussion.

I gratefully acknowledge the financial support from the Division of Biomedical Engineering, the Saskatchewan Health Research Foundation (SHRF), and the CIHR Training grant in Health Research Using Synchrotron Techniques Fellowship. I also acknowledge the support from the Canadian Light Source, where I imaged and examined the scaffolds fabricated in my study.

Last, but not least, I thank my parents and wife for their support, love, patience, and understanding.

Dedication

To my wife, Laura, and my daughter, Emma

TABLE OF CONTENTS

LIST OF TABLES

LIST OF FIGURES

CHAPTER 1
INTRODUCTION

1.1 Peripheral nerve tissue engineering (NTE)

Peripheral nerve system (PNS) injuries can lead to the lifetime loss of neurological function and approximately 200,000 nerve repair procedures are performed annually in the United States alone [1]. After peripheral nerve injury (PNI), the distal portion of the nerve undergoes degeneration, in which severed axons die and Schwann cells shed their myelin [2], leading the loss of neurological function. On the other hand, the proximal segment may be able to regenerate and reestablish nerve function, depending upon the length of injury gap. If the gap is long, the PNI must be surgically treated. Currently, the "gold standard" of clinical treatments for the long-gap PNI uses a donor nerve from a different location to bridge the severed nerve. However, the method still is limited as it requires two incisions for donor harvest and repair thus causing donor site morbidity and the functional recovery from this method is always not complete [3]. Peripheral NTE aimed at developing nerve conduit scaffolds are a promising approach to promote functional recovery of the injured nerves [4, 5].

Figure 1.1 schematically illustrates the concepts of PNI and its repair by means of a conduit scaffold. In the literature, non-nerve autologous tissues such as blood vessels [6, 7] and skeletal muscles [8] have been used as conduits to promote axon regeneration and functional recovery. As harvested from the patients themselves, the autologous tissues are immunologically compatible, thus possessing optimal donor-host integration characteristics. The use of autologous tissues also requires a second surgery, in addition to the shortcoming of incompatibility in terms of size or

dimension. As alternatives to autologous tissues, a number of non-autologous biological tissues have been reported for peripheral nerve repair. Acellular non-autologous nerve grafts obtained from animals were used as a conduits [9, 10]. Although extracellular matrix (ECM) based nerve conduits, which are plentiful, are able to promote cellular attachment, migration and axon extension, they present risks with immunogenic mismatching and possible transmission of disease [11]. Non-biodegradable nerve conduits have also been used to bridge peripheral nerve lesions. Non-biodegradable nerve conduits are typically made from non-biodegradable materials such as silicone [12] and polytetrafluoroethylene (PTFE) [13]. Numerous trials have shown that, owing to unmatched mechanical properties between non-biodegradable materials and nerve tissues, the implants may lead to chronic nerve compression, decreased neovascularization, and increased scarring [14].

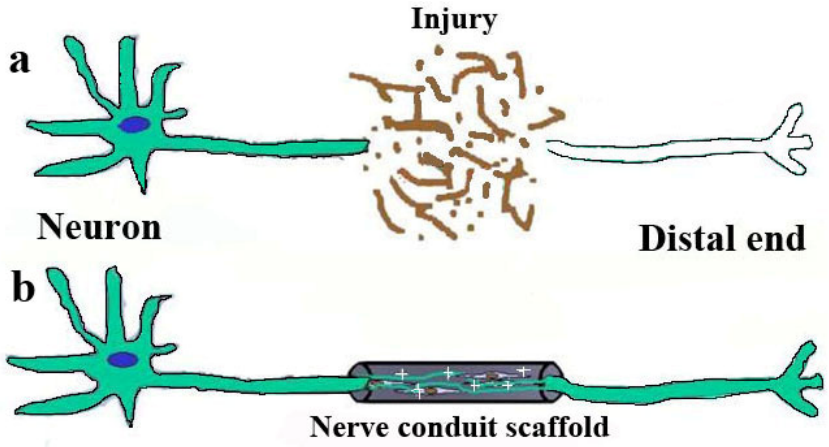

Figure 1.1 (a) Schematic of peripheral nerve injury and (b) regeneration by using a nerve conduit scaffold.

Currently, biodegradable nerve conduit scaffolds has been emerging and showing promise in peripheral NTE. Due to their biodegradability, the scaffolds degenerate *in vivo* and are eventually bioabsorbed by the surrounding tissues at the implanted site.

In contrast, non-degradable materials tend to accumulate toxic levels of waste products and even constrict the nerve, thus impairing nerve function once regenerative axons have traversed the gap [15]. While previous studies show the potential of the biodegradable scaffold, numerous issues must be addressed before they can be applied clinically. The present study is aimed at addressing some of the issues, particularly focusing on the axon guidance and the development and characterization of biodegradable scaffolds in NTE.

1.2 Brief introduction to the development of biodegradable scaffolds for NTE

1.2.1 Requirements imposed on the biodegradable NTE scaffolds

Generally speaking, scaffolds for peripheral nerve regeneration should mimic the structure and properties of native nerves so as to support and direct the process of neo-tissue formation. Ideally, a nerve conduit scaffold should have the following properties and characteristics [16-18], as illustrated in Figure 1.2.

(1) Biocompatibility: the scaffold materials should have a high affinity for cells to attach, differentiate, and proliferate, but not induce any adverse response.

(2) Microstructure: scaffolds should possess interconnected porous microstructure with appropriate pore sizes to favor tissue integration and vascularization. The porous microstructure also contributes significantly to the diffusion of nutrients and metabolic wastes.

(3) External shape: scaffolds should have a nerve conduit shape allowing the regenerative nerves across the scaffolds to reach the distal end of the severed nerve.

(4) Mechanical properties: scaffolds should possess adequate mechanical properties to match the intended site of implantation.

(5) Biodegradablility: the degradation rate of the scaffolds should be controllable and appropriate with the regeneration process of new nerve tissues.

(6) Axon guidance cues: a nerve conduit scaffold should carry bioactive molecules, such as growth factors, and provide directional cues for axon guidance.

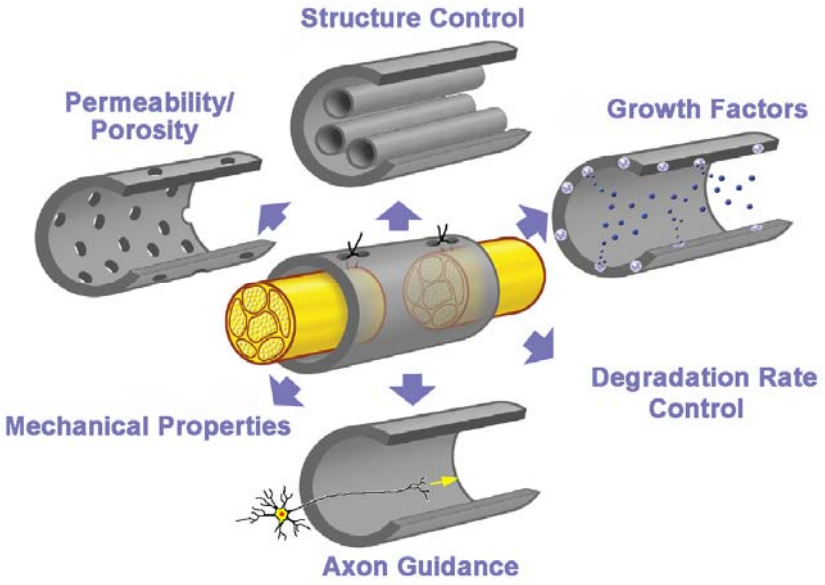

Figure 1.2 Schematic illustration of an ideal nerve conduit scaffold for peripheral nerve regeneration (modified from [19]).

1.2.2 Biodegradable biomaterials for NTE scaffolds

A wide range of biodegradable biomaterials has been used in the development of nerve tissue scaffolds. Generally, these biomaterials can be classified into two categories: synthetic and naturally derived materials.

(1) Synthetic materials:

Synthetic materials have many advantages, including (a) they have known compositions and can be designed to minimize the immune response; and (b) a range

of mechanical properties and degradation rates of the synthetic polymers can be tailored to match the requirements of a specific tissue engineering application. Figure 1.3 shows the chemical structures of the common synthetic polymers used in nerve tissue which are briefly reviewed as follows.

Poly (lactic acid) or poly lactide (PLA) has been proved to be the most attractive and useful category of biodegradable polyesters, which can be prepared by both direct condensation of lactic acid or the ring-opening polymerization of the cyclic lactide dimer [20]. PLA can be semi-crystalline or totally amorphous, depending on the stereopurity of the polymer backbone. PLA undergoes hydrolytic degradation with the random scission of the ester backbone. It degrades into lactic acid, which is a normal human metabolic by-product and can be resorbed by human bodies [21]. As such, PLA has been approved by the United States Food and Drug Administration and widely used in the development of commercial bioabsorbable biomedical devices, such as bone screws [22], stents [23], sutures [24], etc. Based on the chiral nature of lactic acid, PLA has been found in two stereoisomeric forms: L-lactide and D-lactide. Poly (L-lactide) (PLLA) is a product resulting from polymerization of L-lactide which is the natural and most common form of the acid. PLLA not only possesses good mechanical strength and biodegradation properties, but also can be easily processed by various conventional processing techniques. Therefore, PLLA has been popularly used to build tissue scaffolds. With regard to PNI repair, PLLA nerve conduit scaffolds have been successfully applied and reported in the literature [25, 26]. Also studies of PLLA have also been conducted to investigate into neurite alignment [27],

cytocompatibiliy [28, 29], and material modification promoting neurite outgrowth [30, 31].

Besides PLA, other synthetic polymers applied in NTE include Poly (glycolic acid) (PGA), poly (lactide-co-glycolide) (PLGA), polycaprolactone (PCL), and poly-3-hydroxybutyrate (PHB) (Figure 1.3). PGA is the simplest linear, aliphatic polyester [32]. It is a high crystalline polymer and therefore exhibits excellent mechanical properties. Due to its slow degradation rate, the copolymerization of glycolic acid (GA) and lactic acid (LA) - PLGA has been investigated for improvement. In NTE, PLGA has been applied in the fabrication of scaffolds [33, 34] or microspheres for drug delivery [35]. PCL is a semi-crystalline polyester and has low tensile strength, but an extremely high elongation at breakage [36]. In NTE, PCL has been studied to build nerve conduit scaffolds either alone [37] or in combination with other materials, such as chitosan [38], gelatin [39], and collagen [40]. PHB has been studied as a nerve conduit scaffold material in NTE applications for the last decade [41-43]. PHB can be degraded in either a enzymatic or non-enzymatic environment. PHB is considered to be moderately resistant to degradation *in vitro* and *in vivo* compared to PLA and PLGA [44].

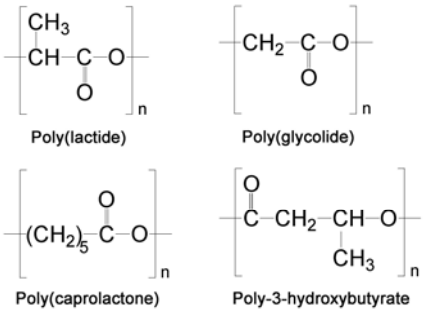

Figure 1.3 Chemical structures of common synthetic biodegradable polymers used in peripheral nerve tissue engineering.

(2) Natural materials:

Natural materials possess many properties that make them attractive for NTE applications, which includes excellent biocompatibility and similar properties to the soft tissues being replaced. However, natural materials must be purified to reduce the risk of foreign body response upon implantation. Homogeneity of products from different source locations can be another issue with natural materials. Several natural polymers that have been typically studied in NTE are reviewed as follows.

Chitosan is a deacetylated derivative of chitin found in arthropod exoskeletons. It is the second most abundant biopolymer in nature. Chitosan is a linear polysaccharide consisting of β(1→4) linked D-glucosamine residues with a variable number of randomly located *N*-acetyl-glucosamine groups [45]. The degree of deacetylation (DD) of chitosan is an important characteristic which greatly affects its biological properties [46] and physicochemical properties (e.g. crystallinity, swelling ratio, and mechanical property) [47, 48]. The degradation behaviors of chitosan are also dependent on the DD [49, 50] and chitosan can quickly degrade in the presence of lysozyme [51]. Chitosan is a attractive biomaterial in biomedical applications due to its biocompatibility, biodegradability, low immunogenicity and low cost [52, 53]. Chitosan scaffolds have been explored in numerous tissue engineering applications [54] especially in nerve regeneration [55, 56]. Furthermore, one of chitosan's promising features is its cationic nature, which allows for forming ionic complexes with various anionic substances in an acidic environment and dissociating a portion of the complexes in a physiological solution (pH 7.4). This characteristic is beneficial to

carry and accumulate bioactive molecules for their sustained release from the chitosan matrix [57]. Therefore, chitosan has also been widely used as a bioactive molecule carrier for neurotrophins release during nerve tissue regeneration [58, 59].

Other natural materials applied in NTE include collagens, alginate, and fibroin. Collagens are the most abundant protein present in the human body being the major component of skin and other musculoskeletal tissues. It is among the most popular biomaterials in various tissue engineering applications [60]. Collagen conduits have proven to successfully support axon regeneration in a degree similar to that supported by autografts [61-63]. Collagens have also been used, in a form of hydrogel, with other biomaterials to promote axon regeneration [64, 65]. Alginate is a linear polysaccharide obtained from seaweed or algae [66]. Alginate gels have good cell-affinity and can enhance cell survival and growth. As such the polymer can be used to develop cell-binding hydrogels for use as scaffolds for tissue engineering [67]. In NTE, scaffolds made from alginate are capable of maintaining the viability and function of a variety of neural cell types [68]. Alginate-based scaffolds encapsulated with nerve support cells have been reported for peripheral nerve regeneration [69]. Fibroin from the silkworm, which is another class of natural fibers [70], has been demonstrated to have good biocompatibility with peripheral nerve cells *in vitro* [71, 72].

1.2.3 Scaffold fabrication techniques

A number of conventional techniques have been widely used to process synthetic

and natural biodegradable biomaterials into NTE scaffolds, including solvent-casting and particulate-leaching [73], gas foaming [74], phase separation [75], melt molding [76], freeze drying [77], and electrospinning [78]. The solvent-casting and particulate-leaching techniques can be used to fabricate porous scaffolds with a porosity up to 93% and an average pore diameter up to 500 μm [79]. However, these techniques are limited to produce thin membranes up to 3 mm in thickness [80]. The gas foaming process creates a porous structure by using gas-foaming agents, such as CO_2 and nitrogen [81], water [82], or fluoroform [83]. The process is organic solvent free; and its main drawback is possibly yielding a largely unconnected porous structure and a non-porous external surface [84]. Using phase separation [85] or freeze dry techniques [86, 87], the micro- and macro-structure of the scaffolds can be controlled by varying processing parameters, such as polymer concentration, quenching temperature, and rate. As these processes are carried out under relatively-low temperatures, they allow for the incorporation of bioactive molecules to scaffolds during their fabrication. Melt molding is a non-solvent fabrication process, but needs a high processing temperature for operation and as such, it would not allow for incorporation of with bioactive molecules [88]. The electrospinning technique has been employed nowadays to fabricate porous scaffolds with nanofibrous microstructure, thus possibly mimicking the structure and biological functions of the natural extracellular matrix [89]. Concerns about this technique include the uncontrollable collection of fibers during the process, and the relatively-small space formed among the fibers which might limit cell penetration in the scaffold.

As an alternative to conventional scaffold fabrication methods, a group of rapid prototyping techniques (RP) has recently been developed in tissue engineering [90, 91]. RP techniques utilize the layer-manufacturing strategy to fabricate three-dimensional (3D) scaffolds with the help of computer-assisted-design (CAD) and computer-assisted-manufacturing (CAM) techniques. RP allows better control of scaffold internal structure and external shape compared to conventional fabrication techniques [92, 93]. RP-based scaffold fabrication can be classified three types: liquid-based, solid-based, and powder-based, according to the properties of the scaffold biomaterials used. The main RP processes applied in tissue scaffold fabrication include stereolithography [94], selective laser sintering [95], fused deposition modeling [96], and 3D printing [97]. Recently, RP techniques also have shown their capacities to incorporate living cells [98, 99] and growth factors [100] into the scaffolds during the fabrication process thus building bio-mimetic tissue scaffolds.

1.2.4 Scaffolds as carriers for drug delivery

In NTE, some proteins play an important role as bioactive factors in enhancing nerve regeneration across peripheral nerve gaps which include neurotrophins and neurostimulatory ECM proteins [18]. Research has shown that these factors have influence on neural development, survival, outgrowth, and branching [101]. The most common growth factors used to promote neural tissue regeneration are neurotrophins such as nerve growth factor (NGF), brain derived neurotrophic factor (BNDF),

neurotrophin-3 (NT-3), and neurotrophin-4/5(NT-4/5). Other growth factors that have been studied for their ability to promote nerve regeneration include ciliary neurotrophic factor (CNTF), glial cell line-derived growth factor (GDNF), transforming growth factor β (TGF-β), and acidic and basic fibroblast growth factor (aFGF, bFGF) [101, 102]. Furthermore, neurostimulatory ECM proteins, such as laminin and fibronectin, can provide stimulatory cues for neurite extension [103].

The local delivery of these proteins is desirable due to the fact that the proteins often have short half-lives and multiple biological effects that present the risks of potential systemic toxicity [104]. As a local delivery method, scaffolds carried with bioactive molecules have shown promise to promote and guide cell-induced tissue regeneration through a control of the local microenvironment in which the molecules can be exposed at the desired site and be released with sufficient local dose in the required time frame [102]. The proteins can be directly interspersed within the scaffolds or encapsulated in micro- or nano- particles interspersed in the scaffold structure. The proteins released from the micro- or nano- particles in scaffolds could overcome the disadvantages of direct release from scaffolds, including poor release rate control and the loss of growth factor bioactivity [105]. To mimic the natural biological process, nerve conduit scaffolds should not be limited to a single neurotrophin or ECM protein, but rather should release multiple bioactive molecules at an optimized ratio, each at a physiological dose [106]. Also, scaffolds with a specific spatial gradient of proteins may built with directional cues to enhance nerve regeneration [107].

1.3 Research issues and objectives

The aim of this research is to develop 3D scaffolds for peripheral nerve tissue regeneration by focusing on the axon guidance, development and characterization of a novel 3D scaffold, and visualization of scaffolds by means of synchrotron-based diffraction enhanced imaging (DEI).

1.3.1 Axon guidance

In NTE, axon guidance is crucial to successful nerve regeneration [101, 108]. Axon growth and guidance may be mediated by many permissive factors, including scaffold biomaterials [71, 109, 110] and microstructure [111], growth-promoting and signaling molecules [112-114], as well as chemical gradients [115]. The challenge of axon guidance in scaffolds is that the scaffolds should deliver appropriate cues in a controlled and localized manner.

The first objective of the present study is to study the influence of scaffold materials on the axon guidance, specifically, to investigate the addition of laminin to chitosan scaffolds for promoting axon guidance in cultured adult dorsal root ganglion neurons. For this, scaffolds are created from chitosan with varying amounts of laminin added, and with controllable structure by means of a rapid prototyping technique - dispensing-based rapid prototyping (DBRP). The scaffold's influence on the growth and orientation of neurites is then studied *in vitro*.

1.3.2 Development and characterization of three-dimensional scaffolds

Scaffolds have been shown to be critical in tissue engineering. As mentioned in section 1.2.1, one of the challenges in NTE is to develop nerve conduit scaffolds with adjustable and controllable microstructure, mechanical properties, drug delivery, and degradation properties, in order to meet the requirements for a given PNI application. Scaffolds made from a single material hardly meet the comprehensive requirements for nerve tissue regeneration. Composite materials take advantage of the unique properties of each compound in the composite. RP techniques have shown promise for fabricating scaffolds with a controllable structure. A limitation of RP, however, is the high operating temperature of the system which can cause degradation of the materials and also limit the incorporation of biomolecules into the scaffolds [92, 116]. The combination of RP with freeze dry techniques (the rapid freeze prototyping technique - RFP) can avoid this drawback of RP and has potential to fabricate scaffolds with enhanced properties.

The second objective of the present study is to develop and characterize a novel 3D composite scaffold made from PLLA and chitosan microspheres (CMs). The scaffolds are fabricated by using the RFP, which combines RP with the freeze dry technique; and the CMs are fabricated by means of the emulsification method, particularly for the purpose of bioactive molecule delivery. The scaffolds are then characterized in terms of microstructure, mechanical properties, degradation behavior, and protein release behaviours.

1.3.3 Visualization of scaffolds by means of synchrotron-based diffraction enhanced imaging

In NTE, different visualization techniques are available to study tissues, tissue structures, and biomaterials/scaffolds. Scanning electron microscopy (SEM) is a surface measurement method which can be used to observe the surface features of scaffolds and cells [117]. Confocal laser scanning microscopy (CLSM) can visualize objects in 3D and requires fluorescent labeling [118], whereas the resolution in depth of the images is restricted to the micrometer scale. X-ray micro-computed tomography (μCT) is a nondestructive and noninvasive quantification method and can be used to perform 3D morphometric analysis of scaffolds and regenerative tissues. μCT techniques are becoming increasingly important to tissue engineering research in recent years [119]. However, there have been few applications of μCT in NTE. The main obstacle is the low x-ray attenuation contrast of low density polymer scaffolds and nerve tissues. Coupling synchrotron radiation based (SR) x-ray sources to μCT imaging techniques offers advantages such as better image quality, high photon flux, the possibility for monochromatization with a brilliance several orders of magnitude higher than those of a standard x-ray source, high spatial resolution (< 1 μm), a better signal-to-noise ratio, and the potential to lower the radiation dose by tissue samples [120]. One of the SR x-ray phase contrast imaging techniques, DEI, has shown its potential in the visualization of soft tissues [121]. However, its application to tissue engineering has not been reported in the literature.

The third objective of the present study is to explore the feasibility of visualizing

polymer scaffolds *in vivo* by using the DEI technique. For this, 3D PLLA/chitosan scaffolds embedded in rat muscle tissue are imaged by using DEI. The image contrast, radiation dose, and the limitation of sample thickness are also investigated.

1.4 Organization of the Dissertation

This dissertation is comprised of seven chapters. Besides this chapter, it includes five

manuscripts, followed by the conclusions drawn from this research.

Chapter 2 presents a literature review on visualization techniques in NTE applications. Specifically, the techniques of electron microscopy, CLSM, and μCT are examined, with the current and potential future applications of these techniques to understand properties of native tissues and tissue-engineered constructs in NTE.

Chapter 3 presents an investigation into the addition of laminin to chitosan scaffolds for promoting axon guidance in cultured adult dorsal root ganglion (DRG) neurons. Using the DBRP technique, 2D grid patterns were created by chitosan or laminin-blended chitosan substrate strands oriented in orthogonal directions; adult DRG neurons were selected and cultured on the patterns *in vitro*. The effect of the patterns on the orientation of neurite growth was investigated after 4 days of neuron culture.

Chapter 4 presents the development of a novel 3D scaffold made from a mixture of chitosan microspheres (CMs) and PLLA by means of the RFP technique. The microstructure, mechanical properties, and chemical characteristics of the

PLLA/chitosan scaffolds were evaluated. Also, the protein release rate of the scaffolds were studied.

In Chapter 5, the *in vitro* degradation of the PLLA/CMs scaffolds were investigated. The degradation properties of the scaffolds were characterized by using μCT, weight loss, Raman spectroscopy, and differential scanning calorimetry.

Chapter 6 presents a study on exploring the potential of x-ray diffraction enhanced imaging (DEI) as a novel method for the visualization of low-density polymer scaffolds in soft tissue. DEI can clearly visualize scaffolds embedded in unstained muscle tissue, as well as the microstructure of muscle tissue. The potential for the use of DEI in soft tissue engineering is discussed.

Chapter 7 presents the conclusions drawn from this research. This is followed by suggestions and recommendations for possible future work.

1.5 Contributions of the Primary Investigator

The papers included in this thesis are co-authored; however it is the mutual understanding of all authors that Ning Zhu, as the first author, is the primary investigator of the research work. The contributions of other authors are limited to an advisory and editorial capacity and they are acknowledged.

CHAPTER 2
REVIEW: VISUALIZATION TECHNIQUES FOR NERVE TISSUE ENGINEERING APPLICATIONS*

*This chapter has been published as "Zhu N., Chen X.B., Chapman D. (2010) A brief review of visualization techniques for nerve tissue engineering applications. *Journal of Biomimetics, Biomaterials, and Tissue Engineering*. 7: 81-99". According to the Copyright Agreement, "the authors retain the right to include the journal article, in full or in part, in a thesis or dissertation".

2.1 Introduction

Nerve tissue engineering applies the principles of biology and engineering to the development of functional substitutes for damaged nerve tissue [101, 122]. Scaffolds are developed through tissue engineering and employed as carriers for cells and biochemical factors as constructs providing appropriate mechanical conditions, or both. In general, the term scaffolds is used to describe all structures used to restore functionality of an organ either permanently or temporarily [123]. Ideally, a scaffold should (1) be highly porous with an interconnected three-dimensional (3D) pore network for cell growth and flow transport of nutrients and metabolic waste; (2) be biocompatible and bioabsorbable with a controllable degradation and absorption rate to match cell/tissue growth *in vitro* and/or *in vivo*; (3) have suitable surface chemistry for cell attachment, proliferation, and differentiation, and (4) match mechanical properties of the tissues at the site of implantation [124]. Biomedical imaging techniques are playing an increasingly important role in the rigorous characterization of engineered tissues and biomaterials. Imaging is a key means by which tissue engineers can determine which chemical and biological species are present in a

biomaterial, how those species are spatially distributed, and how long they remain functional. Recent advances have extended the application of sophisticated 2D and 3D imaging technologies to reveal complex biological events and species at biomaterial-tissue interfaces.

Imaging of engineered tissues is very important due to incomplete knowledge of cell physiology and dynamics, especially with regard to the integration of engineered and host tissues. Progress in tissue engineering requires a number of technological innovations in imaging, including (1) non-invasive, real-time methods to continuously monitor cell differentiation, scaffold degradation, and tissue replacement; (2) label-free techniques with comparable sensitivity techniques using labels at molecular and cellular levels; (3) ways to identify and track individual cells and cell subpopulations *in vivo*; (4) processes to image cells at deeper levels within tissues and organs; and (5) 3D image analysis and quantification [125].

In this article, the application of several visualization techniques in nerve tissue engineering is reviewed, including electron microscopy, confocal laser scanning microscopy (CLSM), and micro-computed tomography (μCT). The current and potential future application of these techniques to understand properties of native tissues and tissue-engineered constructs are also discussed.

2.2 Electron Microscopy

2.2.1 Scanning electron microscopy (SEM)

Scanning electron microscopy (SEM) has become a standard visualization method

for morphology elucidation, and is widely used in nerve tissue engineering for the characterization of engineered scaffolds. SEM images can reveal morphological features of scaffolds [126, 127] and allow direct measurement of the pore size [128], fiber diameter [129], and microsphere diameter [130]. Visual estimates of interconnectivity, cross-sectional area, and anisotropy can also be obtained [131, 132]. SEM imaging results can help to determine how scaffolds degrade [133], and this technique can also be used to observe morphological feature of cell attached to scaffolds, thus contributing to an understanding of cell-substrate interactions. SEM images are usually employed to study the attachment of nerve cells as well as surface spreading of different polymers [134]. For example, Bozkurt et al. observed the orientation of Schwann cells on the 3D-collagen scaffolds by means of SEM [135].

With the evolution of SEM techniques, applications for nerve tissue engineering are expanding. Environmental scanning electron microscope (ESEM) can be used with non-conductive samples; cells and materials samples do not require desiccation/dehydration and coating with gold [136]. ESEM could solve the problems with respect to the invasive preparation process of SEM, which may lead to incomplete results or unclear images. Recently, Martinez et al. reported that the combination of focused ion beam (FIB) lithography with scanning electron microscopy (SEM) in a double-beam apparatus makes *in situ* imaging of sample cross-sections possible in well-defined areas [137]. With the SEM/FIB technique, a given cell growing on the polymer substrates can be selected for analysis, and high resolution imaging of localized cross-sections of the cell can be achieved**.** Greve et al.

investigated substrate-induced effects on neuronal networks (Figure 2.1) [138]. The SEM/FIB allowed them to obtain the cross-section images of the selected neurites and neurons, demonstrating that the neuron attachment to the surface is discontinuous as regions of tight attachment alternate with cavities**.** This type of study would be extremely difficult using conventional SEM techniques. The SEM/FIB technique could be beneficial for revealing the interactions between nerve cells and the scaffold surface.

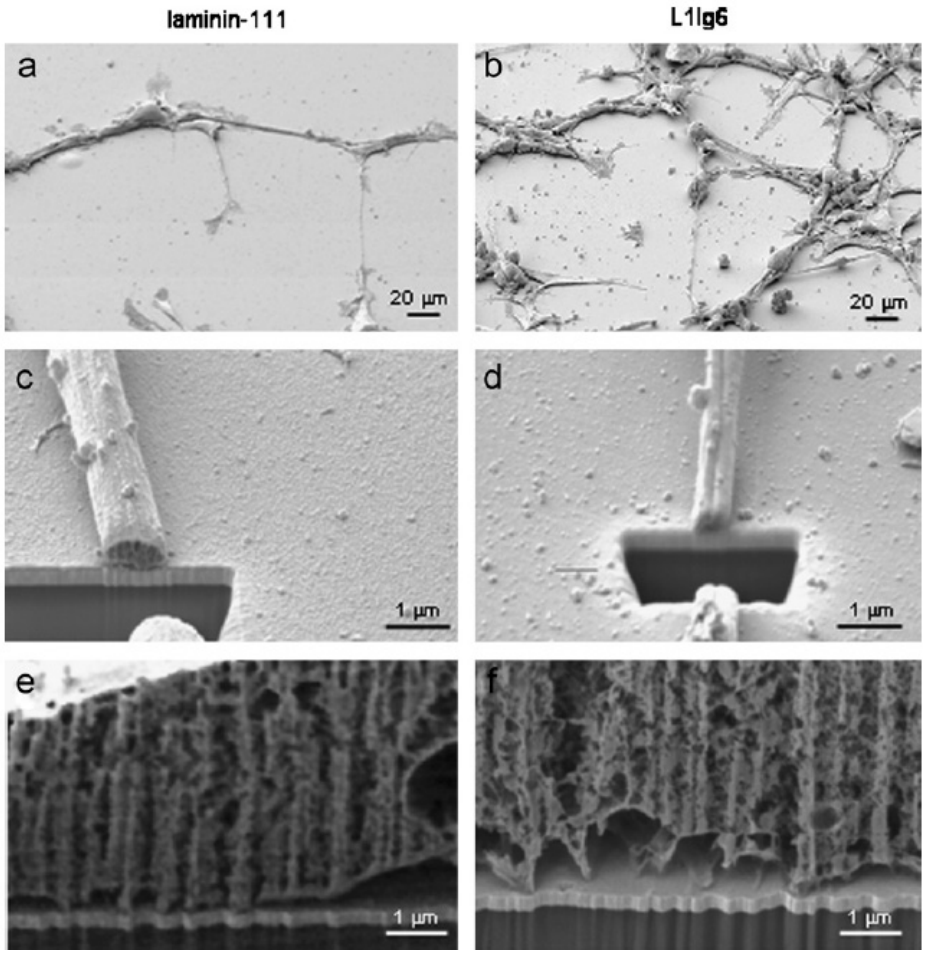

Figure 2.1. Images show chicken dorsal root ganglion neurons forming networks on laminin-111 (a, c, and e) and the sixth immunoglobulin domain of cell adhesion molecule L1 (L1Ig6) (b, d, and f) substrates analyzed by *in situ* focused-ion-beam milling followed by SEM (SEM/FIB). Figures (a) and (b) show an overview of the neuronal network; (c) and (d) show cross sections by *in situ* focused ion-beam milling through selected neurites extending on the substrates. Cross-sections through neuronal cell bodies on laminin-111 and L1Ig6 are shown in (e) and (f). (from [138])

2.2.2 Transmission electron microscopy (TEM)

Another electron microscopy technique widely used in biology and materials science is transmission electron microscopy (TEM). This method can obtain images with a spatial resolution of less than 1 nm, which enables the observation of regenerative nerve tissues at the cellular level. Specimens for TEM analysis must be thinner than about 100 nm for electron transmission to occur effectively. After staining, TEM is routinely used to visualize nerve tissues at the nanometer scale, including the detailed structure of myelin sheaths, Schwann cells, and axons [139, 140]. Combined with immunostaining methods, TEM images can distinguish some specific structures in nerve tissues [141]. In addition, TEM imaging can be used for reconstruction of small, highly detailed sample volumes by tilting ultrathin slices [142].

2.3 Confocal Laser Scanning Microscopy (CLSM)

Confocal laser scanning microscopy is a technique for obtaining high-resolution optical images with depth selectivity [143]. The key feature of confocal microscopy is its ability to acquire in-focus images from selected depths, a process known as optical sectioning or tomography. Images are acquired point-by-point and reconstructed with a computer, allowing three-dimensional reconstructions of topologically-complex objects. In effect, CLSM achieves a controlled and highly limited depth of focus. The penetration depth of CLSM can be from 10 to 300 μm.

2.3.1 Visualization of 3D samples

With advances in tissue engineering, more and more researchers are focusing on 3D culture *in vitro* experiments instead of 2D experiments, because 3D culture may be of more physiological relevance as *in vivo* due to the marked differences between cells cultured in 2D and 3D [144, 145]. When normal light or fluorescence microscopy becomes limited, confocal microscopy - a widely available tool - has gained popularity for 3D researches of engineered tissues, including cartilage [118], bone [146], and vascular [147]. In nerve tissue engineering, CLSM offers excellent possibilities to control the depth of field of scanning for monitoring fluorescent-stained neuronal structures at sub-micrometer resolution in 3D structure environments. Patz et al. reported B35 neuronal cells grew in a 3D substrate and formed a 3D neural network, which was captured by using CLSM at the depths up to 75 μm [148]. Smeal et al. used CLSM imaging results to determine that the substrate curvature influences the direction of nerve outgrowth [111]. Confocal images can also provide the evidence regarding the differences between morphologies of neuronal growth cones cultured in 2D and 3D environments [149].

2.3.2 3D image reconstruction

3D image reconstruction is another powerful function of CLSM techniques. With recent developments in fabrication, various 3D scaffolds with designed hyperfine microstructures are being applied to neuron culture and axon guidance, including those with groove/ridge type micropatterns [150] and 3D hydrogel patterns [151, 152].

The 3D images obtained by means of CLSM aid not only in the evaluation of 3D structural features of the designed scaffolds [152], but also contribute to understanding the effect of topographic features of the 3D scaffolds on neurite outgrowth (Figure 2.2) [150].

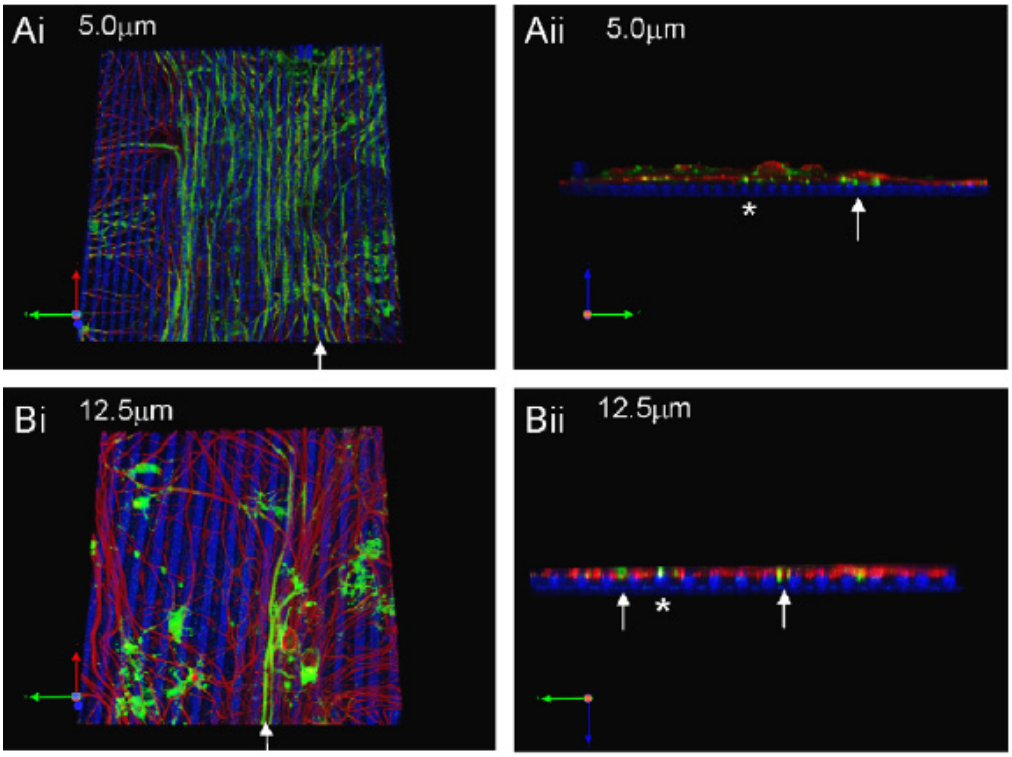

Figure 2.2. The CLSM images show the neurons growing on the groove/ridge type topography substrates that were 'buried' under a monolayer of astrocytes for up to 3 weeks. Cultures were immunolabeled with axonal (red) and myelin (green) markers after 3 weeks in culture. The microgrooves were visualized by reflection of the laser line (blue). Myelinated axons were found both within grooves (arrow) and on ridges (asterisk). (from [150])

2.3.3 Applications for *in vivo* studies

In vivo confocal microscope techniques are also employed in neuroscience and tissue engineering [153, 154]. In corneal tissue engineering, confocal microscopy has been utilized to assess cell and nerve ingrowth at the full-thickness of corneal tissue in live animals. Lagali et al. used *in vivo* confocal microscopy to evaluate corneal nerve

regeneration [155], where imaging results enabled the quantification of nerve parameters, including nerves number, density, and diameter.

2.3.4 Applications in drug delivery research

Coupled with fluorescence techniques, CLSM provides a comprehensive tool for the investigation of drug delivery [156]. After fluorescently-tagged bioactive molecules are encapsulated into micro- or nano-sized drug carriers, CLSM can be used to visualize the bioactive molecules in a 3D drug delivery system. CLSM can be applied to different drug carrier systems, such as film coatings, microspheres, and hydrogels [157]. For example, Piotrowicz et al. fabricated microspheres loaded with fluorescein isothiocyanate-labeled bovine serum albumin (FITC-BSA) instead of nerve growth factor and loaded them into the nerve guidance channels; their distribution within the wall structure was characterize using CLSM [35].

2.3.5 Applications to assess scaffold degradation

With the development of fluorescence techniques, characterizing degradation of tissue engineered materials using confocal imaging is now possible. Recently, Ballios et al. studied the *in vivo* degradation of the fluorescence-labeled hyaluronan/methylcellulose (HAMC) scaffolds by means of the 3D reconstructions of this injectable scaffold from the confocal images in the sub-retinal space (Figure 2.3) [158]. After the scaffolds were injected into the sub-retinal space of adult mice, they could be visualized by confocal microscopy both immediately and successively over

time to determine the degradation profile. During the degradation process, the fluorescence can be quantified by image analysis software. Furthermore, the degradation processes of some scaffold materials (such as poly(lactic-co-glycolic acid) (PLGA) [159]) lead to a change in pH. Thus, pH-sensitive fluorescent dyes can be coupled with these types of materials; as the materials degrade, they can be imaged using CLSM and the micro-environmental pH value can be measured. These image results can aid in the study of degradation properties of scaffold materials. Therefore, confocal microscope techniques show great potential as a non-destructive tool for the study of scaffold degradation.

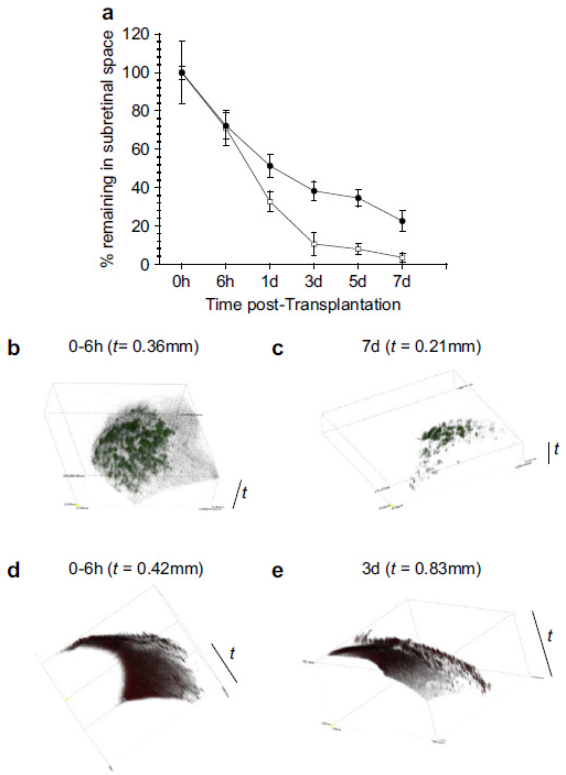

Figure 2.3. *In vivo* degradation characterization of the fluorescently labeled hyaluronan (HA)/methylcellulose (MC) blended material in the sub-retinal space. (a) Mass loss curves (% remaining) of HA (□) and MC (●) over 7 days as assessed by confocal microscopy of fluorescently-labeled components. The fluorescence intensity was quantified. Representative images are shown from HA (b, c) and MC (d, e) degradation time courses. Confocal reconstructions are over an area of 1.3×1.3 mm of tissue, with tissue thickness (t) as indicated. (from [158])

2.3.6 Prospective

CLSM imaging techniques have great promise for future applications in nerve tissue engineering. Development of new technologies may further increase the sensitivity, spatial resolution, and functionality of CLSM imaging in nerve regeneration processes. One advance in this area is the improvement of 3D reconstruction based on time-lapsed observation of live tissue. Du developed a fully-automated, non-rigid, intensity-based registration method to improve 3D reconstruction and subsequent visualization and quantitative analysis of fluorescently labeled live tissues using CLSM [160]. This improvement may be applied to the real time observation of dynamic changes in neuron outgrowth in 3D environments. Another advance comes from the development of fluorescence techniques. For example, obtaining voltage imaging of membrane potential in dendrites and axons of neurons by combining voltage-sensitive staining techniques with CLSM is now possible [161]. This non-invasive imaging technique may aid in the study of the electrophysiological behavior of neuron regenerative processes.

2.4. Micro-computed tomography (μCT)

2.4.1 Development of the μCT techniques

Computed tomography (CT) is a powerful non-destructive technique for producing 3D images that reveal the microstructure of objects [162]. In recent years, CT has become a widely applied tool in science and medicine [163-165], where it supports both clinical practice and fundamental research in areas including tissue engineering

[124, 166]. Conventional CT (such as medical) scanners are not suited for the study of objects at high resolution due to their large focal spot. Thus, micro-computed tomography (micro-CT or μCT) scanners have been developed predominantly for use in research applications. [167-169]. Desktop μCT systems provide nominal resolutions ranging from 5 to 100 μm, and specimens with diameters ranging from a few millimeters to 100 μm can be measured. However, the maximum power of the x-ray source is limited with a consequent upper limit to the available flux. Synchrotron facilities, especially third generation synchrotron facilities, can now generate x-ray photon fluxes several orders of magnitude higher, with high brilliance, small angular beam divergence, high level of polarization and coherence, low emittance, and the possibility for monochromatization [170, 171]. Synchrotron-based micro-computed tomography (SRμCT) can achieve quantitative images with high spatial resolution (1 to 10 μm) and signal-to-noise ratios [172]. This technique is well developed in medical and materials science for structural sizes down to several micrometers and is considered non-destructive and non-invasive with substantial potential for nerve tissue engineering applications.

2.4.2 Characterization of scaffolds

μCT techniques are becoming increasingly important for the visualization and analysis of tissue engineered scaffolds due to the advantages of non-destructive and non-invasive analysis and 3D image reconstruction. The architectural features of engineered scaffolds are studied after the design and fabrication process so that the

success and precision of the process can be assessed. The architectural characteristics of scaffolds include porosity, pore size, surface area to volume ratio, interconnectivity, anisotropy, strut thickness, cross-sectional area, and permeability [173, 174]. The pore structure of scaffolds is important for cell survivability and the pore network is used for molecular transport [175], including the exchange of oxygen, nutrient, metabolic wastes, and molecular signaling that are essential for cell migration and proliferation. When molecular transport is hampered due to poor diffusion, cell-scaffold constructs exhibit peripheral cellular growth while the interior of the construct undergoes necrosis [176]. These principles are also relevant for the design of nerve tissue engineered scaffolds applied in peripheral or central nerve regeneration.

Scaffolds with intricate interior structures can be visualized using μCT, as any spatial location of the architecture can be digitally isolated; this is a key advantage over conventional techniques, such as electron microscopy. Within the digital-excised scaffold cube, scaffold material volume and surface area can be measured, thus the porosity pore size, interconnectivity, anisotropy, strut thickness, and the surface area to volume ratio can be calculated. μCT imaging allows the user to select any specific location as a region of interest (ROI) where visualization of 3D pore shape and measurement of pore parameters can be conducted (Figure 2.4). To date, μCT techniques have been widely used to analyze the features of porous structure of the 3D scaffolds in tissue engineering. In nerve tissue engineering, for example, Silva et al. recently developed a 3D tubular structure scaffold for the applications to spinal cord injury regeneration and characterized the scaffolds using μCT technique [177].

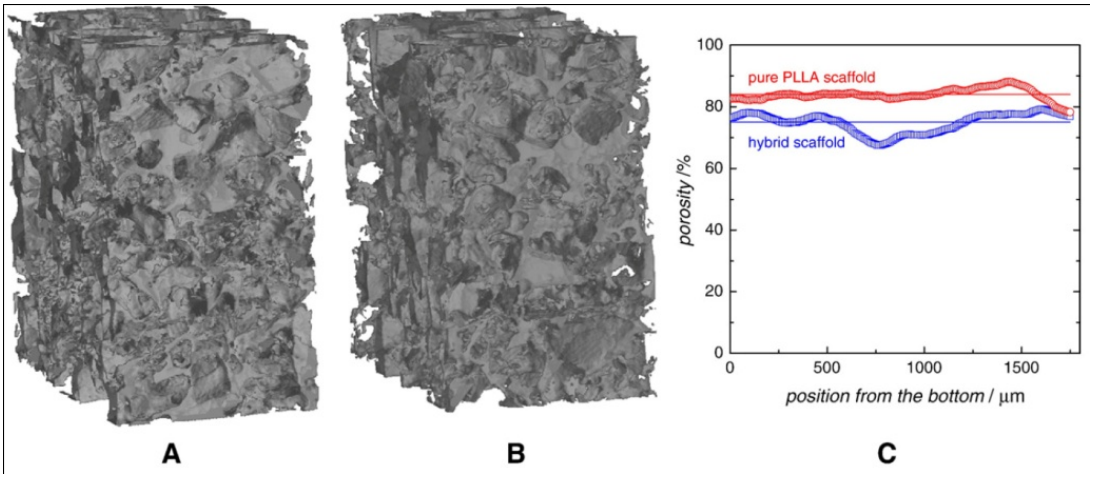

Figure 2.4. Micro-CT 3D images for a pure poly (L-lactic acid) (PLLA) scaffold (A) and a PLLA-chitosan hybrid scaffold (B). The variation of the porosity along the thickness of the scaffolds for the two analyzed structures is represented in the graph (C). (from [178])

2.4.3 Potential for µCT techniques in nerve tissue engineering

Conventional methods to study tissue-scaffold interactions use optical or transmission electron microscopy after histological sectioning, which involves many individual steps including fixation, embedding, sectioning, staining, and mounting [26, 179]. Each step can result in losses due to artifact production during preparation and/or in the process of rendering the complex 3D structures on 2D media [180]. For example, scaffolds may separate from their original position in the surrounding tissue. In the pilot *in vivo* experiment, a histological section image of a polycaprolactone (PCL) nerve conduit scaffold was obtained, which was used to bridge the sciatic nerve of an adult rat for 7 days (Figure 2.5). During frozen sectioning for histological staining, scaffolds embedded in nerve tissues can easily crack, transform, and move away from the surrounding tissues due to differences in hardness and plasticity between the synthetic materials and the tissue. Consequently, observing structural

changes in the degrading scaffolds as well as the reciprocal effects between scaffolds and tissues *in vivo* using histological methods are challenging. μCT is nondestructive and non-invasive, and therefore has significant advantages over histological methods, including the ability to study the samples over time or keep them intact for additional assessments. The quality of the data is also increased, because interventions can be assessed on an animal-specific basis; each animal acts as its own control and can demonstrate individual response characteristics, thereby eliminating the problems of cross-sectional studies. Moreover, the non-destructive aspects allow this method to be used to screen scaffolds before implantation, so only those that fulfill certain criteria are employed. Komlev et al. [164] used SRμCT to qualitatively and quantitatively evaluate tissue engineered bone growth kinetics in 3D porous scaffolds during implantation experiments. Hagenmuller et al. [181] quantitatively assessed the formation of bone-like tissue in the designed scaffolds using non-invasive time-lapsed μCT, and verified that μCT irradiation dose not impact the osteogenic performance of the stem cells based on a series of biochemical tests.

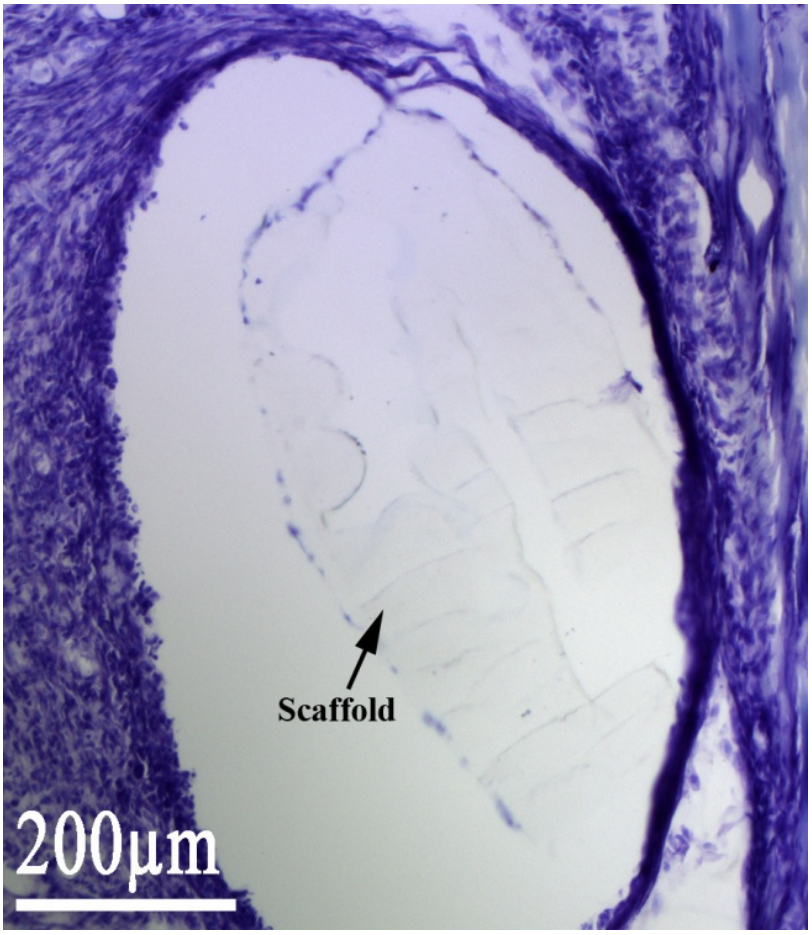

Figure 2.5. Histological section of a PCL scaffold implanted into an injured sciatic nerve of a rat for 7 days. The tissues are stained with purple color; the arrow shows the PCL scaffold.

Although, µCT techniques have been successfully and widely used for the studies of bone engineered scaffolds [182-184] and bone tissue regrowth [164, 181, 185] *in vitro* and *in vivo* in recent years, there have so far been few applications of µCT techniques to nerve tissue engineering. The primary obstacle is the low attenuation contrast of nerve tissue or scaffold samples. The principle of µCT techniques is largely based on the absorption contrast of imaged objects; objects with high absorption contrast can result in high quality µCT images. However, the density of nerve tissue and nerve engineered scaffold materials are both very low and similar, so

distinguishing them by using μCT techniques is difficult. With the combined availability of x-ray staining techniques and x-ray phase contrast techniques, there will be predict further advances in μCT techniques for nerve tissue engineering.

2.4.3.1 X-ray staining techniques

Neurons, nerve fibers, nerve tissue engineered scaffolds, and surrounding soft tissues have small differences in density. Thus, they exhibit almost no difference in x-ray absorption and are essentially invisible using conventional μCT, especially in a hydrated environment. Highly x-ray absorptive contrast agents with a high atomic number can be used to produce sufficient contrast in the acquired tomograms. These x-ray staining techniques are helpful for obtaining images to inform scaffold fabrication protocols and assess nerve tissue engineered scaffold architecture and the formation of new nerve tissues. Various dyes can be applied to stain soft tissues or some low density scaffold polymers for this purpose.

Osmium tetroxide (OsO_4) is a highly x-ray absorptive agent used for x-ray contrast enhancement in cells and soft tissues [186, 187], commonly used to prepare tissues for electron microscopy. It reacts with the unsaturated fatty acids and therefore increases the x-ray absorption of cell membranes. Nerve tissue can be stained with OsO_4 for visualization with x-rays. Lareida et al. used SRμCT technique to visualize the osmium-stained the nerve fiber network within the basilar membrane [188]. The high-quality 3D images exhibit the complex 3D morphology of the nerve fiber bundles, which are difficult to extract from histological slices (Figure 2.6). OsO_4 has

also been used to visualize scaffold architecture using x-rays [189]. However, the major disadvantage of O_sO_4 as a staining agent is its toxicity.

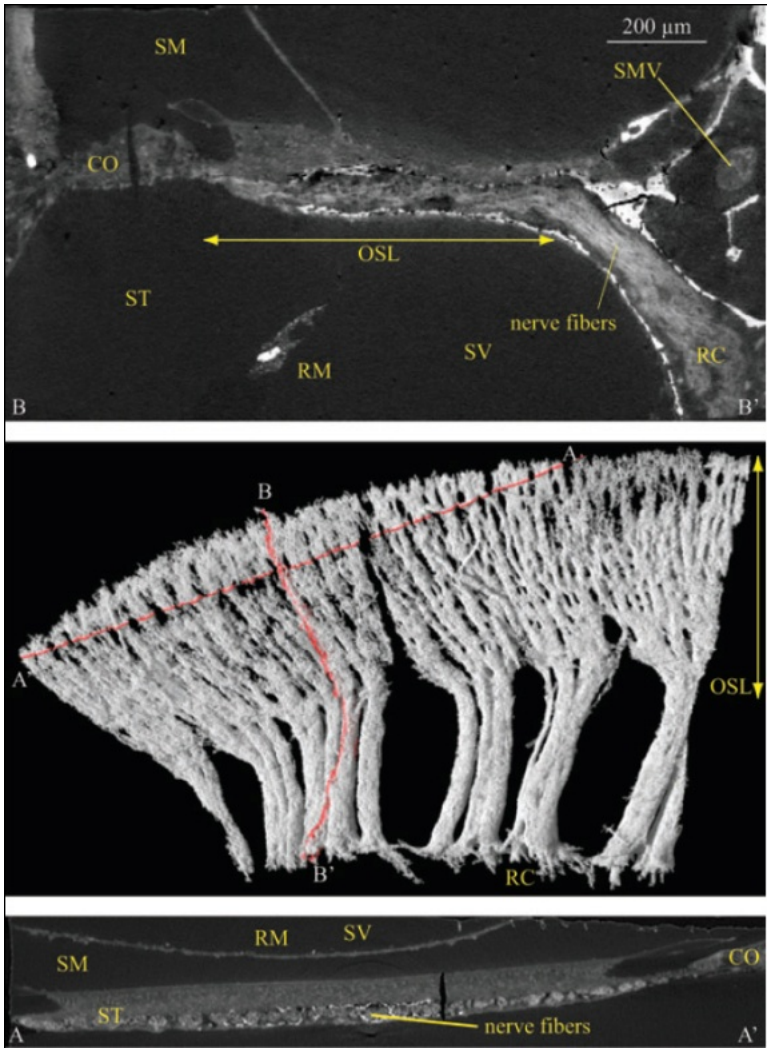

Figure 2.6. The reconstructed 3D SRµCT image using OsO_4 as a contrast agent exhibits the complex 3D morphology of the nerve fiber bundles in the human cochlea. The semi-automatic, intensity-based segmentation of the nerve fibers as given in the middle panel shows the spatial distribution of the fiber bundles. The orientation of the 2D slices is indicated in red in the 3D image and by A-A' and B-B' in the 2D slices. (from [188])

Lyophilic salts, such as $CaSO_4$, $SrSO_4$ and $BaSO_4$, enable the visualization of microvasculature in tissues [190, 191]. They are strongly hydrophobic and inert, and are injected into blood vessels using perfusion methods. Iodine, OsO_4, and lead

chromate can also be used to visualize blood vessel systems. The combination of contrast agents with μCT techniques can be used to not only show the complex 3D microvascular network architecture but also quantify vessel volume, thickness, number, connectivity, and degree of anisotropy [192]. The techniques show promise for the study of neo-vascularization in regenerative nerve tissues. Recently, Bolland et al. visualized the new blood vessel formation in poly (DL-lactic acid) scaffolds *in vivo* by means of lead chromate staining [193]. Briefly, the technique involves perfusion of a radio-opaque silicone rubber contrast agent containing lead chromate (Microfil MV-122, Flow Tech; Carver, MA) through the vasculature immediately following euthanasia. This technique has primarily been applied in small animal models.

Gold is another important contrast agent. Thurner et al. used gold-labeled lectin to stain foreskin fibroblasts and osteoblast-like cells for 3D morphology studies of cells on polymer scaffolds using SRμCT, because lectins can bind to sugar residues or derivatives on the cell membrane [194, 195]. From the acquired 3D data, the total cell volume, total cell volume density, and cell mass distribution can be quantified [196]. With respect to nerve tissue engineering, CLSM is of great value for cell imaging, but SRμCT seems to be the method of choice if quantitative 3D information is needed; this is especially true if opaque scaffolds are used. Furthermore, gold is a very useful contrast agent for biological systems research. Not only is it chemically inert and non-toxic, but it does not interfere with the normal cell function; the surfaces of gold nano-particles are also easily coated with a variety of proteins to provide some functional behavior in a biological environment [197]. Hall et al. reported that the

gold-loaded glioma cells permitted 3D visualization of the cells within bulk tissue using SRμCT technique [198]. Therefore, the features of gold make it useful in the investigation of the proliferation and migration of labeled cells implanted *in vivo*.

2.4.3.2 Synchrotron-based phase-contrast techniques

Synchrotron radiation, producing x-rays with higher photon flux and greater spatial coherence than standard computed tomography, has great potential for the development of new imaging methods. Synchrotron-based phase contrast techniques allow structural visualization of low density scaffolds and nerve tissues without fixation, sectioning, and staining.

(1) In-line phase contrast micro-tomography (PC-μCT)

In-line phase contrast technique is one of the x-ray phase contrast techniques. The image contrast principle of x-ray phase contrast techniques, briefly, is effectuated by local alterations of the x-ray refractive index n(x', y', z') causing phase changes of the x-ray wave upon passing through the sample [199]. The phase changes of the x-ray will be reflected on images as the edge enhancements for the different components of the samples. The amount of edge enhancement depends on the distance between the sample and detector, the x-ray energy, the resolution of the detector, and the phase properties of the sample. By combining in-line phase contrast techniques with micro-tomography, in-line phase contrast micro-tomography (PC-μCT; Figure 2.7) may be useful in nerve tissue engineering research.

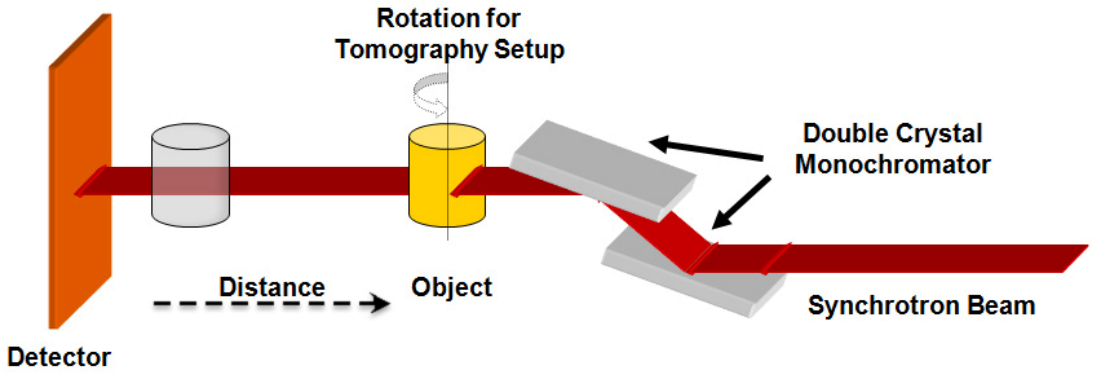

Figure 2.7. Schematic representation of the in-line phase contrast microtomography (PC-μCT). SR is the synchrotron radiation source. The distance between the object and detector is usually in a range from tens of centimeters to several meters. A large sample-detector distance can enhance the bending of beam (refraction) and thus results in sharper contrast near the edges.

Beckmann et al. acquired the 3D structural images of the unstained rat trigeminal nerves using PC-μCT, and a pattern of nerve fibers can be seen in the images [200]. Kim et al. used a third generation synchrotron radiation facility for the visualization of normal and damaged rat sciatic nerve without fixation and staining, and obtained the high resolution PC-μCT images [201]. The structures with small density differences, such as nerve fibers and surrounding tissues, were successfully imaged due to the attenuation of phase boundaries. Each nerve fiber could be easily discriminated and the arrangement of nerve fibers could be identified. However, the axons in each nerve fiber were still invisible due to the spatial resolution limitation of the PC-μCT images. Recently, Zehbe et al. reported inspiring results on the 3D morphological characterization of articular cartilage using PC-μCT [86]. The cell number/cell density (Figure 2.8) and the shape and orientation of the cells inside the cartilaginous part of the sample were quantitatively analyzed based on the 3D PC-μCT images.

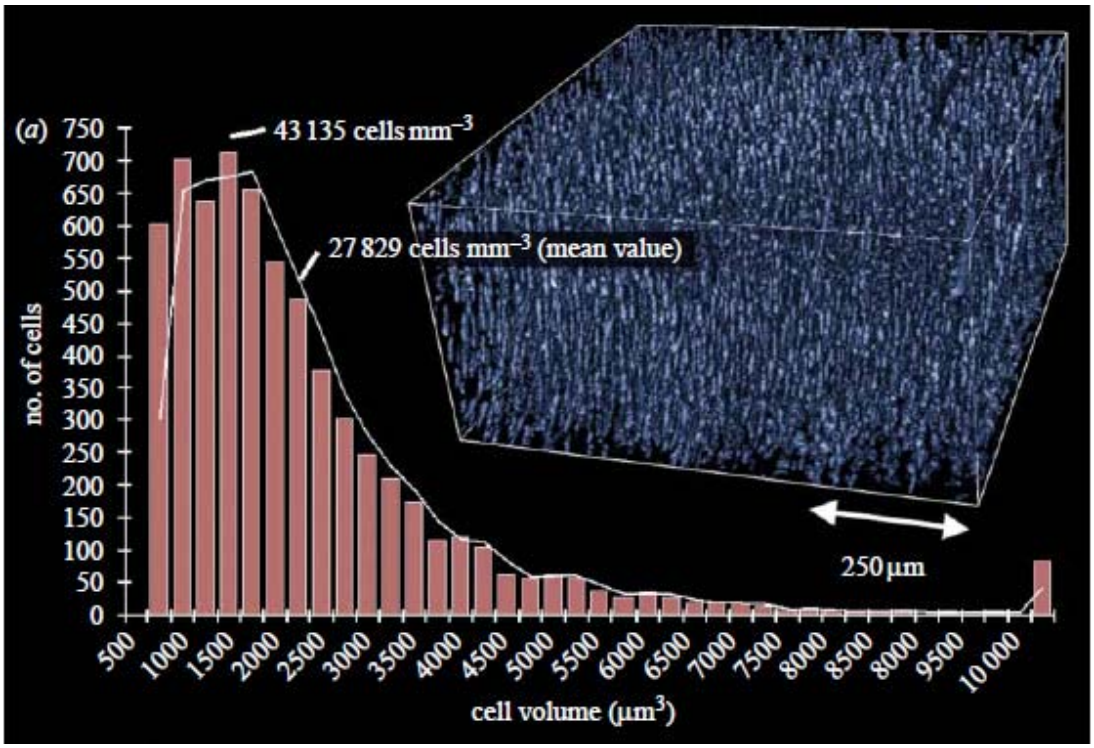

Figure 2.8. (a) Quantitative analysis from a 3D PC-μCT image for cell density in a 0.256 mm^3 volume of the soft tissue region of freeze dried articular cartilage. (from [202])

(2) Diffraction enhanced tomography (DEI-CT)

X-ray diffraction enhanced imaging (DEI; Figure 2.9) is another phase contrast technique based on differences in the x-ray refractive index distribution of an object; this method is more sensitive to relative differences between materials at certain x-ray energies than the absorption contrast method [203, 204]. Pure refraction contrast information of samples can be extracted by DEI analysis. The resulting refraction contrast image represents the spatial gradient of the refractive index, enhancing and highlighting edge appearance, contours, and interfaces of different tissues and materials.

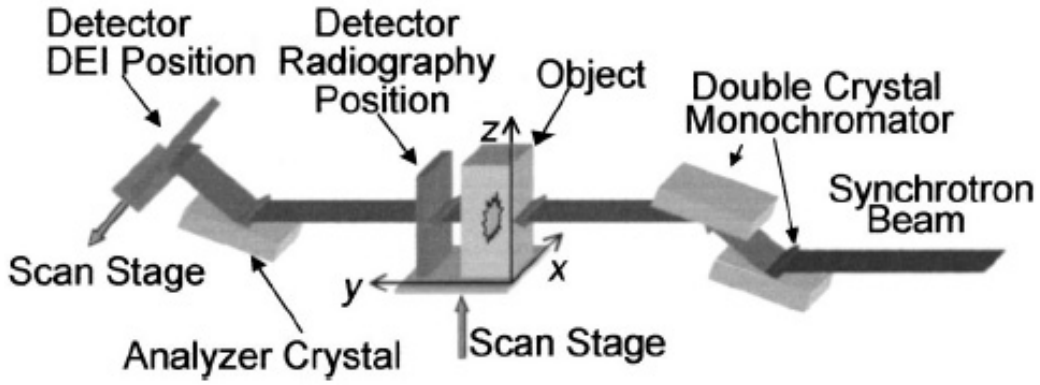

Figure 2.9. Schematic representation of the experimental setup for diffraction enhanced imaging and radiography (absorption imaging). The coordinate system is indicated near the object. The incident x-ray beam travels along the *y* direction, the object is scanned along the *z* direction, the image of the object is formed in the *x* - *z* plane, and the diffraction plane of the monochromator-analyzer crystal is the *y* - *z* plane. The detector is shown in two alternate positions: the upstream location is for radiography; the downstream location is for DEI. (from [205])

To date, DEI has been used to visualize liver [206, 207], breast [208], bone [209], and non-calcified tissues [210] including tendons, ligaments, adipose tissue, and cartilage. In the refraction images of normal liver tissue, vessel walls and vessel trees can be clearly distinguished down to small branches (tens of micrometers in diameter); this level of detail would not be achievable in a conventional absorption contrast image [206]. In a pilot experiment to visualize a low density biodegradable polymer, the DEI images of several low density polymers were produced, which have been used in nerve tissue engineering including poly (L-lactic acid) (PLLA) (block), polycaprolactone (PCL) (block), alginate (filaments), and chitosan (filaments) (Figure 2.10); the edges and shape of the scaffolds are clearly visible. The detailed structural information of the samples in the refraction angle images (Figure 2.10a-d) is greater than in the absorption images (Figure 2.10e-h). These results demonstrate the potential to visualize the microstructure of scaffolds using the DEI technique *in vitro*.

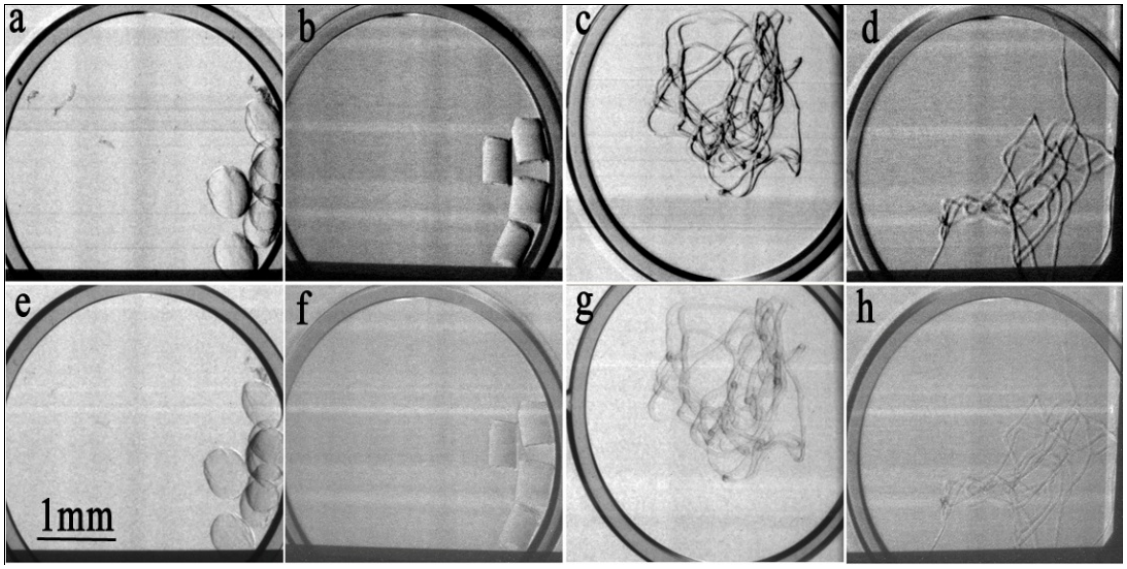

Figure 2.10. SR-DE images of PCL, PLLA, alginate filament, and chitosan scaffolds. (a,e) PCL, (b,f) PLLA, (c,g) alginate, (d,h) chitosan; (a-d) refraction angle images, (c-h) absorption images.

Combined with tomography techniques, x-ray diffraction enhanced tomography (DEI-CT) might be used to obtain 3D structural features of low density scaffolds and regenerative nerve tissues. The advantage of DEI-CT images is the capacity to provide detailed structural information. Bravin et al. visualized breast tissue using a SR-DEI-CT technique [211], where the DEI-CT images showed very rich detail corresponding to the structures of the histological section, even thin collagen strands (Figure 2.11). Another advantage of DEI-CT technique is that the radiation dose deposited in a given specimen by DEI-CT during scanning is less than that by desktop μCT techniques. The DEI extinction contrast of subjects can be large at high x-ray energies; higher energy means less absorption and a lower dose to the sample or subject [204, 212]. Therefore, compared with desktop μCT, the radiation dose may be reduced by an order of magnitude without compromising image quality. Reducing the dose in DEI-CT scanning is very important for *in vitro* and *in vivo* studies to prevent

structural and chemical changes that may occur due to x-ray exposure during the scanning process. Furthermore, repeat μCT scans of the same sample after removing some histological sections for comparison could be of interest. Under low dose scanning, DEI-CT can visualize scaffolds and regenerative tissues in living animals and may represent the next significant advance for *in vitro* and *in vivo* nerve tissue engineering studies.

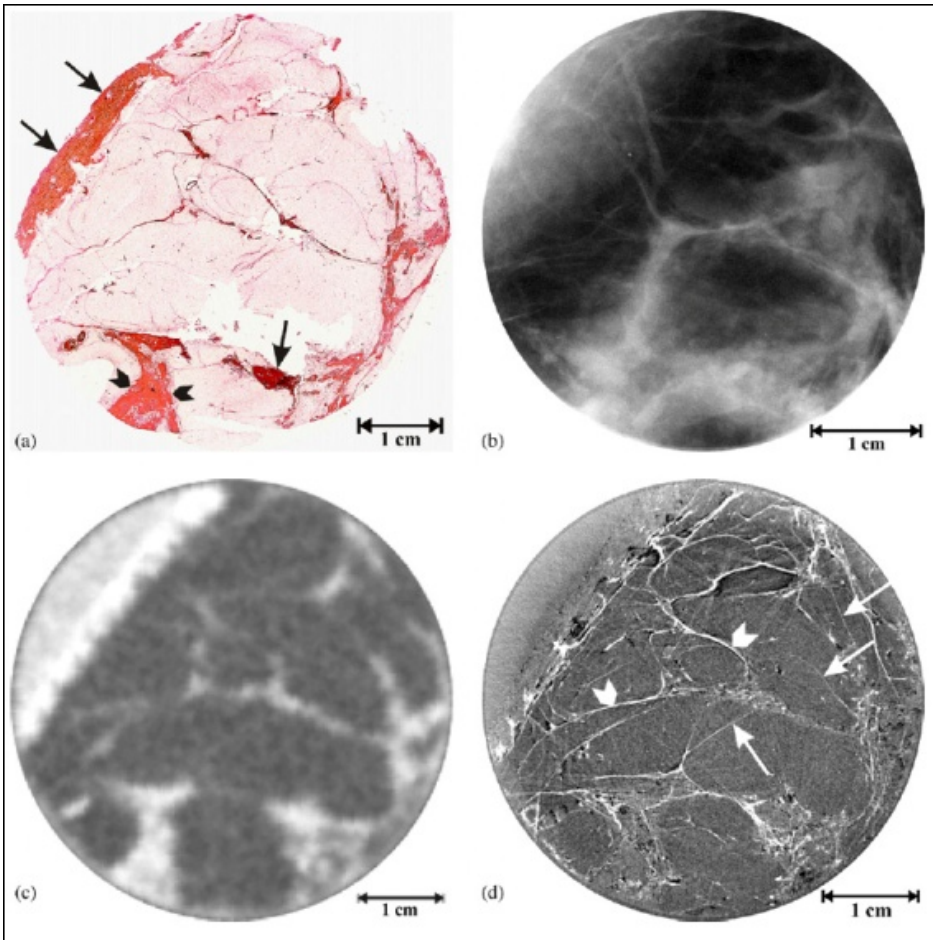

Figure 2.11. Comparison of the DEI-CT image and conventional images for the visualization of the breast tissue (a) Scanner image of the histologic whole-mount slide from a breast tissue sample with ductal carcinoma. The nuclei are shown in brown or black, young collagen and reticulin in bluish, mature collagen in red, adipocytes in white, and both red blood cells and muscle in yellow; (b) clinical screen film mammogram of the same sample; (c) clinical computed tomography (CT) image of the same sample; (d) DEI-CT top image of the same sample. (from [211])

2.5 Conclusions

Various visualization techniques play important roles in nerve tissue engineering studies. Some conventional visualization techniques, such as light microscopy, CLSM, and SEM, have been widely used to understand nerve tissue regeneration, analyze the morphological features of nerve tissue engineered scaffolds, and reveal the interaction of cells and biomaterials. To meet the demands of the evolving area of nerve tissue engineering, the conventional visualization techniques need to be improved by coupling other techniques, such as staining techniques and tomography methodologies. The improvements can provide images with higher resolution, allow imaging of 3D structure of samples, and improve the ability of quantitative analysis based upon imaging results.

μCT techniques have been employed in tissue engineering research, complementing conventional visualization techniques rather than competing with them. They provide an excellent non-destructive and non-invasive method for analyzing the structure of engineered scaffolds. This structural characterization detail is not afforded by other conventional porosity analysis techniques. μCT also offers the unique capacity to analyze tissue growth in porous scaffolds both *in vitro* and *in vivo*. With the development of x-ray staining and synchrotron light source techniques, low density scaffold materials and soft tissue can be visualized and qualitative and quantitative analysis by μCT. μCT techniques show great potentials in nerve tissue engineering studies, especially in real-time studies in living animals.

Selection of a suitable visualization technique to characterize scaffolds and tissues involves weighing the virtues and pitfalls associated with each technique. No visualization technique stands alone, but should be conducted in concert with others to better serve nerve tissue engineering research and help further our understanding regarding nerve regeneration.

CHAPTER 3
EFFECTS OF LAMININ BLENDED WITH CHITOSAN ON AXON GUIDANCE ON PATTERNED SUBSTRATES*

*This chapter has been published as "Zhu N., Li M.G., Guan Y.J., Schreyer D.J., Chen X.B. (2010) Effects of laminin blended with chitosan on axon guidance on patterned substrates. *Biofabrication*. 2(4): 045002". According to the Copyright Agreement, "the authors retain the right to include the journal article, in full or in part, in a thesis or dissertation".

3.1 Introduction

In nerve tissue engineering, axon guidance is crucial to successful functional nerve regeneration [101, 108]. Axon growth and guidance may be mediated by many permissive factors, including biocompatible scaffold biomaterials [71, 109, 110], growth-promoting and signaling molecules [112-114], the influence of chemical gradients [115], and fabrication of a rationally designed microstructure [111]. However, conventional techniques for manufacturing scaffolds, including solvent casting and particulate leaching [79], gas foaming [213], fiber meshes and fiber bonding [214], and phase separation [215] offer little capacity to precisely control the internal structure and biochemical features of scaffolds. To achieve more precise microstructural features, various rapid prototyping (RP) techniques have been used in recent years for tissue engineering scaffold fabrication [216-218]. Among them, dispensing-based rapid prototyping (DBRP) is a promising method by which biomaterials in a fluid form are delivered to build scaffolds in a controllable manner [216]. Specifically, biomaterials are continuously extruded from a needle and deposited on substrates, forming 2-dimensional (2D) or 3-dimensional (3D) strand

micropatterns of scaffolds [216, 219]. DBRP offers an efficient approach to create such micropatterns with complex 2D or 3D architectures and chemical subdomains, which, notably, may not be producible by means of conventional lithographic methods.

Chitosan is a natural biological polymer that has been widely studied for tissue engineering scaffolds applications, including reconstruction of bone [220], vasculature [221], liver [222], and other tissues, because of its mechanical properties, biocompatibility, and biodegradability [223-225]. The cationic nature of chitosan also contributes to the retention and concentration of growth factors secreted by colonizing cells [226]. Chitosan also has good cytocompatibility for neural growth [227], making it a good candidate for promoting the repair of peripheral nerves. However, chitosan does not have any specific bioactivity to interact with neurons for the purpose of axon guidance in nerve regeneration. This problem can be solved by material modification methods. One effective method for synthesizing new composite materials for particular tissue engineering applications is polymer blending [30, 228], which is very suitable for use with the DBRP technique. By blending with other materials, chitosan can be imbued with desired functional properties [109].

Laminin is an extracellular matrix (ECM) adhesion protein, which appears to be an important guidance signal molecule for developing axons *in vivo* [229]. It also demonstrates a neurite-promoting activity in tissue culture, and can stimulate the mitosis of the Schwann cells that form myelin around mature axons in the peripheral nervous system (PNS) [230].

In this study, chitosan was blended with laminin to support and guide neurite growth in a tissue culture model. Adult dorsal root ganglion (DRG) neurons were selected for cell culture and analysis. The axons of DRG neurons are a major component of PNS nerves. Moreover, DRG neurons can be cultured from adult (rather than embryonic) animals, and therefore serve as a better model for regenerative (rather than developmental) axon growth and guidance.

The uniform 2D surfaces were first examined, then more complex 2D micropatterns. The aim was to determine the effect of the microenvironment of axon-materials affinity difference on axon guidance. If the method is validated and applied to the design of 3D nerve conduit scaffolds, materials demonstrating axon affinity may effectively guide the directional growth of axons and help to realize the functional recovery of peripheral nerve injury.

3.2 Materials and Methods

Chitosan (28191), laminin (L2020), and poly-l-lysine (P9155) were purchased from Sigma-Aldrich Canada and used as received to prepare stock solutions, chitosan powder was dissolved at 3% (w/v) concentration in 2% acetic acid by stirring overnight, then sterilized by exposure to 6.5 KGy gamma irradiation. Laminin (1 mg/ml in 50 mM Tris pH 7.4 and 0.9% NaCl) was thawed and aliquoted under sterile conditions. Lyophilized poly-l-lysine powder was dissolved at 25 μg/ml in deionized water under sterile conditions.

3.2.1 Fabrication of micropatterns for testing

(1) 2D uniform surfaces

Blended laminin-chitosan solutions at w/w ratios of 0%, 0.03% and 0.06% (denoted by ChLN0, ChLN3, and ChLN6, respectively) were prepared by uniformly mixing laminin into stock chitosan solution using a vortex mixer at 2000 rpm for 10 minutes. To prepare uniform 2D surfaces, glass coverslips were dipped in the ChLN0, ChLN3 or ChLN6 solutions to form a thin film, and then dried under flowing sterile air at room temperature. For control comparison, poly-l-lysine (PL) coated coverslips were also prepared by puddling poly-l-lysine solution onto the entire surface area of the glass coverslips and incubating at 37°C in a 5% CO_2 incubator for 4 hours. These coverslips were then washed three times with phosphate buffered saline (PBS) and dried under sterile air at room temperature. In additional preparations, poly-l-lysine coated coverslips and chitosan dipped coverslips were then secondarily coated with laminin (denoted by PL+LN and Ch+LN, respectively). Laminin solution was puddled onto the entire surface area of the coverslips at 4°C overnight; the coverslips were then washed 3 times with PBS and dried under sterile air at room temperature.

(2) 2D micropattern surfaces

A precision fluid dispensing system (C0720M, Asymtek) [216] was used to fabricate 2D grid patterns on glass coverslips using the different blended laminin-chitosan solutions: ChLN0, ChLN3, and ChLN6. A schematic illustration of the DBRP system is shown in Figure 3.1. The movements of the dispensers in three

dimensions (X, Y, and Z) and the extrusion speeds were controlled by programming. During the fabrication process, the ChLN0 was extruded from one dispenser, and either ChLN3 or ChLN6 was extruded from the other. The software first controls the dispenser loaded with ChLN0 solution, extruding the solution onto a glass coverslip to form parallel strands. The software system then controls the other dispenser containing ChLN3 or ChLN6 solution, extruding the solution onto the same coverslip to form parallel overlaying strands in the orthogonal direction. When this procedure was finished, the patterns on the glass coverslips were dried under sterile air at room temperature.

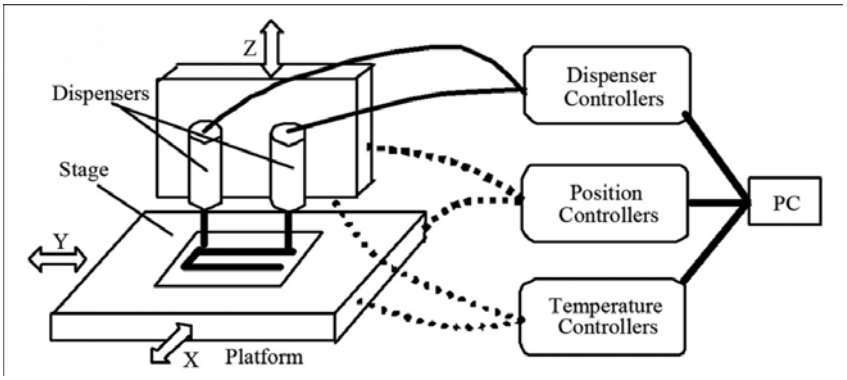

Figure 3.1. Schematic diagram of the DBRP system.

3.2.2 DRG Neuron Culture

Primary dorsal root ganglion (DRG) neurons harvested from Sprague-Dawley rats (approx. 250 g) were dissociated using collagenase and trypsin [231, 232] and seeded on the uniformly coated or the micropatterned coverslips at a density of 1600 neurons/cm^2 and cultured in Dulbecco's Modified Eagle Medium (DMEM) +10% horse serum + antibiotic/antimycotic solution at 37°C in a 5% CO_2 incubator for 4 days, then subjected to immunocytochemical and microscopic analysis.

3.2.3 Immunocytochemistry of neurons

Coverslips were gently rinsed with PBS. The cells were fixed in cold methanol (-20°C) for 30 minutes and then rinsed with PBS. The fixed cells were blocked against non-specific binding (PBS + 0.5% bovine serum albumin + 1% horse serum) for 1 hour at room temperature. DRG neurons and neurites were stained using primary antibody against growth associated protein-43 (GAP-43) [233] diluted 1:5000 in blocking solution. After rinsing with PBS + 0.05% Tween 20, Cy3-conjugated anti-mouse IgG (Jackson Immuno Research) diluted 1:300 in blocking solution was applied as a secondary antibody for 60 min at room temperature. The DNA binding dye 4',6-diamidino-2-phenylindole (DAPI) was used to stain the cell nuclei.

3.2.4 Characterization of patterns

A Zeiss Axioskop microscope was used to examine the 2D grid patterns created on the coverslips. Chitosan strands and the cultured cells were observed using phase-contrast microscopy. Immunofluorescence for laminin was then used to visualize the ChLN3 and ChLN6 strands. Briefly, the coverslips were blocked against non-specific binding (PBS + 0.5% bovine serum albumin + 1% horse serum) for 1 hour at room temperature. Laminin was stained using an anti-laminin antibody (Sigma-Aldrich L9393) diluted 1:200 in blocking solution. After washing with PBS + 0.05% Tween 20, Cy2-conjugated anti-rabbit IgG (Jackson Immuno Research) diluted 1:300 was applied as a secondary antibody for 60 min at room temperature, followed by washing with PBS + 0.05% Tween 20.

To study the variation of the surface height at the overlapping boundary of two orthogonal strands, images of the topography of the grid patterns at an intersection were captured by means of an atomic force microscope (AFM) (Agilient 4500, Agilent Technologies) operating in intermittent contact mode. A silicon cantilever (Applied NanoScience) with a force constant of 48 N/m and resonant frequency of approximately 190 kHz was used. All measurements were performed at ambient conditions with the instrument mounted on an Olympus microscope located on a floating air table.

The infrared spectra of ChLN0 and ChLN6 films were measured with an FTIR (FT-IR 4100, JASCO) spectrophotometer. Each spectrum was acquired in ATR (attenuated total reflection) by accumulation of 32 scans with a resolution of 4 cm^{-1} in the spectral range of 4000 - 400 cm^{-1}.

3.2.5 Image analysis

To evaluate neuron viability and the length of growing neurites on the uniformly coated coverslips, images of the neurons were captured with a fluorescent microscope (Zeiss Axioskop). For each type of substrate, three coverslips were examined and the images were taken from 25 different locations on the coverslips. Captured electronic images were analyzed using Northern Eclipse 7.0 software (Empix Imaging). All neurons were counted based on GAP-43 staining. The lengths of GAP-43 positive neurites were measured using Northern Eclipse. Length analyses were conducted by: (1) highlighting neurites using a binary threshold, which transforms the gray level

image into a binary image. The binary threshold value was set based on the neurite size in a typical gray level image and the all the gray images were, then, transformed applied in the same binary threshold value; (2) 'skeletonizing' neurite profiles by reducing them to one pixel width; and (3) determining the neurite length in terms of the sum of the skeletonized neurite pixels. To evaluate the direction of neurite outgrowth on the 2D micropatterned substrates, a vector was manually measured from the cell body of a neuron to the tip of its neurite by means of ImageJ 1.34 software. The neuron cell bodies were identified based on their round shape, a cell body diameter of 20 μm or greater, and low density DAPI staining of their nuclei.

The angle of each vector was expressed as deviation from 0°, the direction of the ChLN3 or ChLN6 strands, on fluorescent images.

3.2.6 Statistical analysis

An unpaired t-test was used to evaluate the results using Origin Pro 7.5 (OriginLab) software. Repeated-measure statistical analysis was employed to analyze the data for each of the character parameters. In all evaluations, $p < 0.05$ was considered to be statistically significant.

3.3 Results

3.3.1 ATR-FTIR spectroscopy

Figure 3.2 shows the FTIR spectra of the chitosan containing laminin (a), the unmodified chitosan (b), and the pure laminin (c). The (a) and (b) FTIR spectra had

very similar characteristics. The absorption peaks of chitosan at about 1640 and 1553 cm^{-1} were assigned to carbonyl stretching vibration of amides (amide I band) and N-H bending vibrations of amides (amide II band), respectively. Whereas, for the chitosan containing laminin, a prominent band at 1585 cm^{-1} was observed, which suggested that there were more hydrogen bonds formed in chitosan because of blending laminin. The amide I bond at 1621 cm^{-1} in the laminin FTIR spectrum (c) was not evident in the spectrum (a) of the chitosan containing laminin, possibly reflecting loss of the β sheet structure in the laminin. These findings suggest that the secondary structure of the laminin has been changed after being mixed into chitosan.

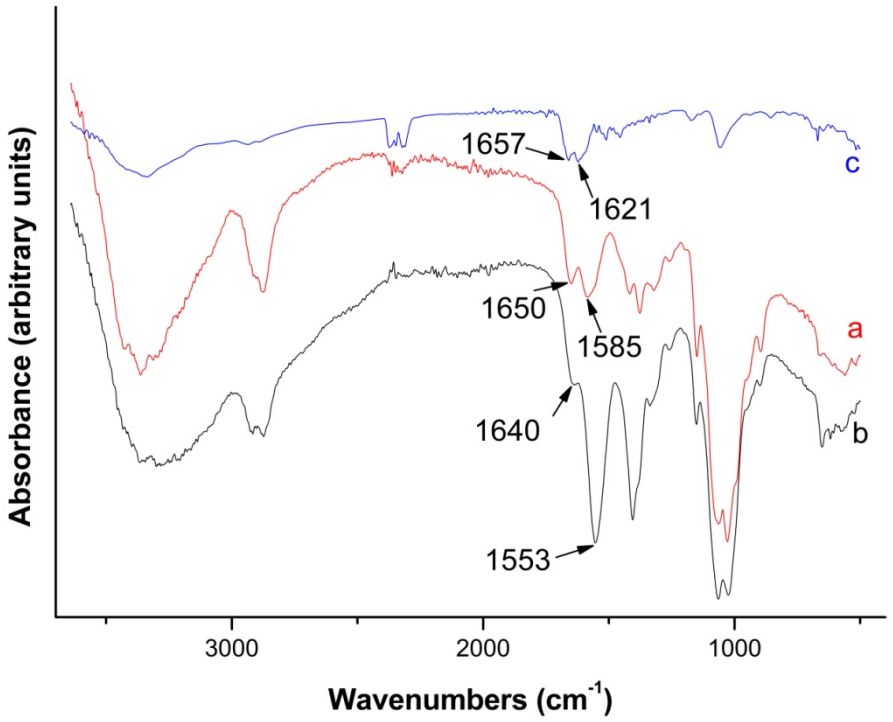

Figure 3.2. ATR-FTIR spectrum of (*a*) chitosan containing laminin, (*b*) unmodified chitosan and (*c*) pure laminin.

3.3.2 Cell viability and length of neurites on uniform surfaces

After 4 days in culture, DRG neurons had grown better on a uniform surface of

ChLN6 than on ChLN3 or ChLN0 coated coverslips. Figure 3.3(a-e) shows typical images of DRG neurons undergoing neurite growth. The average number of surviving neurons in an area of 0.7 mm x 0.5 mm on the ChLN0 coated coverslips (4.00±1.53) was significantly less than on Ch+LN (8.57±2.97), ChLN3 (6.28±2.51), or ChLN6 (6.00±2.51) coated coverslips (Figure 3.3f). The differences in neuron number among PL+LN, Ch+LN, ChLN3, and ChLN6, however, were not significant ($p > 0.05$). Neurites growing on ChLN6 were significantly longer than that those on the ChLN3 or ChLN0 ($p < 0.01$) (Figure 3.3g). There was no significant difference ($p > 0.05$) between the length of neurites grown on ChLN3 and ChLN0. The neurons grown on Ch+LN coverslips had longer neurites than those grown on ChLN6 ($p < 0.01$). These results indicate laminin improves the viability of neurons grown on chitosan, and the length of neurite growth is sensitive to the concentration of laminin blended into the chitosan.

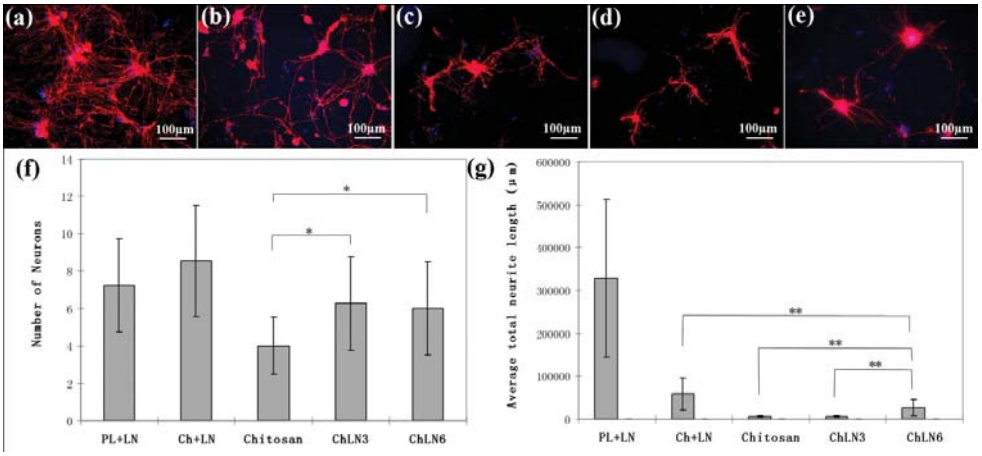

Figure 3.3. Cell viability and length of neurites of DRG neurons after culturing for 4 days on uniform surfaces. (a)-(e) Immunofluorescent images for (a) PL+LN coating, (b) Ch+LN coating, (c) ChLN0 coating, (d) ChLN3 coating, (e) ChLN6 coating. Neurons and neurites (red) were stained with anti-GAP-43 and the nuclei of neurons and associated glial cells (blue) were stained with DAPI; (f) Mean number of neurons in an area of 0.7 mm x 0.5 mm; (g) Mean total neurite length/mm^2. (*: $p < 0.05$, **: $p < 0.01$).

3.3.3 2D micropattern analysis

The grid patterns created using the DBRP system are shown in Figure 3.4. The width of the strands is approximately 100 μm; the parallel strands are separated by spaces of approximately 200 μm. The strands containing laminin (ChLN6 or ChLN3) were dispensed on the top of the ChLN0 strands at an angle of 90°. All strands can be observed under phase contrast microscopy (Figure 3.4a). With immunofluorescent staining for laminin, the image of the ChLN3 or ChLN6 strands is clearly seen. The fluorescent image also shows that laminin was uniformly distributed within the laminin-chitosan strands (Figure 3.4b).

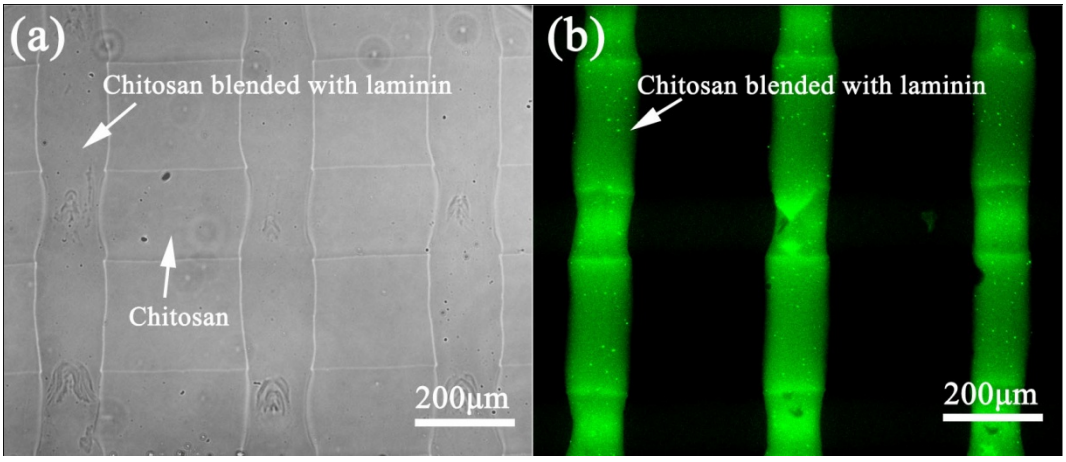

Figure 3.4. (a) Phase contrast image of the grid pattern on a glass coverslip, in which horizontal strands were made of chitosan and vertical strands are made of chitosan blended with laminin. (b) Immunofluorescent localization of laminin (green) within the same field.

AFM was used to observe the surface features at the overlapping parts between ChLN0 and ChLN6 strands (Figure 3.5). The variation of the surface height in the observed area (30 μm x 30 μm) is from 0 to 20 nm. Although previous studies reported that topographic features at the nano- and micrometer scale can affect the orientation of neurite growth [234, 235], the variation of the surface height at the

overlapping boundary of two orthogonal strands in this pattern model is slight and gentle and is unlikely to influence the orientation of neurite growth.

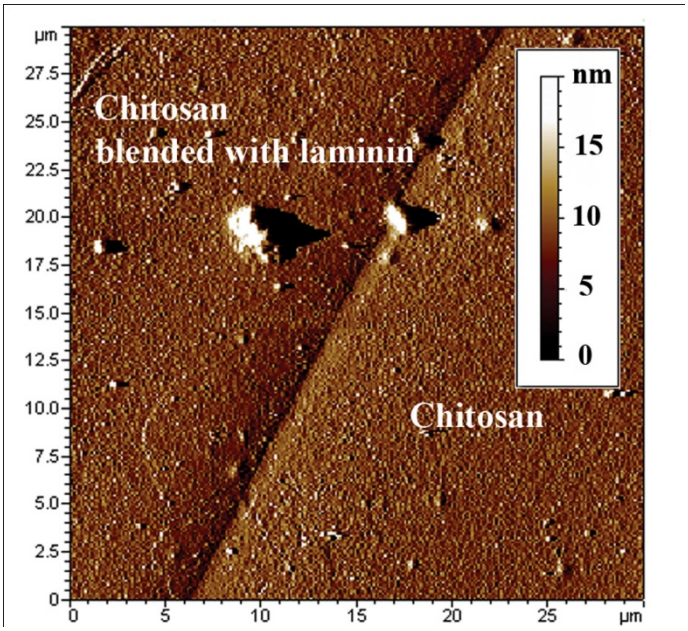

Figure 3.5. Atomic force microscopy (AFM) topographic images of the ChLN0/ChLN6 grid micropatterns at the area of overlap. Scanning area: 30 µm x 30µm. The color scale demonstrates that the topographic variance of the strand base material does not exceed 20 nm.

3.3.4 Directional growth of neurites

Qualitative observations of 2D micropatterned cultures suggest that the orientation of DRG neurites often align with the laminin containing strands when grown on ChLN0/ChLM6 micropatterns (Figure 3.6a,b). To investigate this quantitatively, the angles of the vectors corresponding to overall direction of neurite growth were systematically measured and compared these vectors to the orientation of the laminin-free and laminin-blended strands (Figure 3.6c). These data confirm the qualitative impressions as a marked preference for the neurite growth vectors corresponding with the orientation of the laminin containing strand could be documented.

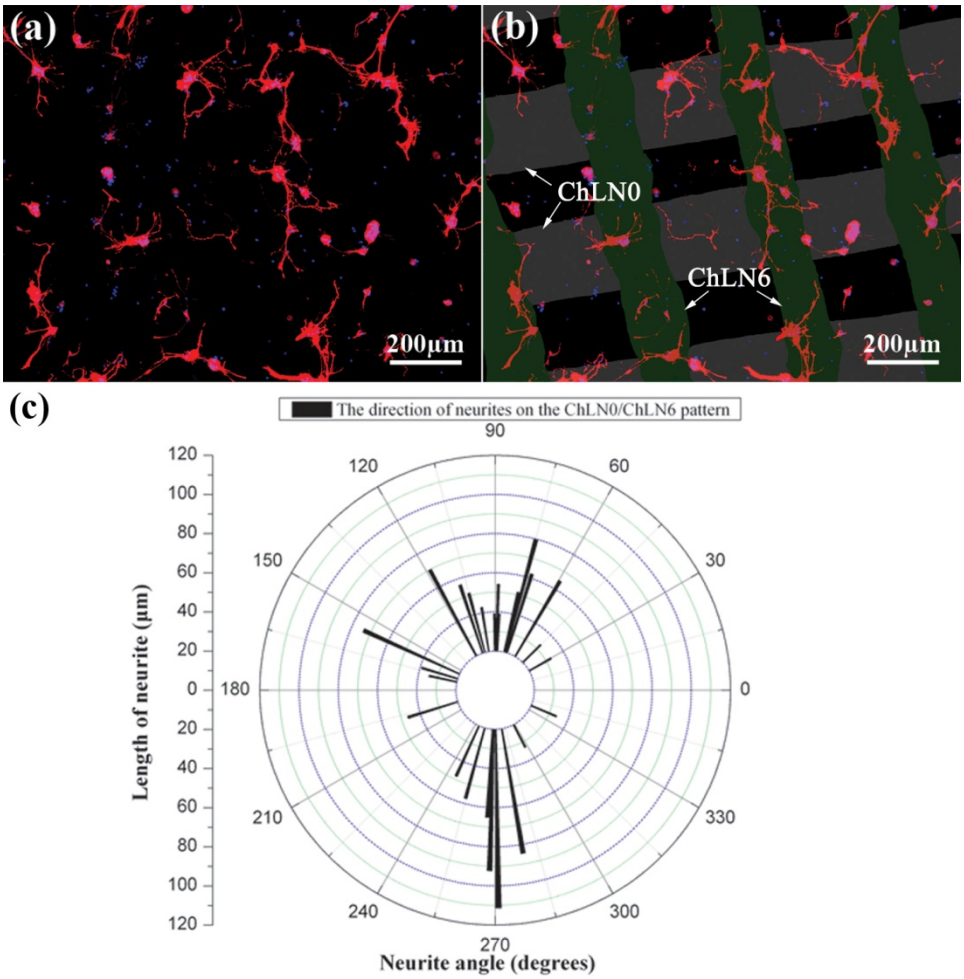

Figure 3.6. Immunofluorescent images showing relationship of neurites to laminin-containing strands. (a) DRG neurons and neurites visualized with GAP-43 immunocytochemistry (red) after culturing for 4 days on a ChLN0/ChLN6 2D micropattern. Neuronal and glial nuclei are stained with DAPI (blue). (b) The same image is superimposed on a false color image of ChLN0 strands (grey) and ChLN6 strands (green) positioned on a glass substrate (black). (c) Circular histogram showing the distribution of neurite angles on the ChLN0/ChLN6 pattern in this image. Only the angle of the longest neurite of each neuron is counted.

A wider sample of cultures was then surveyed, including DRG neurons grown on ChLN0/ChLN3 and ChLN0/ChLN6 micropatterns. In each case, the angle of the vector corresponding to neurite direction on the micropatterned substrates was measured as a deviation from the direction of the ChLN0 strand by 0° to 180° and the pooled results were sorted into bins. Figure 3.7a shows the distribution of neurite

angles on the ChLN0/ChLN3 micropatterns is random within the range from 0° to 180°. Thus, the lower concentration of laminin does not appear to impose a directional preference on neurite growth. In contrast, Figure 3.7b demonstrates the majority of the neurite angle measurements made from cultures on the ChLN0/ChLN6 micropatterns fell within a 20° interval around the 90° direction, which is the direction of ChLN6 strands. This suggests that the strands fabricated with the ChLN6 preparation possess a biologically relevant neurite-orienting property. Observations of the morphology of individual neurons (Figure 3.8) suggest that the neurites growing along ChLN6 strands are longer than those along the ChLN0 strands. Indeed, two neurites from the same neuron could show a preference for longer extension on the ChLN6 surface (Figure 3.8a; Arrows 1, 2). Neurites also displayed a tendency to remain on the ChLN6 strand when confronted with a choice (Figure 3.8b; Arrow 3). Compared to the ChLN0/ChLN6 pattern, the neurites in the ChLN0/ChLN3 pattern showed a reduced tendency for strand-specific increased elongation or preference to grow in a certain direction (Figure 3.8c).

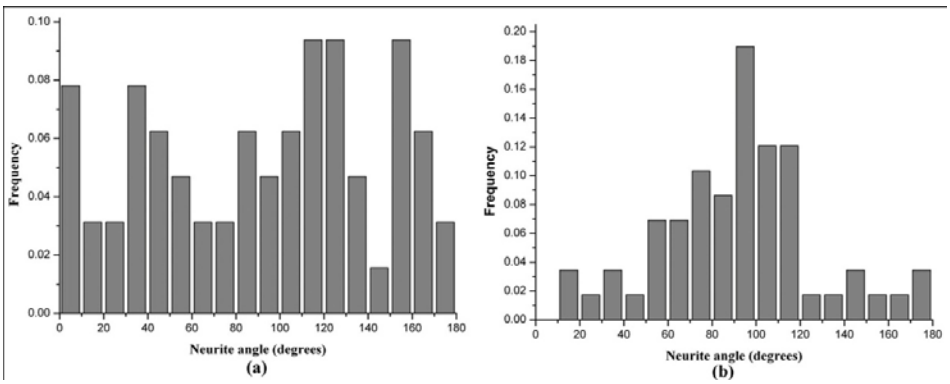

Figure 3.7. The angle distributions of the longest neurite from each DRG neuron on replicate 2D micropattern substrates. (a) Distribution of neurite angles on the ChLN0/ChLN3 micropatterns (64 neurites from 22 different fields). (b) Distribution of neurite angles on the ChLN0/ChLN6 micropatterns (58 neurites from 22 different fields).

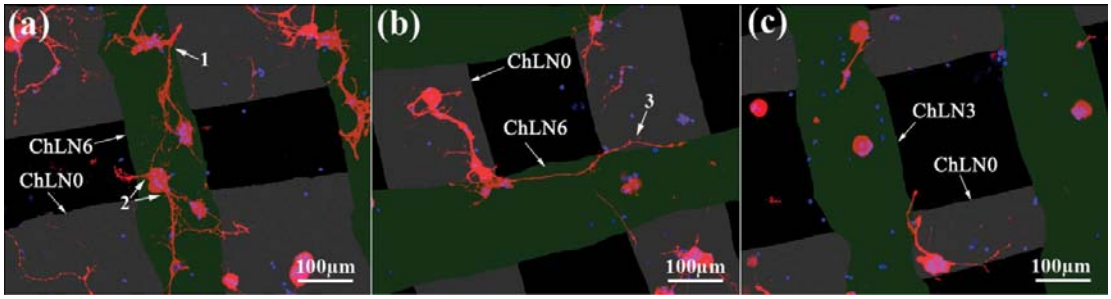

Figure 3.8. Details of immunofluorescent images of DRG neurons after culturing 4 days on the micropatterned substrates. (a) and (b) Neurons cultured on a ChLN0/ChLN6 micropattern; (c) Neurons cultured on a ChLN0/ChLN3 micropattern. Arrow 1 shows a neuron with a short neurite extending onto unmodified chitosan, and longer neurites extending onto chitosan blended with laminin. Arrow 2 shows a neuron with a short neurite extending onto glass, and longer neurites extending onto chitosan blended with laminin. Arrow 3 shows a long neurite that returns to the laminin environment after encountering an unmodified chitosan strand.

3.4 Discussion

Laminin is a natural component of the extracellular matrix recognized to promote and guide neurite growth [236]. The main laminin receptors are integrins, which are located at the tips of the filopodia of migrating axonal growth cones [237]. Integrins may not only mediate attachment, but also transmit signals to the actin cytoskeleton within cells [238]. Thus, addition of laminin may improve the affinity of neurons and neurites for a chitosan substrate and improve, or even guide, neurite growth. Blending laminin into chitosan is a rapid, simple, and controllable modification method for scaffold fabrication. The presence of bioactive molecules on the surface and in the interior of the blended material scaffolds may provide positive, even necessary signals for cell and substrate interaction.

In the 4-day cultures of adult DRG neurons on uniform chitosan and chitosan-laminin blended surfaces, better viability of the neurons on both ChLN3 and ChLN6 vs. ChLN0 surfaces was observed, while ChLN3, ChLN6 and Ch+LN

surfaces were not significantly different. This indicates laminin blended into chitosan at low concentrations can improve neuron survival and/or adhesion and therefore improve the prospects for axon growth on chitosan-based tissue engineering scaffolds [239]. Notably, however, no significant difference was found in how the two concentrations of laminin affected the survival and/or attachment of neurons in these initial experiments.

The studies of neuron cultures on uniform surfaces yielded a somewhat different result when the effect of laminin on actual neurite outgrowth was examined. No significant difference in neurite length between cultures grown on ChLN0 and ChLN3 material was found, but there was a significant increase in neurite length in response to the ChLN6 material containing a higher concentration of laminin. The laminin concentration of our ChLN3 preparation may be below the minimally effective level for improving neurite growth [107], even though ChLN3 could improve neuron adhesion compared to ChLN0. This implies that neuron cell body attachment and neurite elongation may be differentially sensitive to the concentration of laminin.

In the experiments examining axon guidance, the strand size of the micropatterns was designed to 100 μm due to the fact that the narrower strand compared to the length of the neurite is able to effectively reflect the effect of the micropatterns on axon guidance and the minimum size of the dispenser needle available in the Asymtek system is 100 μm. The oriented growth of neurites was clearly observed in the ChLN0/ChLN6 pattern, but not in the ChLN0/ChLN3 pattern. For scaffolds fabricated with micropatterned laminin, this result implies that a minimum

improvement in integrin-mediated affinity for neurites is necessary to cause preferential orientation of growth along the laminin containing strand. It suggests that this finding can be applied in the design of peripheral nerve repair scaffolds to guide the growth of neurites in a longitudinal direction. Specifically, the designer can select appropriate concentrations of material with high axon affinity for the guidance part of a scaffold, and low axon affinity materials for other parts. Further experiments using 3D scaffolds *in vitro* and *in vivo* will be required to evaluate this prospective technique.

Axon guidance requires that a coordinated presentation of multiple permissive factors is incorporated into tissue engineering scaffold design to promote axon growth. 2D micropatterns, as model systems, have numerous potential applications in nerve tissue engineering [108]. Over the past decade, 2D patterns have been created by photolithography [240, 241] or by soft lithography [242] techniques for the study of axon guidance. DBRP, however, has many unique advantages for axon guidance applications. Compared with lithography methods, DBRP can easily create 2D micropatterns with different chemical features in different areas, and the geometric features of these micropatterns can be easily and well controlled. The 2D micropatterns fabricated by DBRP may also easily be used to develop 3D nerve conduit scaffolds with controllable microstructures. The inner layer strands of the 3D nerve conduit scaffolds could be fabricated using chitosan blended with laminin (or other growth-promoting proteins), while the rest of the strands of the scaffolds could be fabricated using pure chitosan. According to the results from the 2D micropattern

experiments, axons would preferentially grow along the laminin containing pathway (the inner layer strands) in such scaffolds. Meanwhile, the strand structure can also affect the orientation of growth of axons because of the curvature influences of the strand [111]. Ultimately, the DBRP technique has the potential to automate the design and fabrication of patient-specific scaffolds [92] based on the geometric requirements of each case of nerve injury.

3.5. Conclusions

Neurite growth on substrates of chitosan blended with laminin was investigated in cultures of adult DRG neurons. The results show that uniform ChLN6 substrates significantly improved neurite growth compared to ChLN0 or ChLN3 in neuron cultures. The DBRP technique was used to create 2D micropatterns with different biomaterials in different strands for the study of axon guidance. The micropatterns were designed to impart directionality to the growth of neurites *in vitro*. Quantitative analysis of growth vectors showed that DRG neurites preferred to grow along the direction of the ChLN6 strands compared with the ChLN0 strands. These results suggest that orientation of neurite growth can be achieved in an artificially patterned substrate by creating selective high-affinity pathways.

DBRP is a promising technique for fabricating 2D micropatterns and building more complex 3D tissue engineering scaffolds with defined macro- and microstructures [243], with the capacity to precisely position bioactive molecules that may support and direct improved functional outcomes when tissue scaffolds are designed and utilized to assist in the regenerative repair of injured nerves.

CHAPTER 4
DEVELOPMENT AND CHARACTERIZATION OF NOVEL HYBRID POLY(L-LACTIDE)/CHITOSAN SCAFFOLDS*

*This chapter has been published as "Zhu N., Li M.G., Cooper D., Chen X.B. (2011) Development of novel hybrid poly (L-lactide)/chitosan scaffolds using the rapid freeze prototyping technique. *Biofabrication*. 3(3):034105". According to the Copyright Agreement, "the authors retain the right to include the journal article, in full or in part, in a thesis or dissertation".

4.1 Introduction

Made from biomaterial(s), tissue scaffolds are used to facilitate cell growth and transport of nutrients and wastes while degrading gradually themselves. As such, scaffolds have been shown critical to various tissue engineering applications. Ideally, scaffolds must [16, 244, 245]: (1) be easily fabricated into 3-dimensional (3D) structures with different shapes and sizes, (2) possess interconnected pores with appropriate scale for cell migration, new tissue integration, and vascularization, (3) have appropriate mechanical properties to matching those at the site of implantation and handling, (4) be made with controllable biodegradation properties, and (5) exhibit appropriate biochemical properties for cell attachment, differentiation and proliferation. To meet these requirements, various techniques have been developed for the scaffold fabrication, including both conventional and rapid prototyping (RP)-based techniques. Conventional techniques, such as leaching, gas foaming, solvent casting, melt molding, and phase separation, have several limitations in fabrication process; they are incapable of controlling pore geometry, spatial distribution of pores, and construction of internal channels within the scaffolds [92].

In contrast, RP-based techniques, in which a 3D scaffold is manufactured by laying down multiple, formed layers in succession based on the use of computer-aided design information [246], has been shown be promising for the development of scaffolds.

Dispensing-based rapid prototyping (DBRP) technique is one of the RP-based techniques and has advantages over others in its ability of providing more accurate control on scaffold microstructure. During DBRP process, biomaterials in a fluid form are delivered to build scaffolds in a controllable manner [216]. Specifically, biomaterials are continuously extruded from a fine needle, forming strands to build 2-dimensional (2D) or 3-dimensional (3D) micropatterns of scaffolds [216, 219]. The DBRP technique has been widely applied in tissue scaffold fabrication [177, 247-249]. With the need to develop advanced tissue scaffolds, the DBRP technique has been challenged by the facts that (1) the diameter of strands cannot be too small (typically greater than 100 μm) [247, 250], (2) high temperatures are present in dispensing melted polymers for the scaffold fabrication, which limits the incorporation of bioactive molecules in the scaffolds, and (3) the mechanical properties of polymer solution must be high enough to form 3D structure [216, 246], meanwhile without causing the difficulty in dispensing. To overcome these challenges, rapid freeze prototyping (RFP) technique has shown to be promising [251, 252], in which the polymer solution is dispensed on substrates with a controllable temperature, where the strands formed are frozen and lyophilized to remove the solvent. Compared to DBRP fabrication techniques, RFP technique has the advantage of fabricating tissue

scaffolds with, simultaneously, both sub-millimeter and micrometer levels of pores. Also, under low fabrication temperature, RFP technique can preserve and maintain the bioactivities of biomolecules encapsulated in the scaffolds.

This study reports the use of the RFP technique in the development of a novel hybrid poly (L-lactide)/chitosan scaffold for potential applications in tissue engineering. Poly (L-lactide) (PLLA) is a biodegradable polymer which has been widely used as a scaffold material in various tissue engineering applications [253-255]. PLLA exhibits strong mechanical properties and can be easily processed into 3D structure with complex shapes. Chitosan has also been widely applied in biomedical applications [256-258], especially in drug delivery system [259, 260]. Its cationic nature to be pH-dependent can greatly facilitate the retention or accumulation of bioactive molecules with a controllable manner [57]. Inspired by these previous studies, a study on the fabrication of PLLA/chitosan scaffolds was carried out, in which microspheres were made from chitosan or its mixture with bioactive molecules (as an example, bovine serum albumin (BSA) were examined in this study) and then added to the PLLA solution for scaffold fabrication by means of the RFP technique. The so-fabricated scaffolds are expected to have enhanced porous structure (including both sub-millimeter and micrometer levels of pores) and mechanical properties, as well as to provide a better means to control over the release of bioactive molecules via the use of microspheres than direct addition of them into the PLLA scaffolds.

4.2 Materials and Methods

Poly(L-lactide) (PLLA, MW: 10^5, product No.: B6002-2) was purchased from DURECT Corporation (United States). Bovine serum albumin (BSA) was purchased from BIO BASIC INC. (Canada). Chitosan (28191), tripolyphosphate (TPP) (72061), Span 80 (S6760), and paraffin oil (18512) were purchased from Sigma-Aldrich Canada. Acetic acid was diluted at 2% (wt/vol) concentration in distilled water as the stock solution.

4.2.1 Fabrication processes

(1) Chitosan microspheres (CMs)

In the preparation of non-loaded CMs or the CMs without the presence of BSA, chitosan was dissolved in 2% (wt/vol) acetic acid solution (10 ml). The chitosan solution was used as a water phase, while 50 ml liquid paraffin containing 1% (vol/vol) Span 80 emulsifier as an oil phase. The water phase was dispersed into the oil phase by using a magnetic stirrer to form water-in-oil (W/O) emulsion for 30 min with the stirring rate at a speed of 1200 rpm. Thereafter, TPP solution in water (2 ml) with the concentration of 2.5% (wt/vol) was slowly dropped into the W/O emulsion to solidify the chitosan droplets. The crosslinking reaction was allowed to proceed for a time period of 4 hours. The chitosan microspheres were separated by centrifugation, washed two times with isopropyl alcohol, two times with ethanol, one time with water under centrifugation of 3000 rpm and eventually the microspheres were lyophilized.

In the preparation of BSA-loaded CMs, chitosan was dissolved in 2.2% (wt/vol)

acetic acid solution and the chitosan solution (9 ml) was then mixed with a 1 ml of protein solution containing BSA at protein to polymer ratio of 1:50. The BSA loading microspheres were generated by employing the process similar to the one described above, but adding TPP solution (2 ml) with various concentrations (0.5%, 1.25%, and 2.5% wt/vol) to the chitosan solution mixed with BSA.

(2) Fabrication of solid-strand (SS) scaffolds by using DBRP technique

20% (wt/vol) PLLA was dissolved into 1,4-dioxane, and then mixed with 40% (wt/vol) CMs. Once uniformly mixed the mixture was loaded into a syringe of 5 ml on a precision fluid dispensing system (C0720M, Asymtek) for scaffold fabrication [261, 262]. The mixture was then extruded from a needle with a diameter of 240 μm onto glass coverslips layer by layer to form 3D structure scaffolds. The scaffolds became solid once the solvent volatilized. The fabrication process was performed at room temperature and the micropattern of the scaffolds was controlled by the system programming.

(3) Fabrication of porous-strand (PS) scaffolds by using RFP technique

20% (wt/vol) PLLA was dissolved into 1,4-dioxane, and then mixed with 5% (wt/vol) non-loaded CMs. The fabrication process used to fabricate the PS scaffold by RFP is similar to the one by DBRP, except the temperature of the glass coverslips was controlled under -70 °C using dry ice; the polymer solution can be frozen after it was extruded on the coverslips. The 3D structure of the scaffolds can be preserved. The

frozen scaffolds were lyophilized to remove the solvent.

4.2.2 Characterization of chitosan microspheres and scaffolds

(1) Scanning electron microscopy (SEM)

The morphological features of the SS and PS scaffolds and CMs were investigated by means of scanning electron microscopy (SEM, EVO60, ZEISS). The samples were coated with gold using a Denton VACUUM DESK IV coater and the SEM images were captured with an accelerator voltage of 20 kV.

(2) Microsphere size measurement

The mean values of the CM diameters after drying were measured by laser diffractometry. Freeze-dried CMs were re-dispersed in distilled water and sized by laser diffractometry using a Mastersizer (Malvern Co., UK).

(3) Micro-computed tomography (μCT)

The architecture of the SS and PS scaffolds were analyzed by using a desktop μCT scanner (1172; SkyScan, Belgium) with a pixel size resolution of 3.46 μm. The x-ray source was set at a voltage of 40 kVp and beam current at 250 μA; the integration time used to acquire a single projection was 400 ms. Isotropic slice data were obtained by the system and reconstructed into 2D XY slice images. Approximately 1000 projections per sample were compiled over a rotation range of 180° with a rotation step of 0.20°. Data sets were reconstructed using standardized cone-beam reconstruction software (NRecon v.1.4.3, SkyScan). The image data was used for

morphometric analysis (CT-Analyser v.1.10.10, SkyScan) on the scaffolds and to build 3D virtual models (CT-Volume v.2.1, SkyScan). The morphometric analysis included porosity, scaffolds interconnectivity, surface/volume ratio, and respective pore size and wall thickness distribution.

(4) Fourier transform infrared spectroscopy (FTIR)

The infrared spectra of the PLLA and PLLA/CMs PS scaffolds were measured with an FTIR (FT-IR 4100, JASCO) spectrophotometer. Each spectrum was acquired in attenuated total reflection (ATR) by accumulation of 32 scans with a resolution of 4 cm^{-1} in the spectral range of 4000 - 400 cm^{-1}.

4.2.3 Tests of mechanical properties

To study the mechanical properties of the PLLA/CMs scaffolds, the compressive mechanical properties of the lyophilized scaffolds were tested with an ElectroForce 5010 BioDynamic test instrument (BOSE Corporation - EletroForce System Group, United States). The cylindrical specimens were prepared with a diameter of 8mm and a height of 10 mm. Crosshead speed of 0.5 mm/min was used in the mechanical tests and the compression modulus was determined from the linear part of the stress versus strain curve. Three specimens were tested for each sample and their average values were used for data analysis.

To study the effect of cryogenic temperature used in the RFP fabrication process on the scaffold mechanical properties, the PLLA scaffolds lyophilized at -80, -40, -20, and 0°C, respectively were examined in the test of mechanical properties. Also, to

study the effect of different ratios of PLLA to CMs on the scaffold mechanical properties, the lyophilized PLLA/CMs scaffolds were used in the mechanical tests. Specifically, 20% (wt/vol) PLLA was dissolved into 1,4-dioxane, and then mixed with the non-loaded CMs at the ratio of CMs to PLLA being: 0%, 10%, and 25% (wt/wt), respectively.

4.2.4 BSA release *in vitro*

(1) BSA release from chitosan microspheres

The *in vitro* BSA release profiles of CMs were examined. Specifically, 10 mg of BSA-loaded CMs were re-suspended in phosphate buffered saline (PBS) (1 ml, pH 7.4) in each centrifuge tube, then were placed in a thermostatic shaker (37 °C, 150 rpm). At intervals of 2, 10, 24, 48, 72, 96, 120, 144, and 169 hours, samples were taken out of the thermostatic shaker and centrifuged at a speed of 8000 rpm for 5 min; 0.5 ml of the supernatants from each tube were then carefully transferred to a quartz cuvette for the measurement of the BSA concentration. Each sample tube, then, was added with equal volume (0.5 ml) of fresh PBS to top up to the original volume. The BSA concentration of the supernatant was analyzed by using the UV spectrophotometry (Ultrospec III, Pharmacia, United Kingdom) at 280 nm using supernatant of non-loaded CMs as basic correction. For each condition, at least three samples were used.

(2) BSA release from PLLA/chitosan microspheres

The lyophilized PLLA scaffolds with BSA-loaded CMs (PLLA/CMs-BSA) were used for the study of BSA release. Specifically, 20% (wt/vol) PLLA was dissolved into 1,4-dioxane, and then mixed with the BSA-loaded CMs at the ratio of CMs to PLLA being 10% (wt/wt); the BSA-loaded CMs were crosslinked by adding 2.5% wt/vol TPP solution as described in section 4.2.1(1). The *in vitro* BSA release profiles of PLLA/CMs-BSA scaffolds were then examined. Specifically, 100 mg of the PLLA/CMs-BSA scaffolds were dipped in PBS (2.5 ml, pH 7.4) and kept in a thermostatic shaker (37 °C, 150 rpm). At intervals of 2, 4, 6, 8, 14, 20, 26, and 32 days, 2.5 ml supernatant was collected from each sample for the measurement of the BSA concentration as described above and equal amount of fresh medium was added to each sample to top up to the original volume. For each condition, at least three samples were used.

4.2.5 Statistical analysis

An unpaired t-test was used to evaluate the results using Origin Pro 7.5 (OriginLab) software. Repeated-measure statistical analysis was employed to analyze the data for each of the character parameters. In all evaluations, $p < 0.05$ was considered to be statistically significant.

4.3. Results and discussion

4.3.1 Scaffold fabrication

The CMs were fabricated by using water-in-oil (W/O) emulsification method

(Figure 4.1.a), and the mean values of the CM diameter was determined as 9.51 μm by using laser diffractometry. Figure 4.1.b shows the SEM image of the non-loaded CMs.

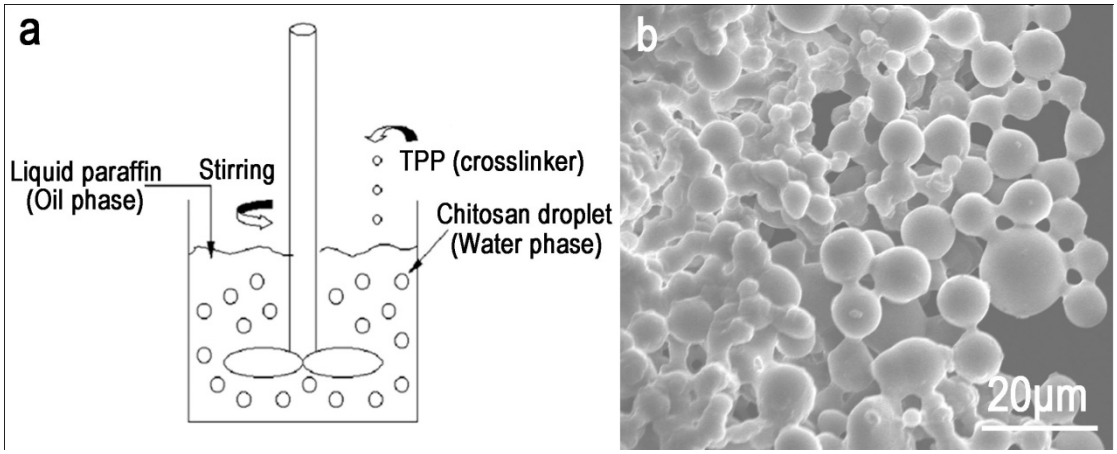

Figure 4.1. Fabrication of chitosan microspheres (CMs); (a) schematic of emulsification method for the CMs fabrication and (b) SEM image for the non-loaded CMs.

After adding the CMs into PLLA solution, the PS scaffolds were fabricated by using RFP technique shown in Figure 4.2. Compared with DBRP fabrication process, the RFP process needs to control the substrate temperature at low levels, so that the polymer strands become solid after the freezing process rather than the use of solvent volatilized process. Consequently, the diameter of the strands in the PS scaffolds (about 250 μm) is bigger than that in the SS scaffolds (about 200 μm) by using the identical size of the needle (Figure 4.3.a and c). Figure 4.3.b and d show the cross-section views of the SS scaffold strand and the PS scaffold strand, respectively. The strands of the PS scaffolds shows interconnected porous structure in a micrometer level, which is , however, hardly observed in the SS scaffold strands.

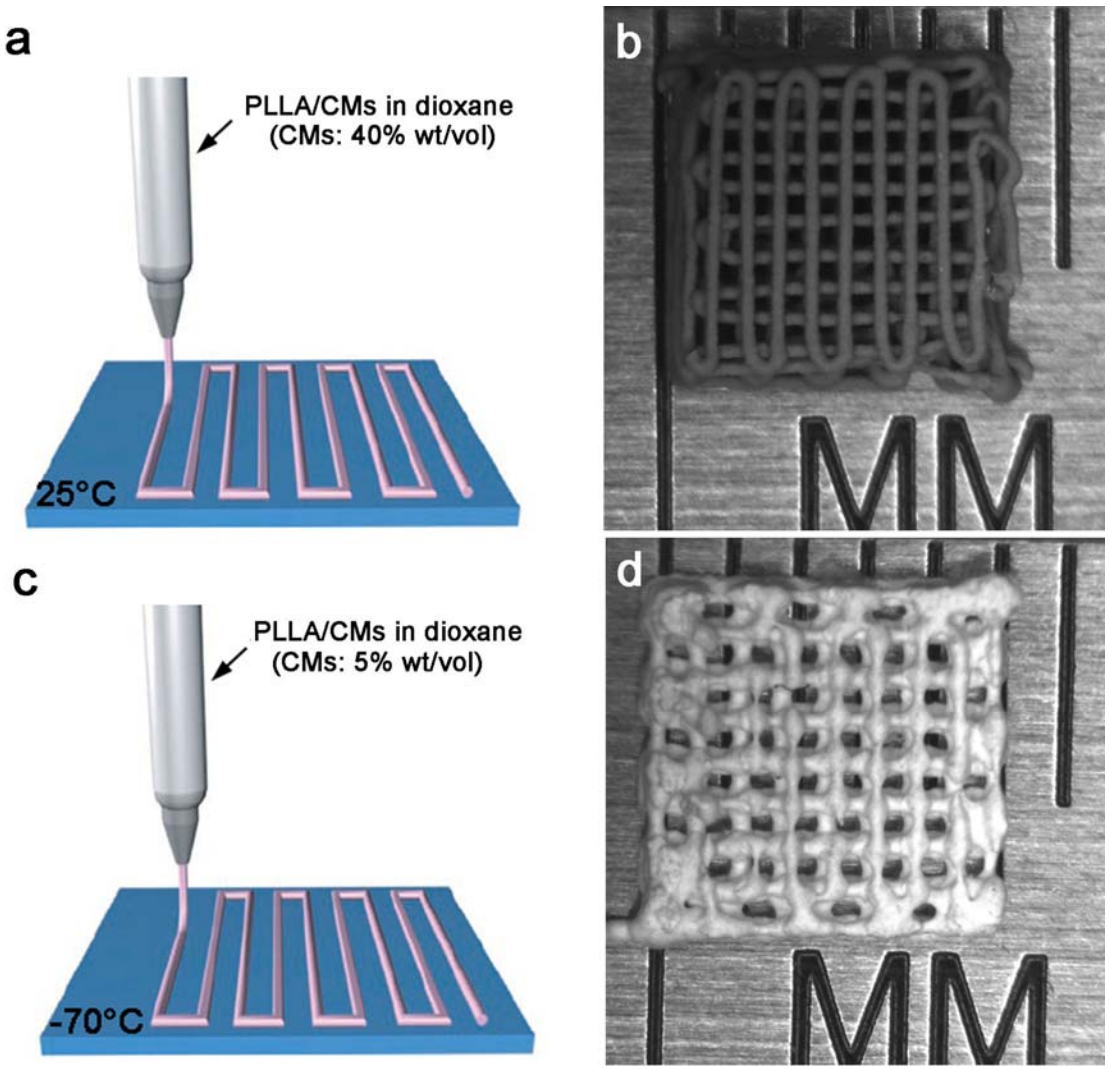

Figure 4.2. Fabrication of the solid-strand (SS) and porous-strand (PS) scaffolds; (a) schematic of the rapid prototyping technique for fabricating a SS scaffold; (b) camera image of a SS scaffold; (c) schematic of the rapid freeze prototyping technique for fabricating a PS scaffold; and (d) camera image of a PS scaffold.

When using the DBRP technique for the PLLA/CMs scaffold fabrication, it was found that the concentration of the particles (CMs) in the polymer solution needed up to 40% in order to enhance the mechanical properties for the formation of 3D structure. It reflects that the polymer solution must be prepared with the yield stress high enough to build scaffold with 3D structure [216]. All of these suggest the addition of the particles into the polymer solution is essentially needed in the

fabrication process by means of the DBRP technique. In contrast, the RFP technique can eliminate the addition of the particles due to the use of the freezing process and as such, it is a process independent of the particle concentration to fabricate 3D scaffolds.

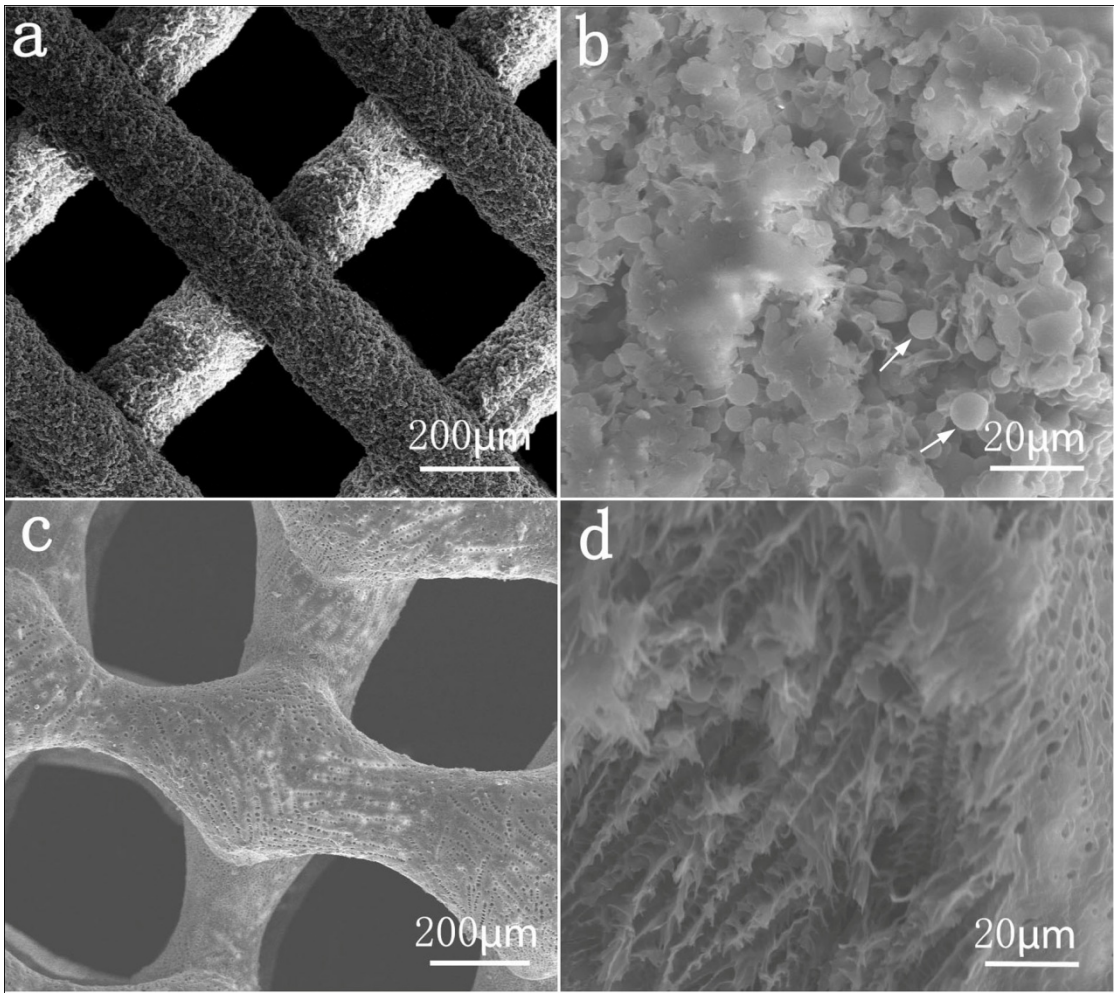

Figure 4.3. SEM images of the solid-strand (SS) and porous-strand (PS) scaffolds; (a) top view of the SS scaffold; (b) cross-section view of the SS scaffold and the arrows show the CMs in the PLLA strand; (c) top view of the PS scaffold strand; and (d) cross-section view of the PS scaffold strand.

It is well known that tissue scaffolds should be able to carry and release bioactive molecules, such as growth factors, in order to support and improve the attachment, proliferation, and differentiation of cells. Thus, maintaining the bioactivities of such

molecules during fabrication process may be needed. The DBRP process is carried out at high temperature or room temperature, which may cause the loss of molecular bioactivities. In contrast, the RFP process is performed at low temperature environment, which is beneficial for preserving the bioactivities of molecules in the scaffold fabrication.

4.3.2 Analysis on the scaffold porous structure

Using μCT technique, the 3D microstructure of the PS and SS scaffolds were reconstructed, as shown in Figure 4.4. a and b. The porous structure features of the scaffolds were quantified based on the μCT image data. Table 4.1 shows the pore parameters of the PS and SS scaffolds. Both types of scaffolds a show highly interconnected structure, while the PS scaffolds have higher porosity and surface/volume ratio than the SS scaffolds. Figure 4.4.c shows the pore size distribution of the different scaffolds. It is seen that there are not only the macro size pores (150-400μm) but micro size pores (5-50 μm) in the PS scaffolds, while the main pore size ranges of the SS scaffolds and lyophilized scaffolds are only from 200 μm to 400 μm and from 50 to 100 μm, respectively. Figure 4.4.d shows wall thickness of the PS and SS scaffolds, indicating that the wall thickness ranges for SS and PS scaffold are from 100 to 150 μm and from 20 to 30μm, respectively. During DBRP, the SS scaffolds solidify by means of the solvent volatilization; the wall thickness of the SS scaffold mainly depends on the diameter of the scaffold strand and/or the diameter of dispenser needle. Compared to the SS scaffolds, the PS scaffolds have much thinner

wall thickness. The PS scaffold strands have porous microstructure due to the lyophilization process; the wall thickness of the PS scaffolds reflects the microstructure inside the individual strands of the PS scaffolds. The results indicate that with the RFP technique, the PS scaffolds can be fabricated with high porosity, enhanced pore size distribution, and thinner wall thickness.

Previous research has shown that the growth of large organized cell communities requires optimized porous structure of the scaffolds [263]. This suggests that wide pore size distributions of the PS scaffolds may maximize cell utilization and permit spatially uniform tissue regeneration. The surface/volume ratio of the PS scaffolds is higher than that of the SS scaffolds. After the bioactive molecules are encapsulated into the scaffolds, high surface/volume ratio can result in the high efficiency of the biomolecules release from the scaffolds *in vivo*. Considered the effect of wall thickness of the scaffolds on scaffold degradation, the thinner the wall thickness of scaffold, the better controlled the degradation of scaffold can be. The surface of scaffolds exposed in biological environment may have different degradation rate from the unexposed parts of scaffolds *in vivo* because of the effect of biological environment on scaffold degradation. PLLA usually undergoes self-catalyzed degradation caused by its acidity production and acidity production of PLLA results in enhanced degradation. So the degradation rate at PLLA surface can be slower than that in the interior [264]. The PS scaffolds with the thin wall structure may facilitate uniform degradation of the scaffolds compared to the SS scaffolds.

Table 4.1. Porous structure comparison of the porous-strand (PS) scaffolds to the solid-strand (SS) scaffolds.

Scaffold Type	Closed Porosity* (%)	Total Porosity (%)	Surface/Volume Ratio (μm^{-1})
SS scaffolds	0.19	67.8	0.024
PS scaffolds	0.0098	82.5	0.143

* Closed porosity: the ratio of the closed pore volume to the total scaffold volume.

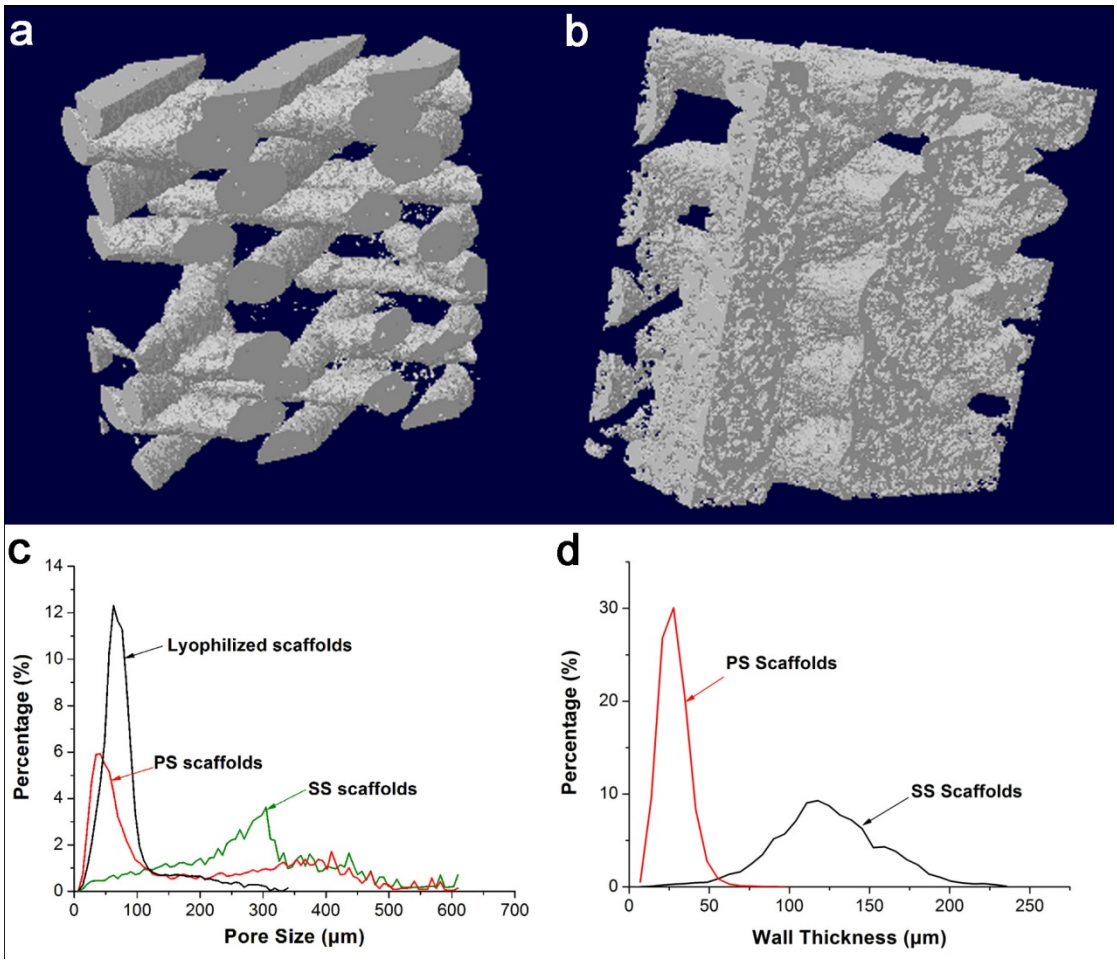

Figure 4.4. Analysis on the porous structure of the porous-strand (PS) and solid-strand (SS) scaffolds using micro-tomography; (a) and (b) are the 3D reconstructed model of the SS and PS scaffolds, respectively, (c) the pore size distribution of the PS, SS, and lyophilized scaffolds, and (d) the wall thickness of the PS and SS scaffolds.

4.3.3 ATR-FTIR spectroscopy

In Figure 4.5, compared to the FT-IR spectrum of PLLA, the spectrum of the obtained PLLA/chitosan presented new absorption peaks around 1540, and 1650 cm^{-1},

which were assigned to the N–H bending vibration of amide II band and the carbonyl stretching of amide I band of the CMs, respectively. After the CMs were mixed mechanically with PLLA (Figure 4.1b), the values of frequencies of these bands hardly change. But the new bands, arising from N–H bending, appears at 1520 and 1558 cm^{-1}, the reason of which might be that a little PLLA was bonded with the chitosan by their molecular force. So the CMs can reinforce the material to a little extent.

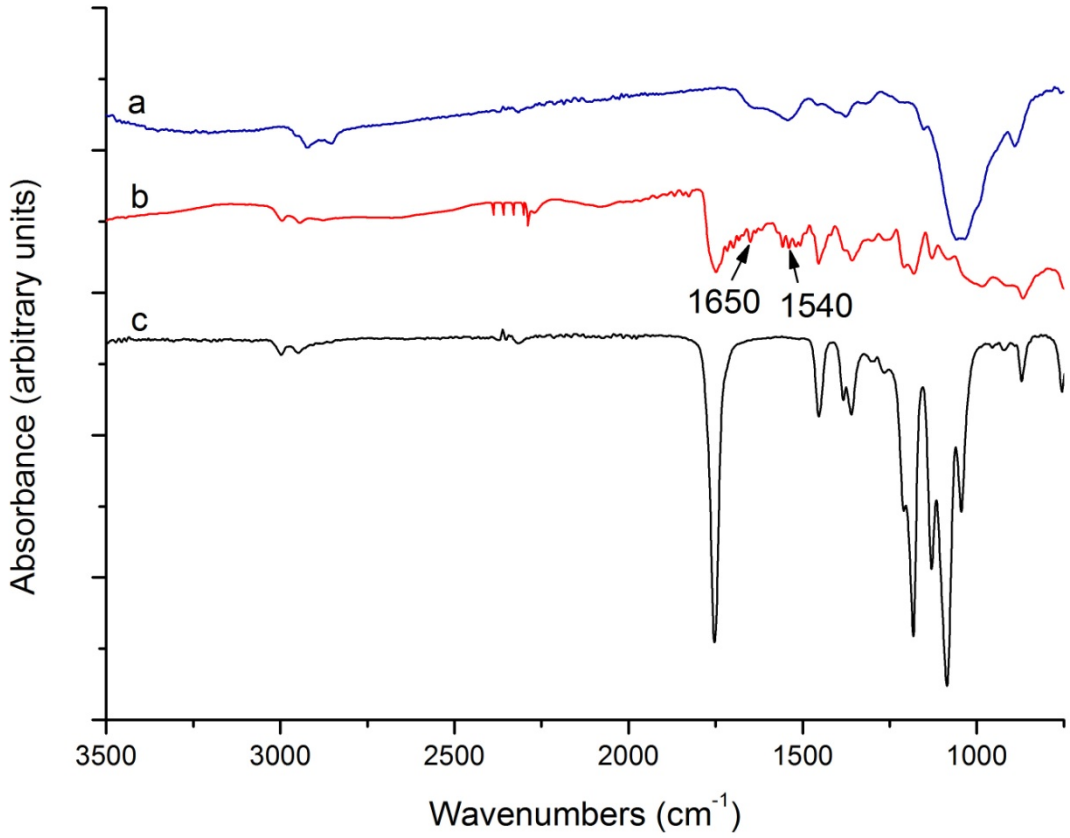

Figure 4.5. FTIR spectra of: (a) non-loaded chitosan microspheres (CMs); (b) PLLA/CMs porous-strand (PS) scaffolds; and (c) PLLA scaffolds.

4.3.4 Mechanical properties

Tests on the scaffold mechanical properties were carried out to investigate the effect of cryogenic temperature and the ratio of CMs to PLLA on the mechanical properties

of the PS scaffolds during the RFP fabrication process. Figure 4.6.a shows the compression modulus of PLLA scaffolds fabricated under different cryogenic temperatures (-80, -40, -20, and 0°C). The results showed that compression modulus of the scaffolds increased with the decrease of the cryogenic temperatures. After mixing CMs into PLLA solution, the result shown in Figure 4.6.b indicated that the compression modulus of the scaffolds increased with the increase of the ratios of CMs to PLLA.

The mechanical properties of tissue scaffolds are of great importance in tissue engineering applications due to the necessity of structural stability to withstand stress incurred during the implantation of the scaffolds *in vivo*. The mechanical properties can also significantly influence the specific biological functions of cells within the engineered tissue [265, 266]. This study demonstrates that the mechanical properties of the PS scaffolds can be controlled by adjusting the cryogenic temperatures. Lower cryogenic temperature can speed up the heat transfer rate and affect the crystal growth, leading to the smaller mean pore size of the scaffolds [226]. As a result, the compression modulus of the scaffolds can be increased. In addition, as discussed previously the formation of 3D structure by means of the RFP technique, the PS scaffolds are independent of the ratios of CMs to PLLA. The dependency of mechanical properties on the ratio of CMs to PLLA allows for the selection of its value in a more wider range so as to achieve the desired mechanical properties for a particular tissue regenerative application.

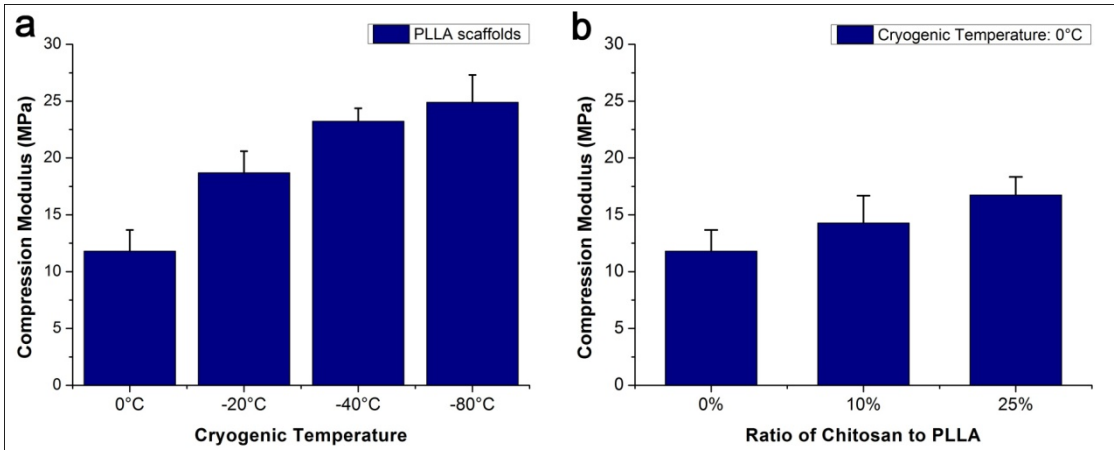

Figure 4.6. Compression modulus of the two kinds of lyophilized scaffold samples; (a) PLLA scaffolds fabricated under different cryogenic temperatures: -80, -40, -20, and 0°C, respectively and (b) PLLA/CMs scaffolds fabricated under the cryogenic temperature of 0°C with different ratios of CMs to PLLA, i.e., 0%, 10%, and 25% (wt/wt).

4.3.5 *In vitro* BSA release

In the investigation of the BSA release profile, the BSA-loaded CMs treated with different concentration TPP solutions (i.e., 0.5, 1.25, and 2.5% (wt/vol)) were incubated in PBS pH 7.4, 37 °C for one week. Figure 4.7. shows the BSA release kinetics from the CMs. It is seen that the release profile is different, depending on the TPP concentration. Particularly, the percentage of the BSA release in the first 24 h is 73.6±0.8% for the 2.5% TPP crosslinked CMs, 89.6±4.3% for the 1.25% TPP, and 94.2±2.4% for the 0.5% TPP. Compared to 1.25% and 0.5% TPP crosslinked CMs, the initial burst release of the 2.5% TPP was significantly different ($p<0.01$) in the first 24 h of release process. High initial burst release is problematic in most protein delivery applications because dose dumping is both inefficient and potentially harmful to the target tissue [267]. The results suggest that the higher TPP concentration causes higher crosslinking degree of CMs and delays protein diffusion across the phase

boundary to reduce the initial burst release. The crosslinking process of chitosan - TPP is predominantly ionic cross-linked [268]. TPP containing negative charges ($P_3O^{5-}_{10}$ ions) interact with the $-NH^{+}_{3}$ amino groups of chitosan. During the BSA release process (pH=7.4), BSA surface shows negative charges, which will avoid the effect of TPP on BSA release.

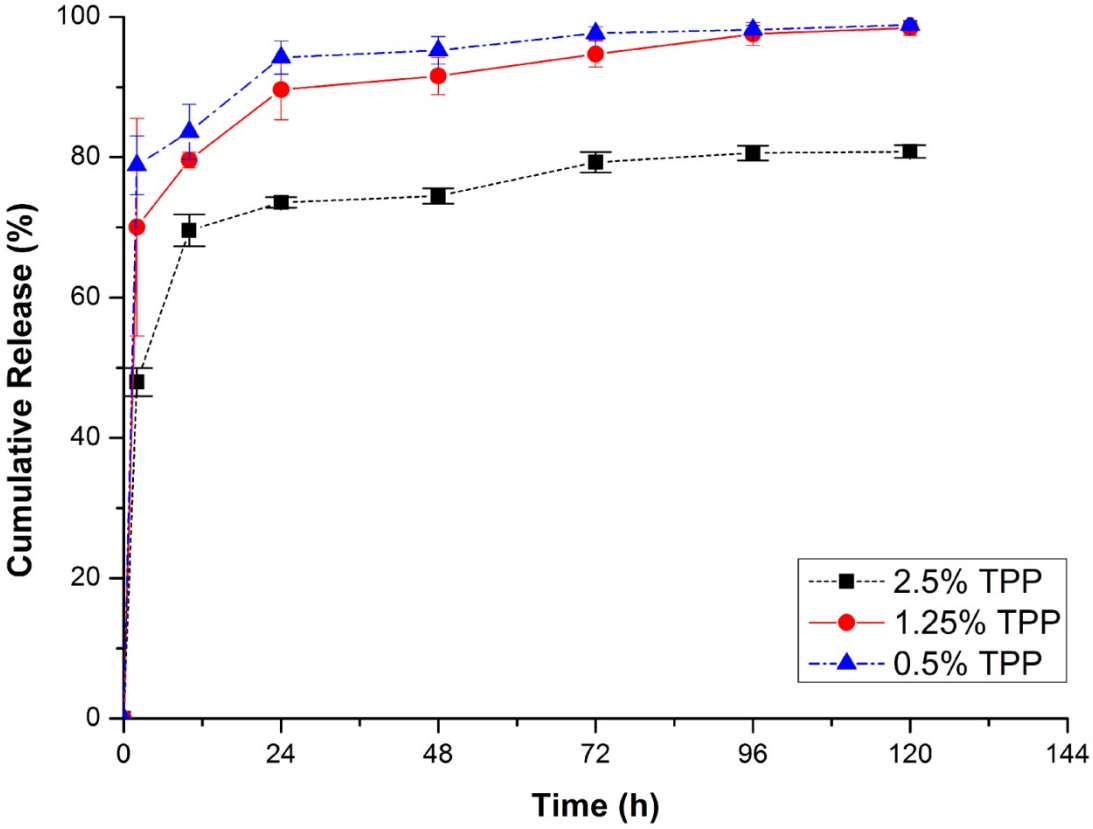

Figure 4.7. BSA release from chitosan microspheres in PBS pH 7.4, 37 °C. Chitosan/BSA microspheres (50:1 wt/wt) were prepared by emulsification method crosslinked by tripolyphosphate (TPP) solution with concentrations of 0.5, 1.25, and 2.5% (wt/vol), respectively. Values represent means and standard deviations (n=3).

In the investigation of BSA release from PLLA/CMs-BSA scaffolds, the BSA loaded CMs crosslinked by 2.5% TPP were used to mix into PLLA scaffolds. The same content of BSA-loaded CMs was used for both BSA release from free floating CMs and PLLA/CMs scaffolds. From the BSA release profile shown in Figure 4.8,

the complete release of BSA from the PLLA/CMs-BSA scaffolds took 34 days and about 49.0±2.1% BSA was released in the first 4 days. In contrast, BSA release from free floating CMs in Figure 4.7. is 80.6±1.0% in the first 4 days, which is significantly higher ($p < 0.01$) than that from the PLLA/CMs-BSA scaffolds. After embedding CMs into PLLA scaffolds, the BSA release period can be prolonged because the BSA release from PLLA occurred by a combined diffusion-degradation mechanism.

In tissue engineering, the bioactive molecules need to be gradually released from scaffolds during the period of new tissue regeneration. The use of CMs to carry the bioactive molecules can better encapsulate, control, and manipulate biomolecules from PLLA PS scaffolds compared to the scaffolds directly encapsulating the bioactive molecules. The crosslinking degree can affect chitosan bioadhesive properties and release of the biomolecules [269]. The BSA initial burst release, therefore, can be controlled by the treatment with different crosslinking degree. Meanwhile, the PLLA/CMs system can prolong protein release process. The long-term protein release is beneficial to promote and maintain functional recovery in tissue engineering applications, such as nerve [102] and bone [270] tissue engineering. Furthermore, the combination of RFP technique with the use of CMs provides an effective way of controlling the biomolecule distribution and the total biomolecule encapsulation content in the scaffolds. The different biomolecule-loaded CMs can be placed into the specific designed strands of the scaffolds using RFP system with muti-nozzle dispensers [252]. The total biomolecule encapsulation content in the PLLA/CMs PS scaffolds can be adjusted by means of choosing a percentage of

BSA-loaded CMs in the RFP dispenser/syringe and independent of biomolecule encapsulation efficiency of CMs. The RFP/CMs system shows the potential to improve the control of the biomolecule release in the scaffolds.

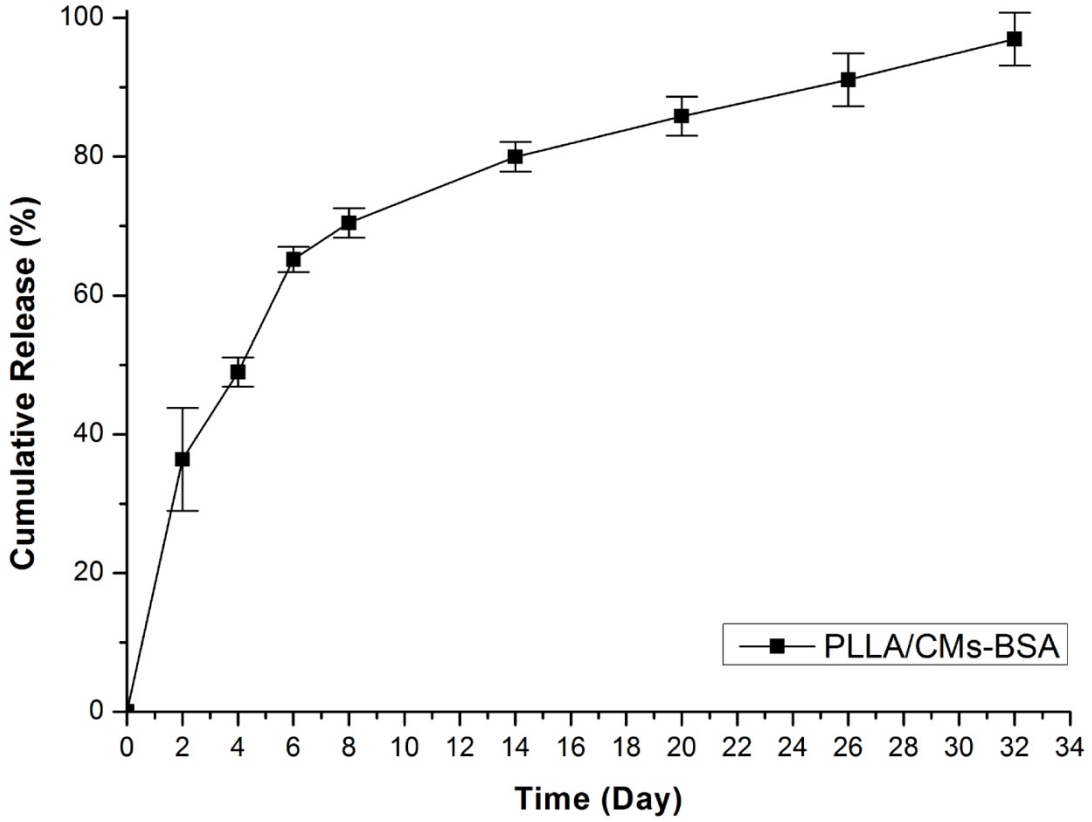

Figure 4.8. BSA release from the PLLA/CMs-BSA scaffolds in PBS pH 7.4, 37 °C for 32 days. Values represent means and standard deviations (n=3).

4.4. Conclusions

This paper presents the development of a novel three-dimensional scaffold made from the mixture of CMs and poly (L-lactide) by means of the RFP technique. Compared to the DBRP technique, the RFP technique is able to achieve improved porous structure of scaffolds, which includes higher porosity, enhanced pore size distribution, and thinner wall thickness. The improved porous structure would

facilitate cell and tissue migration and vascularization. In the novel PLLA/chitosan scaffolds, the CMs are used to encapsulate and release bioactive molecules. The FTIR results show the CMs were mechanically mixed into the PLLA scaffolds. The experimental results of the BSA release demonstrate that the use of the CMs is an effective way to administrate the BSA release and that its rate can be controlled by adjusting the crosslinking degree of the CMs; the BSA release period can be prolonged after the CMs are embedded into PLLA scaffolds. The experimental results also show the addition of the CMs to the PLLA scaffolds can improve the mechanical properties of the scaffolds, depending on cryogenic temperature used in the scaffold fabrication process. The present study demonstrates that the novel PLLA/chitosan scaffolds fabricated by using the RFP technique have enhanced porous structure and mechanical properties. The RFP technique shows the potential to preserve the bioactivities of the biomolecules in the scaffolds.

CHAPTER 5
A STUDY ON THE IN VITRO DEGRADATION OF POLY(L-LACTIDE)/CHITOSAN-MICROSPHERES SCAFFOLDS

5.1 Introduction

Scaffold degradation is one of the key considerations in the design and fabrication of tissue engineered scaffolds. In tissue engineering, biodegradable scaffolds must be able to maintain their physical and chemical characteristics, as well as mechanical properties, in order to support new tissue growth until tissue is regenerated at an injured site. Ideally, the degradation rate of scaffolds should match the rate of new tissue formation, which allows a smooth transition of load transfer from scaffolds to tissue [271]. However, the challenge of scaffold design is to control and adjust scaffold behaviors to meet the requirements of different tissue engineering applications.

Depending on the mode of degradation, polymeric biodegradable biomaterials can be classified into hydrolytic degradable polymers and enzymatic degradable polymers [272]. Most natural polymers undergo enzymatic degradation. The degradation rate of enzymatic degradable polymers varies significantly with the site of implantation and depends on the availability and concentration of the enzymes. On the other hand, degradation of synthetic polymers generally occur due to cleavage of hydrolytic sensitive linkages in the polymer. Synthetic polymers have more predictable properties and batch-to-batch uniformity and their property profiles can be tailored for specific tissue engineering applications. Therefore, they are devoid of many of the disadvantages of natural polymers [66].

Poly (L-lactide) (PLLA) is a type of nontoxic, biodegradable, synthetic polymer, which is widely used as a scaffold material in tissue engineering, such as nerve [30], cartilage [273], and bone [274] tissue regeneration. PLLA undergoes hydrolysis of the ester groups to form the harmless product L-lactic acid. Degradation properties are dependent on several factors, such as molecular weight [275], crystallinity [276], and sample size and shape [277]. These factors can be used to predict and control the degradation behaviors of PLLA scaffolds. However, concerns exist regarding the use of PLLA as the only biomaterial in building tissue scaffolds. PLLA has obvious weaknesses during *in vivo* degradation, i.e., biodegrading too quickly and creation of acidic degradation products [278].

Chitosan is a natural polymer derived from chitin, which is widely found in shells of crustaceans such as crabs and shrimps. It has been shown to have excellent biocompatibility when applied to tissue engineering [53, 279]. Combination of chitosan with synthetic PLLA might overcome some of the drawbacks of PLLA alone [280]. Chitosan, as an alkalescent polymer, can neutralize the acidity generated, thereby eliminating the inflammations which prolongs the exiting of the material from the body. Recently, poly (L-lactide)/chitosan microspheres (PLLA/CMs) scaffolds were successfully developed in the authors' laboratory [281]. CMs added to the PLLA scaffolds may not only improve the biocompatibility and mechanical properties of the scaffolds but also enable manipulate bioactive molecule release from the scaffolds [281]. However, the degradation properties of the composite material scaffolds are still not well understood. Therefore, in the present study, the effect of chitosan

microspheres on PLLA degradation was investigated using weight loss, differential scanning calorimetry (DSC), and Raman spectroscopy. In particular, micro-computed tomography (μCT) was used to monitor and quantify the morphological changes during scaffold degradation. The results were also compared to the degradation behaviors of pure PLLA scaffolds.

5.2 Materials and Methods

5.2.1 Materials

Poly(L-lactide) (PLLA, MW: 10^5 g · mol^{-1}, product No.: B6002-2) was purchased from DURECT Corporation (United States). Chitosan (28191), tripolyphosphate (TPP) (72061), Span 80 (S6760), and paraffin oil (18512) were purchased from Sigma-Aldrich Canada. Acetic acid was diluted with distilled water at a concentration of 2% (wt/vol) for the stock solution.

5.2.2 Scaffold fabrication

(1) Chitosan microspheres (CMs)

To prepare the the CMs, chitosan was dissolved in the 2% (wt/vol) acetic acid solution to obtain 2% (wt/vol) chitosan solution. 10 mL chitosan solution was used as a water phase, while 50 ml liquid paraffin containing 1% (vol/vol) Span 80 emulsifier was the the oil phase. To form water-in-oil (W/O) emulsion, the water phase was dispersed into the oil phase using a magnetic stirrer with a stirring rate of 1200 rpm for 30 min. To solidify the chitosan droplets, a TPP solution in water (2 ml) with a

concentration of 2.5% (wt/vol) was slowly dropped into the W/O emulsion. The crosslinking reaction was allowed to proceed for 4 hours. The CMs were separated centrifugally, washed twice with isopropyl alcohol, twice with ethanol, and once with water using a centrifuge at 3000 rpm. Finally, the microspheres were lyophilized.

(2) Preparation of PLLA/CMs scaffold

The composite porous scaffolds were fabricated using a lyophilization technique. Briefly, a known amount of PLLA was dissolved into 1,4-dioxane to obtain 6% (wt/vol) PLLA solution. This was mixed with the CMs (particle size ~10 μm) at a CMs to PLLA ratio of 25%. The resulting solution was poured into cylindrical molds and frozen below -20°C. The frozen scaffolds were lyophilized to remove the solvent. PLLA scaffolds were fabricated using the same without addition of CMs.

5.2.3 Scaffold degradation *in vitro*

The cylindrical shape PLLA/CMs scaffolds weighing approximately 70 mg were placed in vials filled with 5 mL of phosphate buffered saline (PBS) (pH 7.4). These are incubated *in vitro* using a shaking air bath at 37°C and 100 rpm for 8 weeks. The PBS solution was replaced once a week. At specific time intervals (2, 4, 6, and 8 weeks), parts of the samples were removed from the buffer and washed thoroughly with distilled water, followed by drying at room temperature under reduced pressure for at least 24 hours. The degraded scaffolds were kept in a desiccator until further use. PLLA scaffolds were treated similarly.

5.2.4 Characterization

(1) Micro-computed tomography (μCT)

During degradation, the same scaffold from each group (PLLA/CMs and PLLA) was taken out of the PBS solution at time intervals (0, 6, and 8 weeks) and scanned using a desktop μCT scanner (1172; SkyScan, Belgium) with a pixel size resolution of 3.46 μm. The scaffolds were dried at room temperature under reduced pressure for at least 24 hours before μCT scanning and immersed into the PBS solution again after the scanning.

For microstructure analysis of the degraded scaffolds, the x-ray source was set to a voltage of 40 kVp and beam current of 250 μA. The integration time used to acquire a single projection was 400 ms. Isotropic slice data were obtained by the system and reconstructed into two-dimensional XY slice images. Approximately 1000 projections per sample were compiled over a rotation range of 180° with a rotation step of 0.20°. Data sets were reconstructed using standardized cone-beam reconstruction software (NRecon v.1.4.3, SkyScan). The image data was used for morphometric analysis (CT-Analyser v.1.10.10, SkyScan) of the scaffolds. The pore size thickness distribution of the degraded scaffolds was obtained from the morphometric analysis.

(2) Weight loss

The percentage weight loss of degraded scaffolds was calculated from the weights of the dried scaffolds before and after hydrolysis according to:

$$W_{loss}\ (\%) = (m_0 - m_d)/m_0 \times 100\% \quad (5.1)$$

where W_{loss}(%) is the percentage weight loss of the degraded scaffold; m_0 is the weight of the dried scaffold before degradation, and m_d is the weight of the dried scaffold after degradation.

Three specimens were tested for each sample and their average values were used for data analysis.

(3) Raman spectroscopy

Raman spectra of the degraded scaffolds were obtained and measured with a inVia Raman microscope (RENISHAW Inc., UK). A laser with a 785 nm line was used as the excitation source for the Raman spectra. The exposure time and accumulation for obtaining the Raman spectra were 10 s and 16 times, respectively. The laser power at the sample surface was 100 mW. A curve fit of the spectra was performed using WiRE 3.2 software with a mixture of Gaussian and Lorentz functions.

(4) Differential scanning calorimetry (DSC)

A Q2000 differential scanning calorimeter (TA instruments, U.S.A.) was used to obtain DSC thermograms of the degraded scaffolds. Samples with a mass of approximately 10 mg were first sealed in an aluminum pan. DSC measurements were then performed on samples which were heated from 10°C to 200°C at 10°C/min. Heat of Fusion is directly proportional to crystallinity (χ%) and it was calculated by:

$$\chi\% = \triangle H_f / \triangle H_0 \quad (5.2)$$

where $\triangle H_f$ is the fusion enthalpy of the sample, and $\triangle H_0$ is the theoretical heat of

fusion for crystalline PLLA and it was taken as 135 J/g [282].

5.3 Results

5.3.1 Scaffold microstructure analysis

The microstructural changes of both PLLA and PLLA/CMs scaffolds were monitored by μCT. During scaffold degradation *in vitro*, the scaffold microstructure analysis was based on a sample taken at different time points. After μCT scanning, a three dimensional scaffold model was reconstructed and the pore-structural features were quantified from the model. Figure 5.1a shows the pore size distribution of a PLLA scaffold at 0, 6, and 8 weeks. The peaks of the distribution curves move to the right for samples from 0 to 8 weeks. This means that a large percent of pores were distributed approximately 60 μm before the scaffold degraded, but this changed to approximately 90 μm after degradation for 8 weeks. The result demonstrates that the scaffold degradation led to changes of pore size inside the scaffolds due to the polymer hydrolysis. Figure 5.1b shows the pore size distribution of a PLLA/CMs scaffold at 0, 6, and 8 weeks. The distribution curves do not move significantly during the scaffold degradation, therefore, the pore size distribution of the scaffolds does not significantly change after the scaffold degradation. The results suggest that adding CMs to PLLA causes the degradation rate of the PLLA/CMs scaffolds to be slower than the PLLA scaffolds.

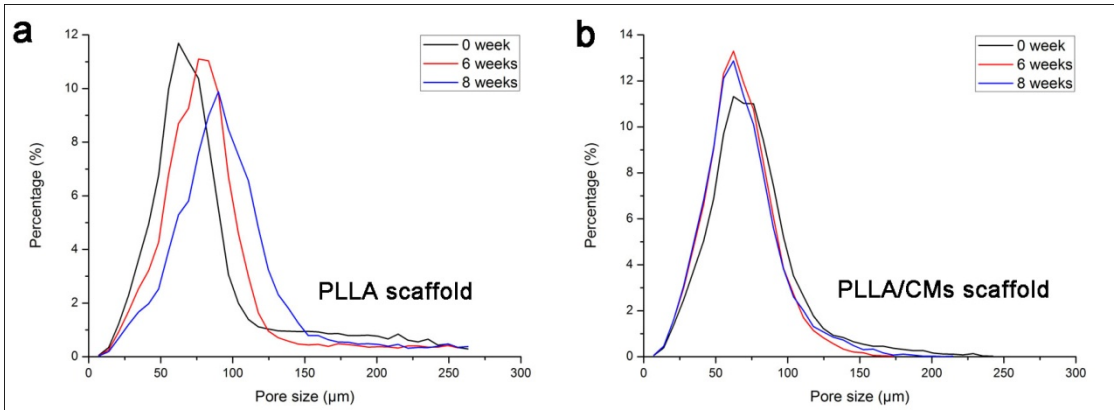

Figure 5.1. Micro-tomography quantitative analysis for pore size distribution of the PLLA (a) and PLLA/CMs (b) scaffolds at time point 0, 6, and 8 week during scaffold degradation in PBS for 8 weeks *in vitro*.

5.3.2 Weight loss

Figure 5.2 shows the mass changes of both PLLA and PLLA/CMs scaffolds, which were monitored during the degradation process. The mass loss of the PLLA scaffolds was approximately 7.6% after 8 weeks, which was higher than that of the PLLA/CMs scaffolds (approximately 5.9%). The weight loss curves indicate that the PLLA scaffolds degrade faster than PLLA/CMs scaffolds throughout the degradation process.

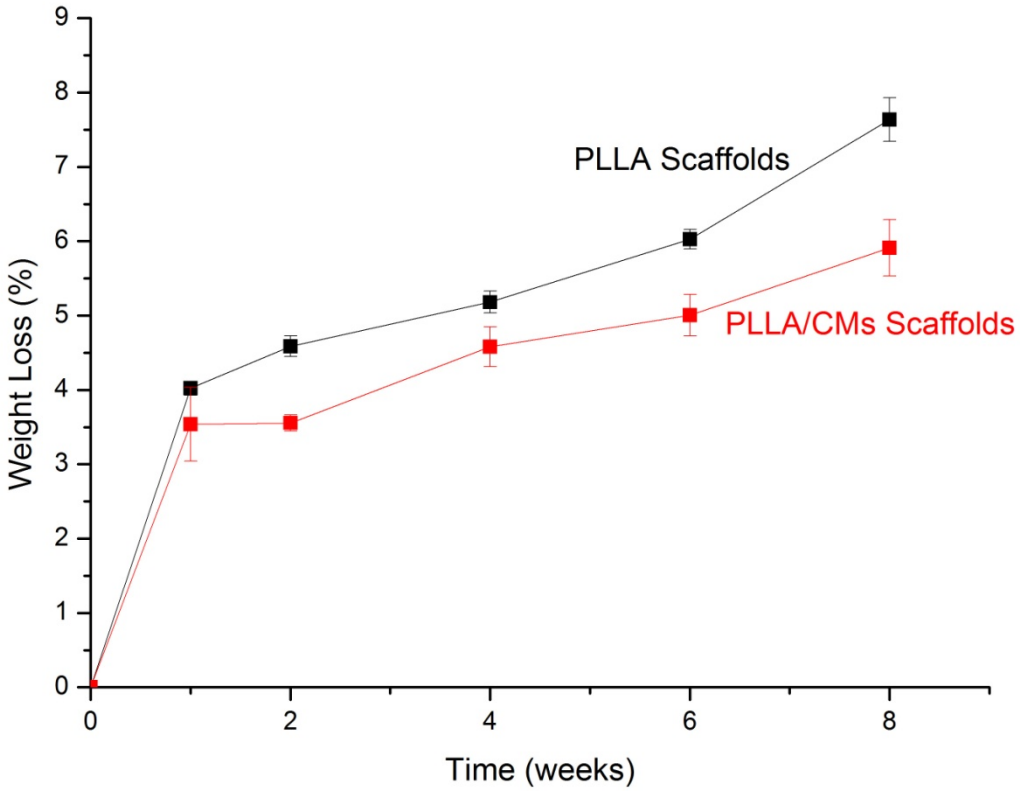

Figure 5.2. Weight loss of the PLLA (a) and PLLA/CMs (b) scaffolds during scaffold degradation in PBS for 8 weeks *in vitro*.

5.3.3 Spectroscopic characterization

Figure 5.3 shows the Raman spectra of a PLLA scaffold before degradation (a) and after degradation for 8 weeks (b) and of a PLLA/CMs scaffold before degradation (c) and after degradation for 8 weeks (d). The spectra of both PLLA and PLLA/CMs presented significant Raman peaks at 875 and 1452 cm^{-1}. These peak positions are consistent with the PLLA spectrum reported in previous research [283]. The $857cm^{-1}$ peak is attributed to the C-COO stretching modes in the chain, while the 1452 cm^{-1} band is attributed to the CH_3 symmetric bending. Previous studies on PLLA showed that the Raman I_{875}/I_{1452} intensity ratio constitutes a spectroscopic marker of the polymeric chain length [284]. The 1452 band can be taken as internal standard.

During PLLA degradation, long PLLA molecular chains break into short ones, which leads to the decrease of the I_{875}/I_{1452} intensity ratio [285]. The Raman I_{875}/I_{1452} intensity ratios of PLLA and PLLA/CMs are shown in Figure 5.4. The Raman I_{875}/I_{1452} intensity ratios for both materials do not significantly change up to four weeks. After 8 weeks of degradation in PBS, Figure 5.4 suggests that the chain length of PLLA decreases more quickly than PLLA/CMs.

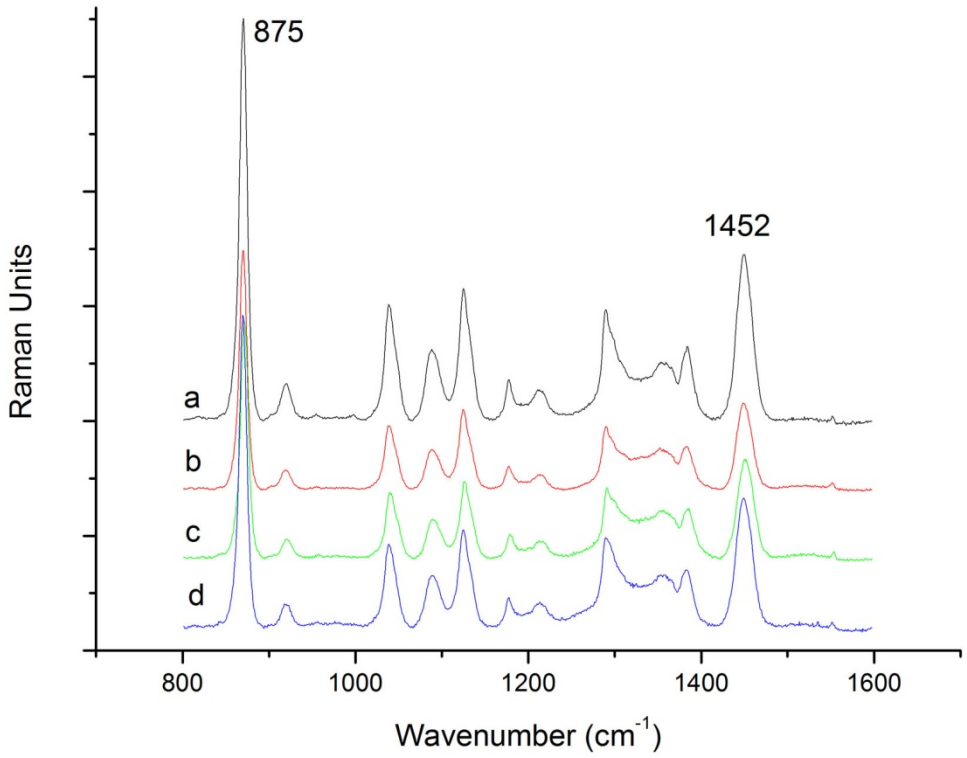

Figure 5.3. Raman spectra of both PLLA and PLLA/CMs scaffolds during degradation in PBS for 8 weeks *in vitro*. (a) PLLA scaffolds degraded for 0 week, (b) PLLA scaffolds degraded for 8 weeks, (c) PLLA/CMs scaffolds degraded for 0 week, and (d) PLLA/CMs scaffolds degraded for 8 weeks.

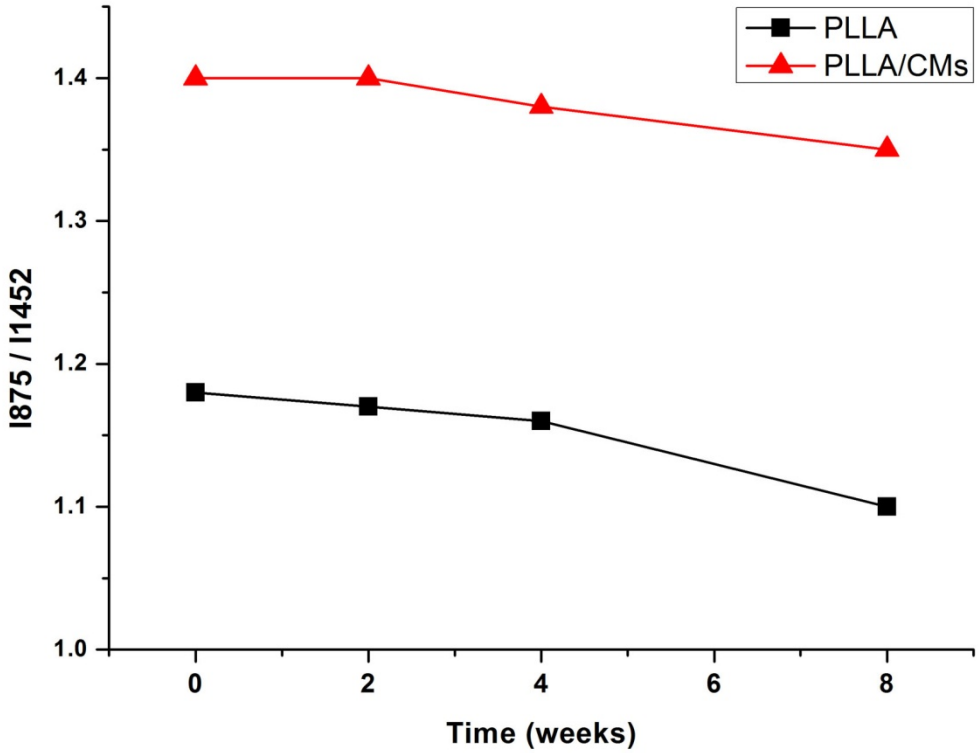

Figure 5.4. Raman I_{875}/I_{1452} intensity ratios for PLLA and PLLA/CMs scaffolds during degradation in PBS for 8 weeks *in vitro*.

5.3.4 Differential scanning calorimetry (DSC)

DSC measurements were performed to further describe the degradation behaviour of PLLA/CMs scaffolds. In table 5.1, the crystallinity (χ%) of PLLA in both PLLA and PLLA/CMs scaffolds were calculated based on the enthalpy of melting (△H) of PLLA from DSC thermograms. The χ% of PLLA in the undegraded PLLA/CMs scaffolds is noticeably lower than that in the PLLA scaffolds. The result demonstrates that adding CMs into PLLA increases PLLA lattice disorder and/or decreases crystalline thickness during scaffold fabrication. During scaffold degradation, the χ% of PLLA in both PLLA and PLLA/CMs scaffolds gradually increased due to the factor that the crystalline residues formed as a result of selective hydrolysis and

removal of the chains in the amorphous state occurred first [286]. The changes of PLLA χ% in both scaffolds are plotted in Figure 5.5 as a function of hydrolysis time. The crystallinity of the PLLA in PLLA/CMs scaffolds increases slightly slower than that in PLLA scaffolds after 4 weeks of degradation. This suggests that the PLLA/CMs scaffolds degrade slower than PLLA scaffolds.

Table 5.1. Thermodynamic characteristics of PLLA and PLLA/CMs after scaffold degradation in PBS in vitro for 0, 2, 4, 8 weeks.

Sample	Time(weeks)	△H(J/g)	χ(%)
PLLA	0	46.12	34.2
	2	46.3	34.3
	4	48.36	35.8
	8	49.14	36.5
PLLA/CMs	0	33.18	24.6
	2	34.29	25.4
	4	35.89	26.6
	8	36.12	26.8

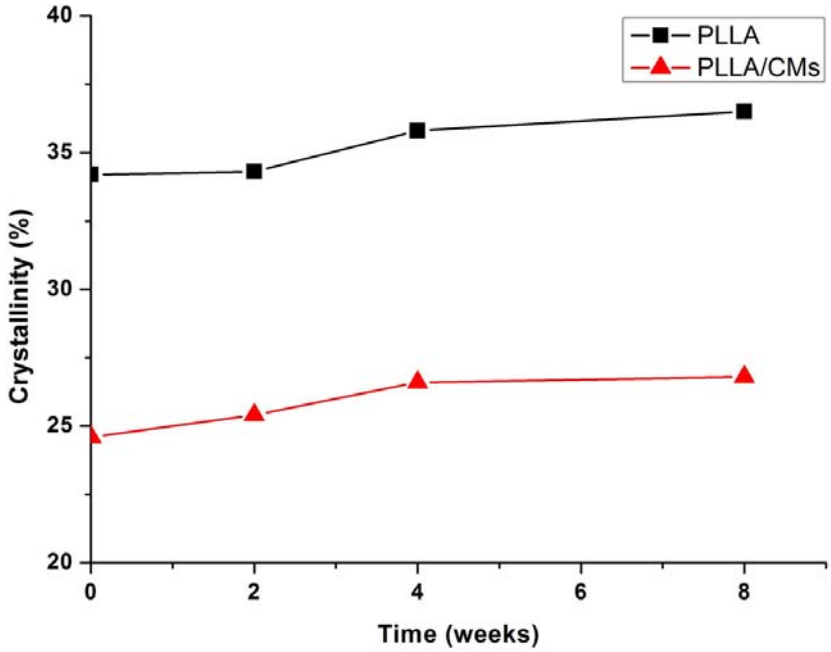

Figure 5.5. Crystallinity (χ%) of PLLA in PLLA and PLLA/CMs scaffolds as a function of degradation time.

5.4 Discussion

The structural features of a scaffold play an important role in new tissue regeneration. Engineered scaffolds fabricated from biodegradable polymers will experience internal and external structural changes during the whole scaffold degradation/tissue growth process. Monitoring structural changes of a scaffold during degradation is a challenge in tissue engineering due to the limitations of conventional invasive methods, such as scanning electron microscopy, light microscopy, mercury intrusion porosimetry, and the gas expansion method. μCT is a non-invasive and non-destructive method, which is able to quantify scaffold microstructural features without damaging the samples. In the study, a μCT was used to monitor PLLA and PLLA/CMs scaffold degradation behaviours. One sample from each group was used for microstructural analysis by μCT and the same sample was monitored at each time point during degradation. Using the same sample ensured that the results would be more comparable and reliable than results obtained from different samples at each time point.

The results from weight loss, Raman spectroscopy, and DSC analysis are consistent with the μCT results, which show that the PLLA/CMs scaffolds degrade more slowly than pure PLLA scaffolds. Chitosan added to PLLA causes a decrease of PLLA hydrolysis. As PLLA degrades, long chain molecules are degraded into short chain molecules and the small molecules in PLLA degradation products are acidic. Therefore, PLLA usually undergoes self-catalyzed degradation caused by its acidity production and this results in enhanced degradation [264]. The alkalescent

degradation products of chitosan can neutralize the acidity generated by PLLA degradation and thereby inhibit the hydrolysis of PLLA [278], which may slow the changes of the Raman I_{875}/I_{1452} intensity ratio in PLLA/CMs during degradation.

The degradation rate of PLLA/CMs scaffolds should be controlled to match the new tissue regrowth according to different tissue injury processes. For example, it took approximately 3 months to bridge 10-mm sciatic nerve defects in rats [62], but over 6 months for the repair of 30-mm-long dog sciatic nerve defects [287]. In nerve tissue regeneration, one of the disadvantages of PLLA scaffold is its rapid degradation based on the hydrolysis of the polyester bond [288]. Adding chitosan microspheres into PLLA scaffolds can decrease the hydrolysis rate of PLLA. This factor combined with other factors, such as, polymer molecular weight, crystallinity, shape, and wall morphology, can be used to adjust and/or control the degradation behaviours of PLLA scaffolds in order to meet the requirements of specific tissue engineering applications.

5.5 Conclusions

The results obtained from *in vitro* degradation experiments of PLLA/CMs scaffolds showed that there was a decrease in the degradation rate of the composite scaffolds in phosphate-buffer solution with pH 7.4 at 37°C after 8 weeks compared with pure PLLA scaffolds. The addition of CMs into PLLA slowed the hydrolysis of PLLA after 4 weeks degradation and also resulted in the decrease of PLLA crystallinity during scaffold fabrication. The biodegradation behavior of PLLA can be regulated and adjusted by adding CMs.

The μCT technique employed in the present work is capable of monitoring microstructural changes of scaffolds during degradation. This new application allows a deeper insight towards understanding scaffold degradation behavior and possible visualization of new tissue growth as well.

CHAPTER 6
X-RAY DIFFRACTION ENHANCED IMAGING AS A NOVEL METHOD TO THE VISUALIZATION OF PLLA/CHITOSAN SCAFFOLDS FOR SOFT TISSUE ENGINEERING APPLICATIONS*

*This chapter has been accepted for publication as "Zhu N., Chapman D., Cooper D., Schreyer D.J., Chen X.B. (2011) X-ray diffraction enhanced imaging as a novel method to visualize low-density scaffolds in soft tissue engineering. T*issue Engineering Part C*. 17(11): 1071-1080". According to the Copyright Agreement, "the authors retain the right to include the journal article, in full or in part, in a thesis or dissertation".

6.1 Introduction

In tissue engineering, biomedical imaging techniques play an important role in the characterization of biomaterials, scaffolds, cells, and engineered tissue [289]. Conventional imaging techniques applied in tissue engineering include scanning electron microscopy (SEM), transmission electron microscopy (TEM), and confocal laser scanning microscopy (CLSM). SEM has become a standard visualisation method for morphology elucidation and is widely used to reveal scaffold microstructures [117, 126] and cell-substrate interactions [135]. However, as a two-dimensional (2D) visualization tool the utility of SEM for quantitative analysis and characterization of three-dimensional (3D) structures is limited. TEM is another electron microscopy technique used to obtain images in nanometer scale. As such, it enables the observation of regenerative tissue at the cellular level [139, 140]. However, the disadvantages of TEM include the need for specially prepared thin samples that hardly convey the 3D arrangement of samples at the micrometer or larger level. CLSM enables to obtain high resolution optical images with depth selectivity. It has

gained popularity for 3D slides of fluorescent-stained tissue or biomaterial samples in various tissue engineering applications [118, 146, 147]. However, the penetration depth of CLSM is limited to about 300 μm. Progress in tissue engineering requires more detailed information on tissue physiology and the dynamics of scaffold structure (e.g., integration/degradation); thus, innovative imaging techniques are needed, including advancements from 2D to 3D image analysis and quantification, from label techniques to label-free techniques, and from invasive/destructive methods to non-invasive, non-destructive, and real-time methods [125].

X-ray micro-tomography (μCT) techniques, which are non-destructive and non-invasive, are becoming increasingly important for 3D visualization of scaffolds and engineered tissues in recent years. μCT can produce 3D image information to reveal the microstructure of scaffolds and regenerative tissues with specimen sizes from a few millimeters to 100 μm in size and provide nominal resolutions from 5 to 100 μm [119]. Quantitative architectural parameters of scaffolds, such as porosity, pore size, and pore wall thicknesses, can be extracted from μCT tomographic images [178, 290]. The new tissue growth and neovascularisation in scaffolds can also be visualized through 3D models reconstructed from the μCT data [291, 292]. Furthermore, the non-invasive aspects allow this technique to be used to monitor new tissue regrowth *in vivo* in a time-lapsed fashion [181]. Although μCT techniques have been widely applied in bone tissue engineering, there have been few applications of μCT to soft tissue (e.g., nerve, vascular, and liver) engineering. The main obstacle is the low x-ray attenuation contrast of low density scaffolds and soft tissues. Another

issue is the high ionizing radiation dose absorbed by engineered tissue samples during μCT imaging which has potential effects on cellular activity during the repair process [293, 294].

X-ray phase contrast imaging techniques differ from conventional attenuation contrast based x-ray imaging techniques because they instead rely on the refraction properties of object structure; they thus promise better contrast at lower doses [295]. Coupling synchrotron radiation (SR) based x-ray sources to phase contrast imaging techniques offers advantages such as better image quality, high photon flux, the possibility for monochromatization with a brilliance several orders of magnitude higher than those of a standard x-ray source, high spatial resolution (< 1 μm), and a better signal-to-noise ratio [120, 170]. In-line phase contrast imaging (in-line PCI) based on interference is one of the x-ray phase contrast imaging techniques [296] that has been successfully applied in the visualization studies in soft tissue engineering, including imaging of articular cartilage [202], sciatic nerves [201], and microvascular networks in bioceramic scaffolds [297]. In-line PCI is restricted to either thin objects or high x-ray imaging energies [298]. Diffraction enhanced imaging (DEI), another important x-ray phase contrast imaging technique, does not depend on interferometric techniques and works well with thick samples. Due to the use of a crystal analyzer with high angular resolution, DEI is sensitive to the boundary between tissues and/or biomaterials with different refractive indices [204, 212, 299]. It is possible to obtain scatter-free absorption contrast images or refraction images rather than a mixture of the two. DEI has been used in visualization of soft tissues, for example, in the

characterization of breast cancer [121, 300] and cochlea [301]. To date, little work has been reported in tissue engineering to take the aforementioned advantages of DEI to the visualization of soft engineered scaffolds and tissues.

This paper presents a study on the use of X-ray DEI to visualize low-density scaffolds in soft tissue engineering. Specifically, poly (L-lactide)/chitosan scaffolds embedded in rat muscle tissue were imaged using radiography, in-line PCI, and DEI techniques, respectively. The comparisons of image contrasts and other features based on these x-ray imaging techniques were carried out. All comparisons were based on images acquired of identical scaffold samples. To the best of our knowledge, this is the first report on the visualization of engineered scaffolds using a DEI technique.

6.2 Materials and Methods

Poly(L-lactide) (PLLA, mw: 10^5, product No.: B6002-2) was purchased from DURECT Corporation (United States). Chitosan (28191), Span 80, and glutaraldehyde were purchased from Sigma-Aldrich Canada. Acetic acid was diluted at 2% (wt/vol) concentration in distilled water as the stock solution.

6.2.1 PLLA/chitosan scaffold fabrication

(1) Chitosan microspheres

Chitosan microspheres (CM) were prepared using an emulsion-ionic crosslinking method. Briefly, chitosan (200 mg) was dissolved in 2% (wt/vol) acetic acid solution (10 mL). Liquid paraffin (50 mL) containing 1% (vol/vol) Span 80 emulsifier was

used as an oil phase. The water phase was dispersed into the oil phase using a magnetic stirrer (1000 prm) for 30 min to form a water-in-oil (W/O) emulsion. Next, glutaraldehyde as a crosslinking agent was slowly dropped into the W/O emulsion to solidify the chitosan droplets. The crosslinking reaction was allowed to proceed for 2 hours. Once separated by means of centrifugation, the chitosan microspheres were washed two times with isopropyl alcohol, two times with ethanol, four times with distilled water under centrifugation of 3000 rpm, and eventually lyophilized.

(2) Grid pattern PLLA/chitosan scaffolds

Tissue engineered scaffolds were fabricated using a dispensing-based fabrication system [262]. Briefly, 20% (wt/vol) PLLA was dissolved into chloroform and then mixed with 40% (wt/vol) chitosan microspheres. After the chitosan microspheres were uniformly mixed into PLLA solution, the mixture obtained was then loaded into the dispenser for scaffold fabrication. Under pressurized air, the mixture was extruded onto a glass substrate layer by layer, forming scaffolds with a 3D grid-pattern structure. The scaffolds became solid once the chloroform volatilized.

6.2.2 Sample preparation

(1) Tissue sample preparation

A Sprague Dawley rat was deeply anesthetized and perfused transcardially with 0.1M phosphate buffered saline (PBS), pH 7.4, followed by 4% paraformaldehyde in 0.1M PBS. Muscle tissues were then removed from the rat for x-ray imaging and

histological experiments. Animals were cared for according to the protocols of the Committee on Animal Care of the University of Saskatchewan (Animal Use Protocol #20080046).

(2) Scaffold sample preparation for x-ray imaging

PLLA/chitosan scaffolds were trimmed to a thickness of 0.5 mm. One of the scaffolds was selected and then sequentially put into different media for imaging. Specifically, the scaffold was 1) placed in air hereafter referred to as "A-scaffold", and directly exposed in x-rays for imaging; 2) embedded into rat muscle tissue with a total thickness of both scaffold and tissues of 5 mm ("M-scaffold"); then 3) removed from the rat tissue and immersed into water in containers with different inner thickness for imaging ("W-scaffold"), and the inner thickness of containers was 1, 4, and 5 cm, respectively.

6.2.3 Laboratory x-ray imaging

The laboratory x-ray images of the samples were captured using a SkyScan 1172 system (Skyscan, Kontich, Belgium) with an image pixel size of 3.5 μm. The x-ray source was set at an energy of 60 kVp. To enable comparison with the synchrotron x-ray images, experiments were performed only in projection mode with a single magnified image of the sample at the x-ray energy recorded.

6.2.4 Synchrotron radiation based (SR) x-ray imaging

SR x-ray imaging experiments were carried out on the BioMedical Imaging and Therapy (BMIT) beamline at the Canadian Light Source (CLS), Saskatoon, Canada.

(1) SR-radiography and in-line phase contrast imaging (in-line PCI)

Figure 6.1 is a schematic of the SR-radiography and in-line PCI setups. The samples were exposed to the synchrotron generated x-rays at different stage positions (Sample to Detector distance (SD)) to obtain absorption contrast (SD=2 cm) and phase contrast (SD=72 cm) projection images. Three different x-ray photon energy energies (15, 20, and 25 KeV) were applied in the imaging processes.

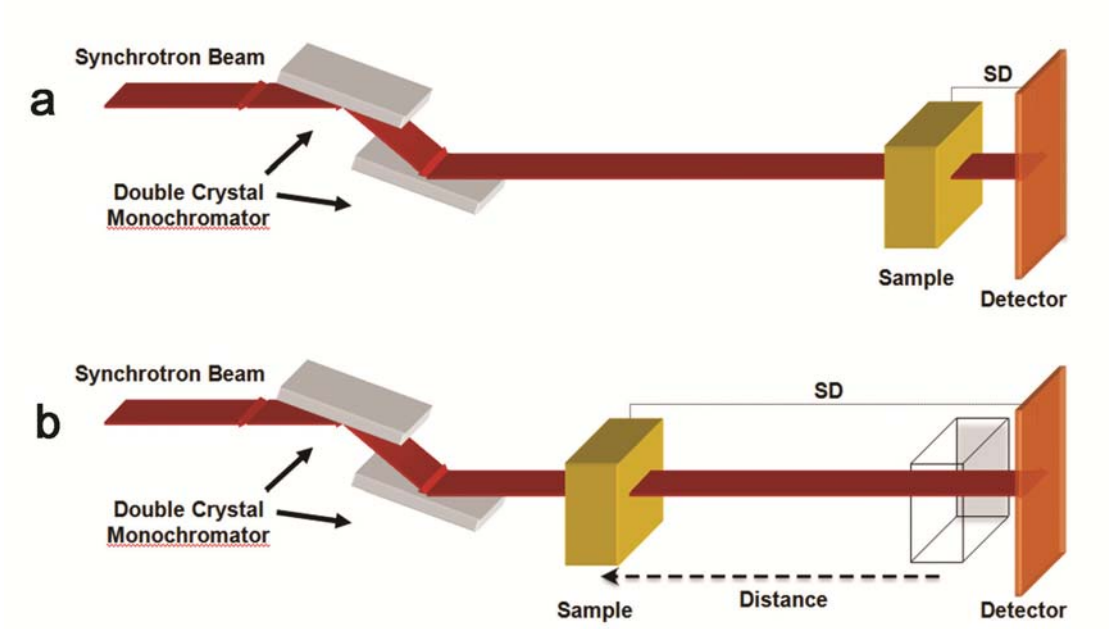

Figure 6.1. Systems for synchrotron radiation based (SR) (a) radiography and (b) in-line phase contrast imaging (in-line PCI). The difference between setups (a) and (b) is the Sample to Detector distance (SD), which influences the attenuation of absorption contrast or phase contrast. The SD was set at 2 cm (SR-radiography) and 72 cm (in-line PCI) in (a) and (b), respectively.

(2) Diffraction enhanced imaging (DEI)

Figure 6.2 is a schematic of the DEI setup. The white synchrotron beam was

monochromatized by a Si (220) double-crystal monochromator. The crystal analyzer was arranged behind the samples and installed on an axis that can rotate in order to be tuned to any position of its rocking curve. The DEI images were recorded by means of a beam monitor AA-40 (HAMAMATSU, Japan) coupled to a charge-coupled device (CCD) camera (HAMAMATSU C9300, 4000×2672 pixels) with an effective pixel size of approximately 4 μm. The measured resolution of this configuration of the DEI system exceeds 18 μm (20% contrast using a 28 line pair per mm resolution test phantom). The x-ray photon energy was set at 20 KeV.

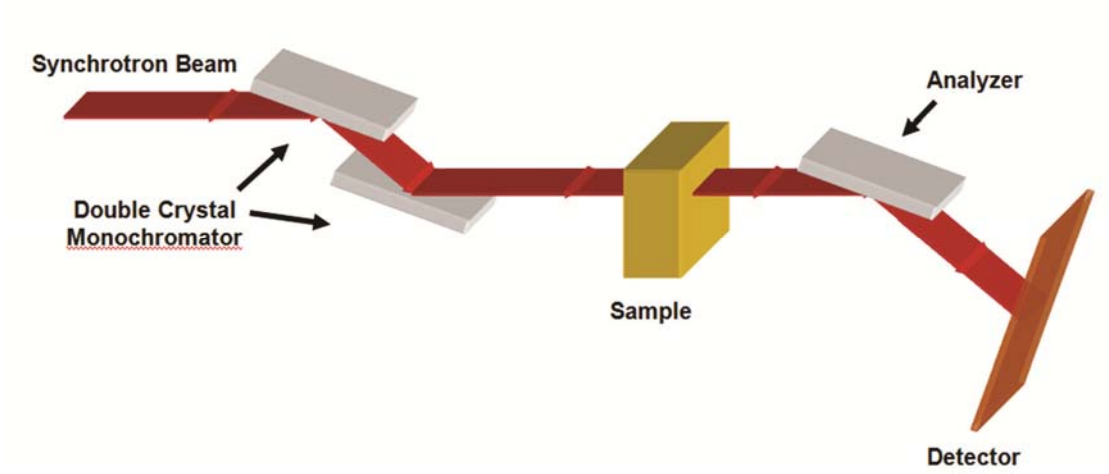

Figure 6.2. Synchrotron radiation based (SR) diffraction enhanced imaging (DEI) setup.

For each sample, three projection images were acquired: one at the peak of the rocking curve and one on each side of the rocking curve at the half maximum point. The image captured at the low angle side of the analyzer crystal is referred to as the low angle image (L), and the image captured at the high angle side of the analyzer crystal is referred to as the high angle image (H). At each position, three images (a sample image, a flat image, and a dark image) were captured for image normalization.

All DEI images obtained were then processed using MATLAB 7.7 software (Mathworks, Inc.) to form the refraction angle images using the following equation (6.1) [204].

$$\Delta\theta_Z = \frac{I_H R(\theta_L) - I_L R(\theta_H)}{I_L \left(\frac{\mathrm{d}R}{\mathrm{d}\theta}\right)(\theta_H) - I_H \left(\frac{\mathrm{d}R}{\mathrm{d}\theta}\right)(\theta_L)} \tag{6.1}$$

where $\triangle\theta_Z$ is the refraction contrast in the plane of diffraction; θ_H and θ_L are symmetrical angles on both sides of the rocking curve; I_{H} and I_{L} are the intensities in the analyzer at θ_H and θ_L, respectively; $R(\theta)$ is the rocking curve of the analyzer; and $(dR/d\theta)(\theta_H)$ and $(dR/d\theta)(\theta_L)$ are the slopes of the rocking curves at θ_H and θ_L, respectively. For images obtained at the 50% reflectivity points, $R(\theta_L)=R(\theta_H)$ and $dR/d\theta\ (\theta_H)=-dR/d\theta\ (\theta_L)$.

6.2.5 Histology and SEM

For histological assessment, scaffolds were embedded in 15×10 mm slices of rat muscle tissue that were postfixed using 4% paraformaldehyde in 0.1M PBS overnight and then cryoprotected overnight in 20% sucrose at 4 °C. The muscle tissues were flash frozen using an acetone and dry ice slurry. The tissues were sectioned on a cryostat (Micron, Zeiss, Canada) to 6 µm and stained using a standard Heamotoxylin & Eosin protocol (HE).

The morphology of the scaffolds was investigated by SEM (EVO60, Zeiss) with an accelerator voltage of 20 kV, in which samples were coated with gold using a Denton Vacuum Desk IV coater.

6.3 Results

6.3.1 PLLA/chitosan scaffolds

The PLLA/chitosan scaffolds were fabricated by using dispensing rapid prototyping method. Images of the scaffold were taken by using a camera and SEM are shown in Figure 6.3. The SEM image shows morphological features of the scaffold, where the rough surface of the strands in the scaffold is due to the presence of chitosan microspheres (with a concentration of 66.7%). The scaffold shown in Figure 6.3 (a) was used in all x-ray imaging experiments to eliminate potential sample variability (e.g., scaffold density) in the comparison of different x-ray imaging techniques.

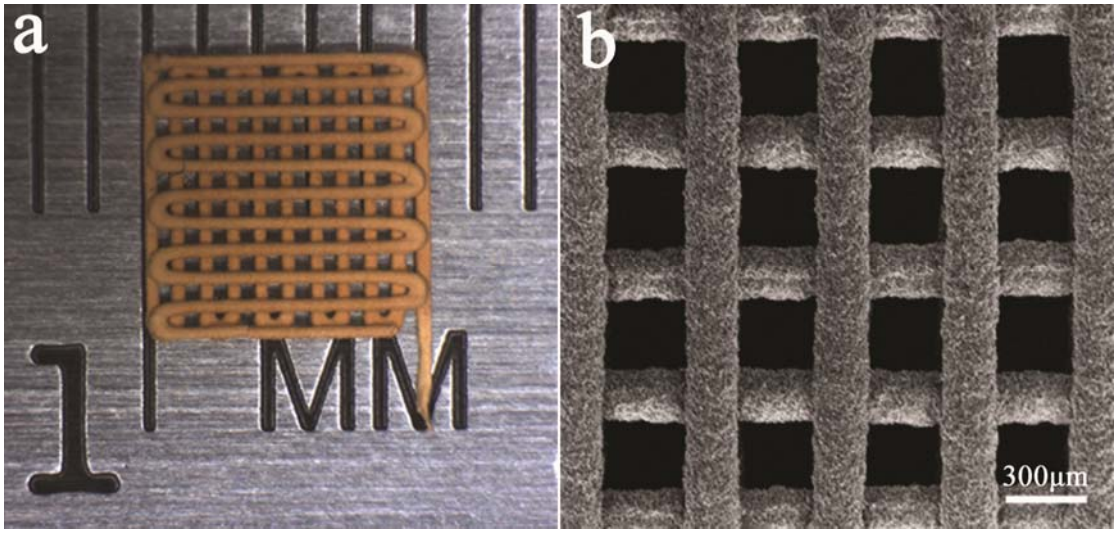

Figure 6.3. Images of the PLLA/chitosan scaffold from (a) a camera and (b) SEM.

6.3.2 Imaging the scaffold in air

The scaffold in air or A-scaffold was visualized using laboratory-based radiography, and SR-radiography, in-line PCI, and DEI techniques (Figure 6.4). The profile of the scaffold was visualized using both laboratory-based (Figure 6.4 (a)) and SR-radiography (Figure 6.4 (b)) but with poor image details. The principle of these

radiography techniques is based on the absorption contrast of imaged objects. As such, the low density of the scaffold results in inadequate image contrast. In the DEI imaging process, the refraction image (Figure 6.4 (d)), which was obtained from both the low and high angle images, shows the profile of the scaffold more clearly than the radiographs (Figure 6.4 (a and b)) and the in-line PCI image (Figure 6.4 (c)), especially, at the edges of the scaffold strands. The refraction contrast image represents the spatial gradient of the refractive index (horizontal in Figure 6.4 (d)), enhancing and highlighting edge appearance, contour interfaces of polymers, and environments. Furthermore, the refraction image reveals detailed information about the chitosan microspheres mixed in the strands of the scaffold, which also caused the scatter rejected by the analyzer.

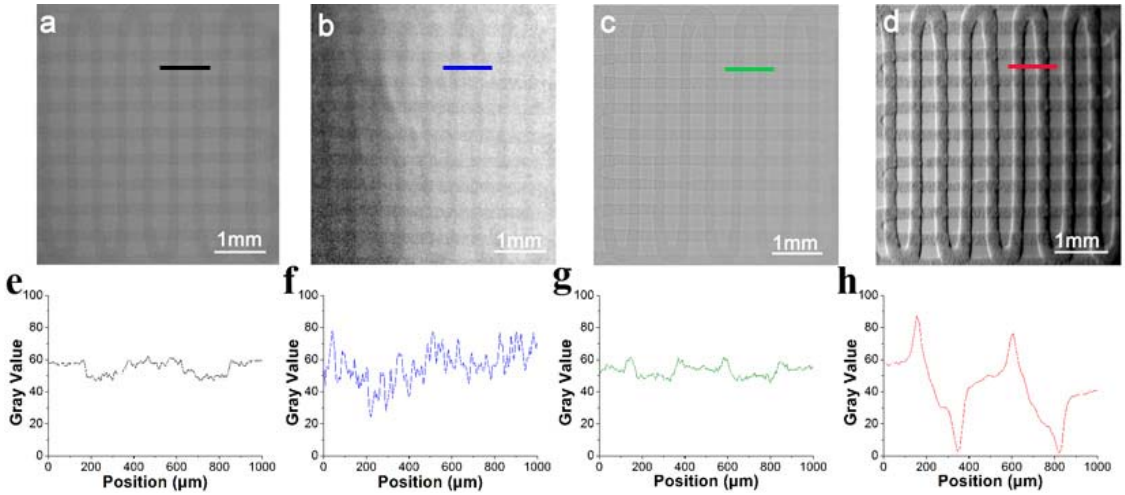

Figure 6.4. Comparison of the PLLA/chitosan scaffold images with laboratory-based radiography, synchrotron radiation based (SR-) radiography, in-line PCI, and DEI using the same sample at a similar magnification. (a) Laboratory -based radiograph at 60 Kvp, (b) SR radiograph at 20 KeV, (c) in-line PCI image at 20 KeV, and (d) DEI image at 20 KeV. (e), (f), (g), and (h) are the gray values corresponding to the color lines shown in images (a), (b), (c), and (d), respectively.

Figure 6.4 (e), (f), (g), and (h) show the gray value changes at the same location of the scaffold in the laboratory- and SR- radiographs, in-line PCI image, and DEI refraction image, respectively. The grayscale contrast in the refraction image is a factor of two higher than in the radiographs and in-line PCI image. Both radiography and in-line PCI are affected by x-ray scatter, while DEI can reject x-ray scatter and produce a pure refraction image. Compared to in-line PCI, DEI is able to show stronger contrast in images and has a higher sensitivity to object edges. Notably, DEI is sensitive to gradients in the projected density along a single direction. This effect accounts for the weaker contrast variations from the horizontal strands as compared to those from vertical ones in Figure 6.4(d). However, the tissue scaffolds are 3D arrays of strands so that no matter the orientation of the scaffold, there will be refraction contrast. The scaffold material also has scatter contrast (sometimes called extinction contrast). The contrast accounts for the other modalities. This type of contrast is isotropic and does not depend on the orientation of the strands. During image processing, most analyses for qualitative and quantitative detail, such as scaffold porosity, pore size, surface area to volume ratio, and interconnectivity, are based on image grayscale contrast. As such, appropriate grayscale contrast makes image analysis more accurate.

6.3.3 Imaging the scaffold in muscle tissue

After being embedded in the muscle tissue, the sample or M-scaffold was imaged using laboratory based radiography, in-line PCI, and DEI, respectively (Figure 6.5).

Using conventional laboratory based radiography at 60 Kvp, the scaffold tissue is not visible and the profile of the muscle tissue is unclear (Figure 6.5 (a)). The contrast of the radiograph is based on x-ray attenuation; however, because the attenuation of muscle tissue and the polymer scaffold are close due to their similar densities, distinguishing them using radiography techniques is difficult. Using in-line PCI at 20 KeV, the profile of the muscle tissue can be distinguished and the scaffold is faintly visible (Figure 6.5 (b)). However, the DEI image clearly shows the M-scaffold and has high contrast (Figure 6.5 (c)). The contrast of DEI images is based on the refraction and scattering properties of the object. Furthermore, many spots along the scaffold strands can be identified in the DEI image (Figure 6.5 (c)) due to the presence of the chitosan microspheres, consistent with the A-scaffold DEI image (Figure 6.4 (d)). The chitosan microspheres within the strands cause x-ray refraction that is captured by the detector throughout the analyzer. Although the scaffold was embedded into muscle tissues, the DEI image of the M-scaffold provides the most detailed image information of the A-scaffold DEI image (Figure 6.4 (d)).

Figure 6.5. X-ray images of the PLLA/chitosan scaffold embedded in rat muscle tissue (M-scaffold): (a) laboratory based radiograph at 60 Kvp, (b) in-line PCI image at 20 KeV, and (c) DEI image at 20 KeV. Arrows in (a), (b), and (c) indicate the location of the scaffold in the muscle tissue.

The DEI images of the M-scaffold provide detailed information on the scaffold structure as well as the profile of the muscle tissue. In Figure 6.5 (c), many short lines can be observed in the muscle tissue area. To identify these features, a histological analysis was conducted on the same muscle tissue after the x-ray imaging was conducted and the scaffold was removed. Figure 6.6 (a) shows a typical image of the muscle tissue at the same location as the DEI image. The light microscopy image shows the muscle tissues are separated into many small pieces by some white edges (Figure 6.6 (a) arrow) that have a similar distribution to the short lines in the DEI image (Figure 6.5 (c)). By magnifying the edge area in the muscle tissue, the histological image (Figure 6.6 (b)) indicates that the connective tissues pack the muscle cells into bundles of muscle fibers, with boundary interfaces formed between them. The presence of this detail indicates that the DEI technique is sensitive to refraction differences inside the soft tissues and is thus able to provide structural information about the soft tissues, particularly "edges" inside the tissue microstructure. The comparison of the DEI image to the histological analysis suggests that the structure discrepancy in soft tissues can be reflected in DEI images.

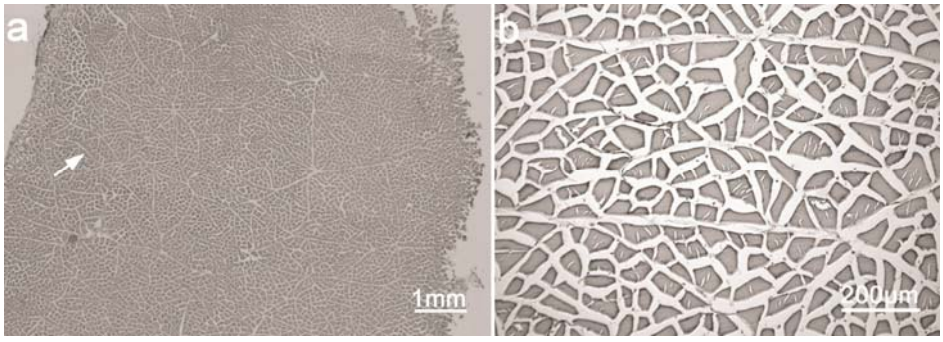

Figure 6.6. Light microscopy images: (a) a typical stained histological slices of the same muscle tissue used to embed the PLLA/chitosan scaffold and (b) magnified light microscopy image of the muscle tissue. (The arrow in image (a) points to the typical microstructure in the muscle tissue, which is magnified in image (b).)

6.3.4 Effect of sample thickness for DEI

To investigate the effect of soft tissue thickness on the visualization of low density scaffolds, the PLLA/chitosan scaffold was immersed into water (W-scaffold) and imaged using DEI at a photon energy of 20 KeV. Water was used as a substitute for soft tissue in this investigation; imaging results for scaffolds in water are comparable to scaffolds in soft tissue and water has a similar density and x-ray mass attenuation coefficient as soft tissue. The results illustrated that the scaffold is clearly distinguishable in the DEI refraction images at sample thicknesses of 1 and 4 cm (Figure 6.7 (a) and (b)) but not 5 cm (not shown). Figures 6.7 (c) and (d) show the gray value changes at the same location of the scaffold marked in Figure 6.7s (a) and (b), respectively. The grayscale contrast in both DEI images is similar, with the grayscale contrast of the 4 cm thick W-scaffold not significantly less than the 1 cm thick W-scaffold. These results suggest the DEI system at 20 KeV is capable of distinguishing the PLLA/chitosan scaffold in soft tissues with thickness up to approximately 4 cm.

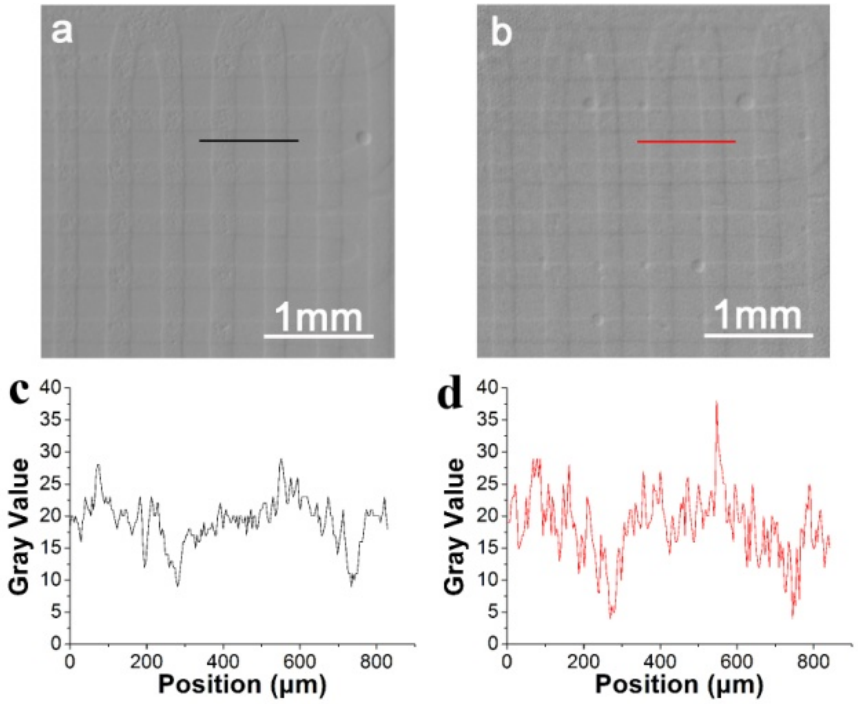

Figure 6.7. DEI images of the PLLA/chitosan scaffold in water (W-scaffold) at a photon energy of 20 KeV and total sample thicknesses of (a) 1 cm and (b) 4 cm. (c) and (d) are the gray value changes corresponding to the locations marked in images (a) and (b), respectively.

6.3.5 Radiation dose and radiograph quality

The surface absorbed dose rates experienced by the scaffolds at different average photon energies during x-ray imaging were evaluated according to the following equation [302]:

$$\dot{D}(E_{ph}) = \frac{\dot{N}_0 E_{ph}}{A}\left(\frac{\mu}{\rho}\Big|_{enabs}\right) \tag{6.2}$$

where $\dot{D}(E_{ph})$ is the surface absorbed dose rate to the sample; $\dot{N}_0$ is the photon fluence rate, measured using a gas ionization chamber; E_{ph} is the average photon energy; $\frac{\mu}{\rho}\Big|_{enabs}$ is the mass energy absorption coefficient of the sample; and A is the sample area.

As the x-ray photon energies increase, the dose rates of the sample decreased

(Table 1); for example, photon energy increase of ~60% (from 15 to 25 KeV) results in a dose rate reduced of ~60% (from2.16 to 0.86 mGy/s).

The image contrast of the A-scaffold in the SR-radiographs at different photon energies is shown in Figure 6.8 (d-f). The images become blurry (Figure 6.8 (a-c)) and image contrast substantially declines as the photon energy is increased; for example, the scaffold in Figure 6.8 (a) is clearly visible at a photon energy of 15 KeV but is barely visible at a photon energy of 25 KeV. The results indicate that better x-ray attenuation contrast of samples can be obtained using radiography at lower photon energies but the sample is consequently exposed to higher dose rates.

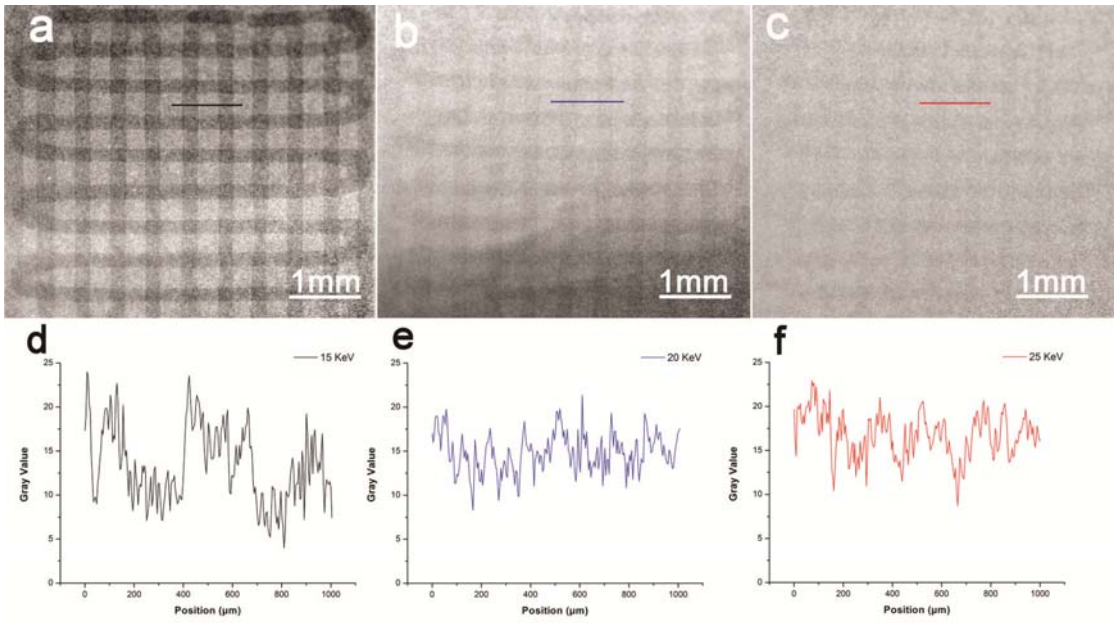

Figure 6.8. SR-radiographs and corresponding image contrast of the A-scaffold at different photon energies with the sample to detector distance (SD) of 2 cm: (a) at 15 KeV, (b) at 20 KeV, and (c) at 25 KeV; (d), (e), and (f) are the gray value changes corresponding to the color lines shown in images a, b, and c, respectively. All image contrasts were measured at the same location of the scaffold.

6.4 Discussion

The present study illustrates, for the first time, the possibilities of DEI for the

visualization of low density tissue scaffolds. Specifically, the PLLA/chitosan scaffold was visualized in both air environment and muscle tissue using different x-ray imaging techniques including laboratory- and SR- radiography, in-line PCI, and DEI. For comparison, all the images were captured from the same scaffold sample. The DEI technique can visualize low density scaffolds in muscle tissue better than any of the other techniques considered here. Moreover, DEI has the potential to be fully non-invasive and non-destructive for both *in vitro* and *in vivo* applications in soft tissue engineering research. This would allow low density scaffolds to remain intact for additional assessments as well as facilitate the monitoring of either degradation behaviour or new tissue ingrowth after implantation, which is especially relevant for pre-clinical trial applications. Inspired by the promising results from the present study and the fact that the integration of DEI and computed tomography techniques (i.e., DEI-CT) can provide 3D visualization of tissue samples, such as breast tissue [211], the DEI-CT can be applied to realize the 3D visualization of engineered scaffolds and newly-generated tissues *in vivo*.

Scatter is a problem in conventional x-ray imaging where it is common for over half of the x-rays that reach the detector to be of scatter origin. Thus, anti-scatter grids are used to reject some of this scatter which improves image contrast. In DEI technique, however, the use of an analyzer can reject off-angle and off-energy scattered x-rays primarily from Compton scattering. As such, this technique is almost scatter free [204]. This effect of extreme scatter rejection has two key advantages. First, this effect can be used to enhance the contrast from small structural features,

such as lung alveoli, fur, and etc., from rejection of ultra-small x-ray scattering [212]. Second, another important effect is that the increased scatter from thick objects becomes almost completely irrelevant, which allows them to be imaged at no loss of contrast due to scatter (see Figure 7). This is part of the reason why DEI is so successful at imaging large thick objects at higher x-ray energies [303]. In this study, the ability to image the PLLA/chitosan scaffold in soft tissue using DEI at 20 KeV was limited to sample thicknesses up to approximately 4 cm; the reason is that a log-linear relationship between the transmitted photon flux and the sample thickness prevented further penetration [304]. Higher x-ray energy DEI systems with higher photon fluxes can visualize thicker tissue samples; for example, breast tissue samples with thickness of 12 cm have been clearly visualized at 60 KeV [305].

Degradation of resolution due to the DEI system was not observed in this work. The resolution of the DEI system is determined by source size, the pixel size of the detector, and the distances between the source, object, and detector; also, there will be a small (approximately 1 μm) contribution in the diffraction plane due to beam penetration into the analyzer crystal. The current resolution could meet the requirements of the tissue level and scaffold degradation studies *in situ* and possibly *in vivo*. Considering the potential variety of samples and wide range of sizes relevant for soft tissue engineering applications, higher resolution imaging systems might be helpful for smaller fields of view while low resolution systems with a large field of view may be more useful for *in vivo* applications.

During x-ray imaging, the dose absorbed by the sample is lower at higher photon

energy levels. Photoelectric absorption in the sample contributes to the main part of the total attenuation at low photon energy levels (and a high dose received by the sample), while Compton scatter in the sample plays the leading role in the processes at high photon energy levels [306]. In conventional radiography, absorption contrast is directly related to the dose received by the sample. Better image contrast means more absorbed x-rays and more dose to the sample at lower photon energy levels [212]. In tissue engineering applications, high dose x-ray imaging processes will change the material properties of the imaged scaffolds and the biological properties of the imaged tissues. The harmful effects of ionizing radiation present in conventional x-ray imaging are a notable challenge to applying these techniques to tissue engineering, especially for *in vivo* visualization [294]. In DEI, the sample absorbs the same dose as conventional radiography at the same x-ray energy, but additional image contrast is generated from x-ray refraction. Thus, compared with radiographs at the same energy level, DEI images of scaffolds embedded in muscle tissue demonstrate higher contrast. Furthermore, DEI can be optimally applied at higher x-ray energies and lower doses in visualization applications [204]. When 2D x-ray imaging techniques are extended to 3D applications, the combination of DEI and tomography techniques will cause order-of-magnitude reductions in radiation dose and offers great promise for the visualization and characterization of scaffolds and regenerative tissues in living animals.

6.5 Conclusions

Visualization of low density materials using conventional radiography is a challenging task due to weak x-ray attenuation. Rising to this challenge, the low density PLLA/chitosan scaffolds were visualized by DEI and compared our results to conventional radiography and in-line PCI. When visualized in air, the DEI images of the scaffolds were much clearer compared to radiographs and in-line PCI images. DEI was also demonstrated to have the capacity to provide enhanced image contrast that could reveal detailed morphology of low density scaffolds. After embedding the scaffold into rat muscle tissue, the images obtained shows DEI can provide higher quality visualization of scaffolds as compared to both radiography and in-line PCI. The DEI images not only show the structure of the scaffold but also the microstructural features of the muscle tissue. In addition, the DEI technique accomplishes good imaging performance with low radiation doses at high energy levels. Overall, DEI technique has great potential for visualization applications in soft tissue engineering, in particular the real-time observation of engineered tissues in living animals.

CHAPTER 7
CONCLUSIONS AND RECOMMENDATIONS

7.1 Conclusions

The aim of this research is to develop and characterize 3D biodegradable scaffolds for potential peripheral nerve tissue regeneration. The main conclusions of this research are summarized as follows:

(1) The orientation of axon growth in scaffolds can be achieved in an artificially patterned substrate by creating selective high-affinity pathways in scaffolds. The 2D micropatterns were designed to impart directionality to the growth of neurites, which take advantage of the DBRP technique. *In vitro* experimental results demonstrated DRG neurites on these patterns preferentially grew upon and followed the laminin-blended chitosan pathways compared to the pure chitosan pathways.

(2) Compared to the DBRP technique, RFP is able to achieve an improved porous structure of scaffolds which includes higher porosity, enhanced pore size distribution and thinner wall thickness. The improved porous structure would facilitate cell and tissue migration and vascularization.

(3) The combination of CMs and PLLA can effectively control the release of bioactive molecules from the scaffolds and control the mechanical properties of the scaffolds. The experimental results of the BSA release demonstrate that the use of the CMs is an effective way to administrate the BSA release and that its rate can be controlled by adjusting the crosslinking degree of the CMs. Thus the BSA release period can be prolonged after the CMs are embedded into the PLLA scaffolds. The

experimental results also show that the addition of the CMs to the PLLA scaffolds can improve the mechanical properties of the scaffolds which also depend on the cryogenic temperature used in the scaffold fabrication process.

(4) The biodegradation behavior of PLLA can be regulated and adjusted by adding CMs. The results obtained from *in vitro* degradation experiments of PLLA/CMs scaffolds showed that there was a decrease in the degradation rate of the composite scaffolds in phosphate-buffer solution with pH 7.4 at 37°C after 8 weeks compared with pure PLLA scaffolds. The addition of CMs into PLLA slowed the hydrolysis of PLLA after 4 weeks degradation and also resulted in the decrease of PLLA crystallinity during scaffold fabrication.

(5) The μCT technique employed in scaffold degradation studies is capable of monitoring microstructural changes of scaffolds. This new application allows a deeper insight towards understanding scaffold degradation behavior and possible visualization of new tissue growth as well.

(6) The DEI technique has a great potential for *in vivo* visualization applications in nerve tissue engineering. In order to explore the visualization of low density polymer scaffolds *in vivo*, the PLLA/chitosan scaffolds were imaged by DEI and compared to the results obtained from conventional radiography and in-line PCI. After embedding the scaffold into rat muscle tissue, the images obtained demonstrate DEI can provide higher quality images of scaffolds as compared to both radiography and in-line PCI which not only show the structure of the scaffolds but also the microstructural features of the muscle tissue. In addition, the DEI technique accomplishes good imaging performance with low radiation doses at high x-ray imaging energy levels.

7.2 Recommendations for future work

Based upon the work presented in this dissertation, a number of projects are recommended for future research.

(1) The 2D micropattern model has been successfully created to guide the directional growth of axons *in vitro*. Based on this 2D design, a 3D PLLA/CMs scaffold with bioactive molecules, such as laminin, could be developed by means of the DBRP technique for the studies of axon guidance *in vitro*. Bioactive molecule-loaded CMs will only be located in the inner layers of the nerve conduits along the longitudinal direction to promote directional axon growth. Additionally, using 3D pattern scaffolds, the scaffolds will provide not only biochemical cues but also geometric cues for neurite directional growth [111].

(2) One of the future investigations could be aimed to develop the ability of the nerve conduit scaffolds so as to manipulate cellular and tissue growth in the presence of multiple biochemical cues and more complex structured micro-environments. Based on the design of PLLA/CMs scaffolds, the CMs loaded with different neurotrophins, such as NGF or BDNF, could be embedded into the PLLA strands with a designed ratio of NGF-loaded CMs to BDNF-loaded CMs. The multiple neurotrophins encapsulated scaffolds may better support and promote axon outgrowth.

(3) Neurotrophin gradients in the scaffolds may enable another means to control guiding axon outgrowth. A dynamic mixing method may be developed to create neurotrophin-loaded strands with concentration gradients by means of DBRP. Briefly,

a strategy for gradient generation is to use two dispensers loaded with non- and neurotrophin-loaded CMs to pump different solutions at controllable flow rates into a mixer and to extrude the mixed solution with designed neurotrophin concentration to the substrate.

(4) Synchrotron based DEI, as a non-invasive and non-destructive imaging technique, has been successfully applied in the visualization of low density polymer scaffolds and soft tissues. Coupling with the computed tomography technique, DEI-CT can obtain 3D imaging information of the scaffolds and new tissue. During *in vivo* experiments of the nerve conduit scaffolds, 3D images of the *in vivo* samples could be reconstructed based on a series of DEI projection images. DEI-CT can provide quantitative results based on different gray levels in reconstructed images of the axon outgrowth and scaffold degradation. It also shows a great potential for the real-time observation of engineered tissues in living animals due to the low radiation dose accumulated during the imaging processes.

LIST OF REFERENCES

[1] Noble J, Munro C A, Prasad V, Midha R 1998 Analysis of upper and lower extremity peripheral nerve injuries in a population of patients with multiple injuries *Journal of Trauma-Injury Infection and Critical Care* 45 116-122

[2] Koeppen A H 2004 Wallerian degeneration: history and clinical significance *Journal of the Neurological Sciences* 220 115-117

[3] Waitayawinyu T, Parisi D M, Miller B, Luria S, Morton H J, Chin S H, Trumble T E 2007 A comparison of polyglycolic acid versus type 1 collagen bioabsorbable nerve conduits in a rat model: An alternative to autografting *Journal of Hand Surgery-American Volume* 32A 1521-1529

[4] Huang E J, Reichardt L F 2001 Neurotrophins: Roles in neuronal development and function *Annual Review of Neuroscience* 24 677-736

[5] Kobsa S, Saltzman W M 2008 Bioengineering approaches to controlled protein delivery *Pediatric Research* 63 513-519

[6] Risitano G, Cavallaro G, Merrino T, Coppolino S, Ruggeri F 2002 Clinical results and thoughts on sensory nerve repair by autologous vein graft in emergency hand reconstruction *Chirurgie de la main* 21 194-197

[7] Chiu D T W, Janecka I, Krizek T J, Wolff M, Lovelace R E 1982 Autogenous vein graft as a conduit for nerve regeneration *Surgery* 91 226-233

[8] Meek M F, Varejao A S P, Geuna S 2004 Use of skeletal muscle tissue in peripheral nerve repair: Review of the literature *Tissue Engineering* 10

1027-1036

[9] Connolly S S, Yoo J J, Abouheba M, Soker S, McDougal W S, Atala A 2008 Cavernous nerve regeneration using acellular nerve grafts *World Journal of Urology* 26 333-339

[10] Hontanilla B, Yeste L, Auba C, Gorria O 2006 Neuronal quantification in cold-preserved nerve allografts and treatment with FK-506 through osmotic pumps compared to nerve autografts *J. Reconstr. Microsurg.* 22 363-373

[11] Bennet D, Kim S 2011 Implantable microdevice for peripheral nerve regeneration: materials and fabrications *Journal of Materials Science* 46 4723-4740

[12] Chen Y S, Hsieh C L, Tsai C C, Chen T H, Cheng W C, Hu C L, Yao C H 2000 Peripheral nerve regeneration using silicone rubber chambers filled with collagen, laminin and fibronectin *Biomaterials* 21 1541-1547

[13] Vasconcelos B C E, Gay-Escoda C 2000 Facial nerve repair with expanded polytetrafluoroethylene and collagen conduits: An experimental study in the rabbit *Journal of Oral and Maxillofacial Surgery* 58 1257-1262

[14] Shen Z L, Lassner F, Becker M, Walter G F, Bader A, Berger A 1999 Viability of cultured nerve grafts: An assessment of proliferation of Schwann cells and fibroblasts *Microsurgery* 19 356-363

[15] Heath C A, Rutkowski G E 1998 The development of bioartificial nerve grafts for peripheral-nerve regeneration *Trends in Biotechnology* 16 163-168

[16] Hutmacher D W 2001 Scaffold design and fabrication technologies for

engineering tissues - state of the art and future perspectives *Journal of Biomaterials Science-Polymer Edition* 12 107-124

[17] Liu C, Xia Z, Czernuszka J T 2007 Design and development of three-dimensional scaffolds for tissue engineering *Chemical Engineering Research & Design* 85 1051-1064

[18] Bellamkonda R V 2006 Peripheral nerve regeneration: An opinion on channels, scaffolds and anisotropy *Biomaterials* 27 3515-3518

[19] Hudson T W, Evans G R D, Schmidt C E 1999 Engineering strategies for peripheral nerve repair *Clinics in Plastic Surgery* 26 617

[20] Gupta A P, Kumar V 2007 New emerging trends in synthetic biodegradable polymers - Polylactide: A critique *European Polymer Journal* 43 4053-4074

[21] Maurus P B, Kaeding C C 2004 Bioabsorbable implant material review *Operative Techniques in Sports Medicine* 12 158-160

[22] Thordarson D B, Samuelson M, Shepherd L E, Merkle P F, Lee J 2001 Bioabsorbable versus stainless steel screw fixation of the syndesmosis in pronation-lateral rotation ankle fractures: A prospective randomized trial *Foot & Ankle International* 22 335-338

[23] Lumiaho J, Heino A, Tunninen V, Ala-Opas M, Talja M, Valimaa T, Tormala P 1999 New bioabsorbable polylactide ureteral stent in the treatment of ureteral lesions: An experimental study *Journal of Endourology* 13 107-112

[24] Charbit Y, Hitzig C, Bolla M, Bitton C, Bertrand M F 1999 Comparative study of physical properties of three suture materials: silk, e-PTFE (Gore-Tex), and

PLA/PGA (Vicryl) *Biomedical instrumentation & technology / Association for the Advancement of Medical Instrumentation* 33 71-75

[25] Evans G R D, Brandt K, Niederbichler A D, Chauvin P, Hermann S, Bogle M, Otta L, Wang B, Patrick C W 2000 Clinical long-term in vivo evaluation of poly(L-lactic acid) porous conduits for peripheral nerve regeneration *Journal of Biomaterials Science-Polymer Edition* 11 869-878

[26] Evans G R D, Brandt K, Widmer M S, Lu L, Meszlenyi R K, Gupta P K, Mikos A G, Hodges J, Williams J, Gurlek A, Nabawi A, Lohman R, Patrick C W 1999 In vivo evaluation of poly(L-lactic acid) porous conduits for peripheral nerve regeneration *Biomaterials* 20 1109-1115

[27] Li J, McNally H, Shi R 2008 Enhanced neurite alignment on micro-patterned poly-L-lactic acid films *Journal of Biomedical Materials Research Part A* 87A 392-404

[28] Khorasani M T, Mirzadeh H, Talebi A, Irani S, Daliri M 2009 Tubular scaffold design of poly(L-lactic acid) for nerve tissue engineering: Preparation, characterization, and in vitro assay *Iranian Polymer Journal* 18 297-306

[29] Leach M K, Feng Z-Q, Gertz C C, Tuck S J, Regan T M, Naim Y, Vincent A M, Corey J M 2011 The culture of primary motor and sensory neurons in defined media on electrospun poly-L-lactide nanofiber scaffolds *Journal of visualized experiments : JoVE*

[30] Koh H S, Yong T, Chan C K, Ramakrishna S 2008 Enhancement of neurite outgrowth using nano-structured scaffolds coupled with laminin *Biomaterials* 29

3574-3582

[31] McKeon-Fischer K D, Freeman J W 2011 Characterization of electrospun poly(L-lactide) and gold nanoparticle composite scaffolds for skeletal muscle tissue engineering *Journal of Tissue Engineering and Regenerative Medicine* 5 560-568

[32] Ratner B D, Hoffman A F, Schoen F J, Lemons J E (2004) Classes of materials used in medicine. In: Biomaterials Science Elsevier Academic Press, London, pp. 120-121

[33] He L, Zhang Y, Zeng C, Ngiam M, Liao S, Quan D, Zeng Y, Lu J, Ramakrishna S 2009 Manufacture of PLGA multiple-channel conduits with precise hierarchical pore architectures and in vitro/vivo evaluation for spinal cord injury *Tissue Engineering Part C-Methods* 15 243-255

[34] Yuan J-D, Nie W-B, Fu Q, Lian X-F, Hou T-S, Tan Z-Q 2009 Novel three-dimensional nerve tissue engineering scaffolds and its biocompatibility with Schwann cells *Chinese journal of traumatology = Zhonghua chuang shang za zhi / Chinese Medical Association* 12 133-137

[35] Piotrowicz A, Shoichet M S 2006 Nerve guidance channels as drug delivery vehicles *Biomaterials* 27 2018-2027

[36] Gunatillake P, Mayadunne R, Adhikari R 2006 Recent developments in biodegradable synthetic polymers *Biotechnology annual review* 12 301-347

[37] Pierucci A, De Duek E A R, De Oliveira A L R 2008 Peripheral nerve regeneration through biodegradable conduits prepared using solvent evaporation

Tissue Eng. Part A 14 595-606

[38] Chiono V, Vozzi G, D'Acunto M, Brinzi S, Domenici C, Vozzi F, Ahluwalia A, Barbani N, Giusti P, Ciardelli G 2009 Characterisation of blends between poly(epsilon-caprolactone) and polysaccharides for tissue engineering applications *Mater. Sci. Eng. C-Mater. Biol. Appl.* 29 2174-2187

[39] Ghasemi-Mobarakeh L, Prabhakaran M P, Morshed M, Nasr-Esfahani M-H, Ramakrishna S 2008 Electrospun poly(epsilon-caprolactone)/gelatin nanofibrous scaffolds for nerve tissue engineering *Biomaterials* 29 4532-4539

[40] Yu W, Zhao W, Zhu C, Zhang X, Ye D, Zhang W, Zhou Y, Jiang X, Zhang Z 2011 Sciatic nerve regeneration in rats by a promising electrospun collagen/poly(epsilon-caprolactone) nerve conduit with tailored degradation rate *Bmc Neuroscience* 12

[41] Ljungberg C, Johansson-Ruden G, Bostrom K J, Novikov L, Wiberg M 1999 Neuronal survival using a resorbable synthetic conduit as an alternative to primary nerve repair *Microsurgery* 19 259-264

[42] Chen G Q, Wu Q 2005 The application of polyhydroxyalkanoates as tissue engineering materials *Biomaterials* 26 6565-6578

[43] Khorasani M T, Mirmohammadi S A, Irani S 2011 Polyhydroxybutyrate (PHB) scaffolds as a model for nerve tissue engineering application: Fabrication and in vitro assay *International Journal of Polymeric Materials* 60 562-575

[44] Artsis M I, Bonartsev A P, Iordanskii A L, Bonartseva G A, Zaikov G E 2010 Biodegradation and medical application of microbial poly(3-hydroxybutyrate)

Molecular Crystals and Liquid Crystals 523 21-49

[45] Rinaudo M 2006 Chitin and chitosan: Properties and applications *Progress in Polymer Science* 31 603-632

[46] Chatelet C, Damour O, Domard A 2001 Influence of the degree of acetylation on some biological properties of chitosan films *Biomaterials* 22 261-268

[47] Chen R H, Hua H D 1996 Effect of N-acetylation on the acidic solution stability and thermal and mechanical properties of membranes prepared from different chain flexibility chitosans *Journal of Applied Polymer Science* 61 749-754

[48] Cao W L, Jing D H, Li J M, Gong Y D, Zhao N M, Zhang X F 2005 Effects of the degree of deacetylation on the physicochemical properties and Schwann cell affinity of chitosan films *Journal of Biomaterials Applications* 20 157-177

[49] Yomota C, Komuro T, Kimura T 1990 Studies on the degradation of chitosan films by lysozyme and release of loaded chemicals *Yakugaku Zasshi-Journal of the Pharmaceutical Society of Japan* 110 442-448

[50] Nakamura F, Onishi H, Machida Y, Nagai T 1992 Lysozyme-catalyzed degradation properties of the conjugates between chitosan having some deacetylation degrees and methotrexate *Yakuzaigaku* 52 59-67

[51] Onishi H, Machida Y 1999 Biodegradation and distribution of water-soluble chitosan in mice *Biomaterials* 20 175-182

[52] Bhattarai N, Gunn J, Zhang M 2010 Chitosan-based hydrogels for controlled, localized drug delivery *Advanced Drug Delivery Reviews* 62 83-99

[53] Muzzarelli R A A 2009 Chitins and chitosans for the repair of wounded skin,

nerve, cartilage and bone *Carbohydrate Polymers* 76 167-182

[54] Kim I-Y, Seo S-J, Moon H-S, Yoo M-K, Park I-Y, Kim B-C, Cho C-S 2008 Chitosan and its derivatives for tissue engineering applications *Biotechnology Advances* 26 1-21

[55] Katayama Y, Montenegro R, Freier T, Midha R, Belkas J S, Shoichet M S 2006 Coil-reinforced hydrogel tubes promote nerve regeneration equivalent to that of nerve autografts *Biomaterials* 27 505-518

[56] Zhang J R, Yi L K, Zhang J C 2010 Chitosan tube bridging autologous nerve segments for the repair of long-segmental sciatic nerve defects *Neural Regen. Res.* 5 668-672

[57] Lee J E, Kim S E, Kwon I C, Ahn H J, Cho H, Lee S H, Kim H J, Seong S C, Lee M C 2004 Effects of a chitosan scaffold containing TGF-beta 1 encapsulated chitosan microspheres on in vitro chondrocyte culture *Artificial Organs* 28 829-839

[58] Mittal S, Cohen A, Maysinger D 1994 In-vitro effects of brain-derived neurotrophic factor released from microspheres *Neuroreport* 5 2577-2582

[59] Yu L M Y, Miller F D, Shoichet M S 2010 The use of immobilized neurotrophins to support neuron survival and guide nerve fiber growth in compartmentalized chambers *Biomaterials* 31 6987-6999

[60] Rocha L B, Goissis G, Rossi M A 2002 Biocompatibility of anionic collagen matrix as scaffold for bone healing *Biomaterials* 23 449-456

[61] Archibald S J, Krarup C, Shefner J, Li S T, Madison R D 1991 A collagen-based

nerve guide conduit for peripheral-nerve repair - an electrophysiological study of nerve regeneration in rodents and nonhuman-primates *Journal of Comparative Neurology* 306 685-696

[62] Alluin O, Wittmann C, Marqueste T, Chabas J F, Garcia S, Lavaut M N, Guinard D, Feron F, Decherchi P 2009 Functional recovery after peripheral nerve injury and implantation of a collagen guide *Biomaterials* 30 363-373

[63] Yao L, de Ruiter G C W, Wang H, Knight A M, Spinner R J, Yaszemski M J, Windebank A J, Pandit A 2010 Controlling dispersion of axonal regeneration using a multichannel collagen nerve conduit *Biomaterials* 31 5789-5797

[64] Labrador R O, Buti M, Navarro X 1998 Influence of collagen and laminin gels concentration on nerve regeneration after resection and tube repair *Exp. Neurol.* 149 243-252

[65] Scott R, Marquardt L, Willits R K 2010 Characterization of poly(ethylene glycol) gels with added collagen for neural tissue engineering *Journal of Biomedical Materials Research Part A* 93A 817-823

[66] Nair L S, Laurencin C T 2007 Biodegradable polymers as biomaterials *Progress in Polymer Science* 32 762-798

[67] Hernandez R M, Orive G, Murua A, Pedraz J L 2010 Microcapsules and microcarriers for in situ cell delivery *Advanced Drug Delivery Reviews* 62 711-730

[68] Frampton J P, Hynd M R, Shuler M L, Shain W 2011 Fabrication and optimization of alginate hydrogel constructs for use in 3D neural cell culture

Biomedical materials 6 015002

[69] Mosahebi A, Wiberg M, Terenghi G 2003 Addition of fibronectin to alginate matrix improves peripheral nerve regeneration in tissue-engineered conduits *Tissue Engineering* 9 209-218

[70] Vollrath F, Barth P, Basedow A, Engstrom W, List H 2002 Local tolerance to spider silks and protein polymers in vivo *In Vivo* 16 229-234

[71] Yang Y, Ding F, Wu H, Hu W, Liu W, Liu H, Gu X 2007 Development and evaluation of silk fibroin-based nerve grafts used for peripheral nerve regeneration *Biomaterials* 28 5526-5535

[72] Yang Y M, Chen X M, Ding F, Zhang P Y, Liu J, Go X S 2007 Biocompatibility evaluation of silk fibroin with peripheral nerve tissues and cells in vitro *Biomaterials* 28 1643-1652

[73] Hsu S H, Su C H, Chiu I M 2009 A novel approach to align adult neural stem cells on micropatterned conduits for peripheral nerve regeneration: A feasibility study *Artificial Organs* 33 26-35

[74] Yang Y, De Laporte L, Rives C B, Jang J H, Lin W C, Shull K R, Shea L D 2005 Neurotrophin releasing single and multiple lumen nerve conduits *J. Control. Release* 104 433-446

[75] Khorasani M T, Mirmohammadi S A, Irani S Polyhydroxybutyrate (PHB) Scaffolds as a Model for Nerve Tissue Engineering Application: Fabrication and In Vitro Assay *International Journal of Polymeric Materials* 60 562-575

[76] Pego A P, Poot A A, Grijpma D W, Feijen J 2003 Biodegradable elastomeric

scaffolds for soft tissue engineering *J. Control. Release* 87 69-79

[77] Huang Y C, Huang Y Y, Huang C C, Liu H C 2005 Manufacture of porous polymer nerve conduits through a lyophilizing and wire-heating process *Journal of Biomedical Materials Research Part B-Applied Biomaterials* 74B 659-664

[78] Xie J, MacEwan M R, Schwartz A G, Xia Y 2010 Electrospun nanofibers for neural tissue engineering *Nanoscale* 2 35-44

[79] Mikos A G, Thorsen A J, Czerwonka L A, Bao Y, Langer R, Winslow D N, Vacanti J P 1994 Preparation and characterization of poly(L-lactic acid) foams *Polymer* 35 1068-1077

[80] Author 1996 Biocompatible polymer membranes and methods of preparation of three dimensional membrane structures United States 5514378

[81] Di Maio E, Mensitieri G, Iannace S, Nicolais L, Li W, Flumerfelt R W 2005 Structure optimization of polycaprolactone foams by using mixtures of CO2 and N-2 as blowing agents *Polymer Engineering and Science* 45 432-441

[82] Haugen H, Ried V, Brunner M, Will J, Wintermantel E 2004 Water as foaming agent for open cell polyurethane structures *Journal of Materials Science-Materials in Medicine* 15 343-346

[83] Parks K L, Beckman E J 1996 Generation of microcellular polyurethane foams via polymerization in carbon dioxide .2. Foam formation and characterization *Polymer Engineering and Science* 36 2417-2431

[84] Quirk R A, France R M, Shakesheff K M, Howdle S M 2004 Supercritical fluid technologies and tissue engineering scaffolds *Current Opinion in Solid State &*

Materials Science 8 313-321

[85] Lee K W D, Chan P K, Feng X S 2004 Morphology development and characterization of the phase-separated structure resulting from the thermal-induced phase separation phenomenon in polymer solutions under a temperature gradient *Chem. Eng. Sci.* 59 1491-1504

[86] Pikal M J, Shah S, Roy M L, Putman R 1990 The secondary drying stage of freeze-dring kinetics as a function of temperature and chamber pressure *International Journal of Pharmaceutics* 60 203-217

[87] Liapis A I, Bruttini R 1994 A theory for the primary and secondary drying stages of the freeze-drying of pharmaceutical crystalline and amorphous solutes - comparison between experimental - data and theory *Separations Technology* 4 144-155

[88] Thomson R C, Wake M C, Yaszemski M J, Mikos A G (1995) Biodegradable polymer scaffolds to regenerate organs. In: Advances in Polymer Science; Biopolymers II, Peppas NALRS (ed), pp. 245-274

[89] Huang Z M, Zhang Y Z, Kotaki M, Ramakrishna S 2003 A review on polymer nanofibers by electrospinning and their applications in nanocomposites *Composites Science and Technology* 63 2223-2253

[90] Arcaute K, Ochoa L, Mann B K, Wicker R B, Asme (2005) Stereolithography of PEG hydrogel multi-lumen nerve regeneration conduits

[91] Cui T, Yan Y, Zhang R, Liu L, Xu W, Wang X 2009 Rapid prototyping of a double-layer polyurethane-collagen conduit for peripheral nerve regeneration

Tissue Engineering Part C-Methods 15 1-9

[92] Yeong W Y, Chua C K, Leong K F, Chandrasekaran M 2004 Rapid prototyping in tissue engineering: challenges and potential *Trends in Biotechnology* 22 643-652

[93] Peltola S M, Melchels F P W, Grijpma D W, Kellomaki M 2008 A review of rapid prototyping techniques for tissue engineering purposes *Annals of Medicine* 40 268-280

[94] Karalekas D E 2003 Study of the mechanical properties of nonwoven fibre mat reinforced photopolymers used in rapid prototyping *Materials & Design* 24 665-670

[95] Wiria F E, Leong K F, Chua C K, Liu Y 2007 Poly-epsilon-caprolactone/hydroxyapatite for tissue engineering scaffold fabrication via selective laser sintering *Acta Biomaterialia* 3 1-12

[96] Hutmacher D W, Schantz T, Zein I, Ng K W, Teoh S H, Tan K C 2001 Mechanical properties and cell cultural response of polycaprolactone scaffolds designed and fabricated via fused deposition modeling *J. Biomed. Mater. Res.* 55 203-216

[97] Lam C X F, Mo X M, Teoh S H, Hutmacher D W 2002 Scaffold development using 3D printing with a starch-based polymer *Materials Science & Engineering C-Biomimetic and Supramolecular Systems* 20 49-56

[98] Khalil S, Sun W 2009 Bioprinting endothelial cells with alginate for 3D tissue constructs *Journal of Biomechanical Engineering-Transactions of the Asme* 131

[99] Mironov V, Kasyanov V, Drake C, Markwald R R 2008 Organ printing: promises and challenges *Regenerative Medicine* 3 93-103

[100] Yu D, Li Q, Mu X, Chang T, Xiong Z 2008 Bone regeneration of critical calvarial defect in goat model by PLGA/TCP/rhBMP-2 scaffolds prepared by low-temperature rapid-prototyping technology *International Journal of Oral and Maxillofacial Surgery* 37 929-934

[101] Schmidt C E, Leach J B 2003 Neural tissue engineering: Strategies for repair and regeneration *Annual Review of Biomedical Engineering* 5 293-347

[102] Willerth S M, Sakiyama-Elbert S E 2007 Approaches to neural tissue engineering using scaffolds for drug delivery *Advanced Drug Delivery Reviews* 59 325-338

[103] Mueller B K 1999 Growth cone guidance: First steps towards a deeper understanding *Annual Review of Neuroscience* 22 351-388

[104] Baldwin S P, Saltzman W M 1998 Materials for protein delivery in tissue engineering *Advanced Drug Delivery Reviews* 33 71-86

[105] Basmanav F B, Kose G T, Hasirci V 2008 Sequential growth factor delivery from complexed microspheres for bone tissue engineering *Biomaterials* 29 4195-4204

[106] Chen F M, Zhang M, Wu Z F 2010 Toward delivery of multiple growth factors in tissue engineering *Biomaterials* 31 6279-6308

[107] Dodla M C, Bellamkonda R V 2006 Anisotropic scaffolds facilitate enhanced neurite extension in vitro *Journal of Biomedical Materials Research Part A* 78A

213-221

[108] Li G N, Hoffman-Kim D 2008 Tissue-engineered platforms of axon guidance *Tissue Engineering Part B-Reviews* 14 33-51

[109] Cheng M Y, Cao W L, Cao Y, Gong Y D, Zhao N M, Zhang X F 2003 Studies on nerve cell affinity of biodegradable modified chitosan films *Journal of Biomaterials Science-Polymer Edition* 14 1155-1167

[110] Shoichet M S, Yu L M Y, Levesque S G, Wylie R, Aizawa Y, Kim H, Rahman N 2007 Peptide modification of biomaterials enhances cellular interactions and guidance *Biopolymers* 88 518-518

[111] Smeal R M, Rabbitt R, Biran R, Tresco P A 2005 Substrate curvature influences the direction of nerve outgrowth *Annals of Biomedical Engineering* 33 376-382

[112] Dickson B J 2002 Molecular mechanisms of axon guidance *Science* 298 1959-1964

[113] Boyd J G, Gordon T 2003 Neurotrophic factors and their receptors in axonal regeneration and functional recovery after peripheral nerve injury *Molecular Neurobiology* 27 277-323

[114] Jones D M, Tucker B A, Rahimtula M, Mearow K M 2003 The synergistic effects of NGF and IGF-1 on neurite growth in adult sensory neurons: convergence on the PI 3-kinase signaling pathway *Journal of Neurochemistry* 86 1116-1128

[115] Farrar N R, Spencer G E 2008 Pursuing a 'turning point' in growth cone research *Developmental Biology* 318 102-111

[116] Ragaert K, Cardon L, Dekeyser A, Degrieck J Machine design and processing considerations for the 3D plotting of thermoplastic scaffolds *Biofabrication* 2

[117] Lv Q A, Feng Q L, Hu K, Cui F Z 2005 Three-dimensional fibroin/collagen scaffolds derived from aqueous solution and the use for HepG2 culture *Polymer* 46 12662-12669

[118] Richardson S M, Curran J M, Chen R, Vaughan-Thomas A, Hunt J A, Freemont A J, Hoyland J A 2006 The differentiation of bone marrow mesenchymal stem cells into chondrocyte-like cells on poly-L-lactic acid (PLLA) scaffolds *Biomaterials* 27 4069-4078

[119] van Lenthe G H, Hagenmuller H, Bohner M, Hollister S J, Meinel L, Muller R 2007 Nondestructive micro-computed tomography for biological imaging and quantification of scaffold-bone interaction in vivo *Biomaterials* 28 2479-2490

[120] Zhu N, Chen X B, Chapman D 2010 A brief review of visualization techniques for nerve tissue engineering *Journal of Biomimetics, Biomaterials and Tissue Engineering* 7 81-89

[121] Kao T, Connor D, Dilmanian F A, Faulconer L, Liu T, Parham C, Pisano E D, Zhong Z 2009 Characterization of diffraction-enhanced imaging contrast in breast cancer *Physics in Medicine and Biology* 54 3247-3256

[122] Woerly S, Plant G W, Harvey A R 1996 Neural tissue engineering: From polymer to biohybrid organs *Biomaterials* 17 301-310

[123] Yarlagadda P, Chandrasekharan M, Shyan J Y M 2005 Recent advances and current developments in tissue scaffolding *Bio-Medical Materials and*

Engineering 15 159-177

[124] Hutmacher D W 2000 Scaffolds in tissue engineering bone and cartilage *Biomaterials* 21 2529-2543

[125] Hendee W R, Cleary K, Ehman R L, Fullerton G D, Grundfest W S, Haller J, Kelley C, Meyer A E, Murphy R F, Phillips W, Torchilin V P 2008 Bioengineering and imaging research opportunities workshop V: A summary *Annals of Biomedical Engineering* 36 1315-1321

[126] Cyster L A, Grant D M, Howdle S M, Rose F, Irvine D J, Freeman D, Scotchford C A, Shakesheff K M 2005 The influence of dispersant concentration on the pore morphology of hydroxyapatite ceramics for bone tissue engineering *Biomaterials* 26 697-702

[127] Li H Y, Chang J 2004 Fabrication and characterization of bioactive wollastonite/PHBV composite scaffolds *Biomaterials* 25 5473-5480

[128] Zhang L, Li Y B, Wang X J, Wei J, Peng X L 2005 Studies on the porous scaffold made of the nano-HA/PA66 composite *Journal of Materials Science* 40 107-110

[129] Bhattarai N, Edmondson D, Veiseh O, Matsen F A, Zhang M Q 2005 Electrospun chitosan-based nanofibers and their cellular compatibility *Biomaterials* 26 6176-6184

[130] Newman K D, McBurney M W 2004 Poly(D,L lactic-co-glycolic acid) microspheres as biodegradable microcarriers for pluripotent stem cells *Biomaterials* 25 5763-5771

[131] Bian Y Z, Wang Y, Aibaidoula G, Chen G Q, Wu Q 2009 Evaluation of poly(3-hydroxybutyrate-co-3-hydroxyhexanoate) conduits for peripheral nerve regeneration *Biomaterials* 30 217-225

[132] Lee M, Dunn J C Y, Wu B M 2005 Scaffold fabrication by indirect three-dimensional printing *Biomaterials* 26 4281-4289

[133] Wu L B, Ding J D 2004 In vitro degradation of three-dimensional porous poly(D,L-lactide-co-glycolide) scaffolds for tissue engineering *Biomaterials* 25 5821-5830

[134] He L M, Liao S S, Quan D P, Ngiam M, Chan C K, Ramakrishna S, Lu J 2009 The influence of laminin-derived peptides conjugated to Lys-capped PLLA on neonatal mouse cerebellum C17.2 stem cells *Biomaterials* 30 1578-1586

[135] Bozkurt A, Deumens R, Beckmann C, Damink L O, Schugner F, Heschel I, Sellhaus B, Weis J, Jahnen-Dechent W, Brook G A, Pallua N 2009 In vitro cell alignment obtained with a Schwann cell enriched microstructured nerve guide with longitudinal guidance channels *Biomaterials* 30 169-179

[136] Muscariello L, Rosso F, Marino G, Giordano A, Barbarisi M, Cafiero G, Barbarisi A 2005 A critical overview of ESEM applications in the biological field *Journal of Cellular Physiology* 205 328-334

[137] Martinez E, Engel E, Lopez-Iglesias C, Mills C A, Planell J A, Samitier J 2008 Focused ion beam/scanning electron microscopy characterization of cell behavior on polymer micro-/nanopatterned substrates: A study of cell-substrate interactions *Micron* 39 111-116

[138] Greve F, Frerker S, Bittermann A G, Burkhardt C, Hierlemann A, Hall H 2007 Molecular design and characterization of the neuron-microelectrode array interface *Biomaterials* 28 5246-5258

[139] Nomura H, Baladie B, Katayama Y, Morshead C M, Shoichet M S, Tator C H 2008 Delayed implantation of intramedullary chitosan channels containing nerve grafts promotes extensive axonal regeneration after spinal cord injury *Neurosurgery* 63 127-141

[140] Nomura H, Zahir T, Kim H, Katayama Y, Kulbatski I, Morshead C M, Shoichet M S, Tator C H 2008 Extramedullary chitosan channels promote survival of transplanted neural stem and progenitor cells and create a tissue bridge after complete spinal cord transection *Tissue Eng. Part A* 14 649-665

[141] Wang Y F, Hand A R, Gillies C, Grunnet M L, Cone R E, O'Rourke J 1997 Morphologic evidence for a preferential storage of tissue plasminogen activator (t-PA) in perivascular axons of the rat uvea *Experimental Eye Research* 65 105-116

[142] Derosier D J, Klug A 1968 Reconstruction of 3 dimensional structures from electron micrographs *Nature* 217 130-134

[143] Pawley J B (2006) Handbook of Biological Confocal Microscopy (3rd ed.). Springer, Berlin

[144] Crompton K E, Goud J D, Bellamkonda R V, Gengenbach T R, Finkelstein D I, Horne M K, Forsythe J S 2007 Polylysine-functionalised thermoresponsive chitosan hydrogel for neural tissue engineering *Biomaterials* 28 441-449

[145] Sun T, Jackson S, Haycock J W, MacNeil S 2006 Culture of skin cells in 3D rather than 2D improves their ability to survive exposure to cytotoxic agents *Journal of Biotechnology* 122 372-381

[146] Qiu K, Zhao X J, Wan C X, Zhao C S, Chen Y W 2006 Effect of strontium ions on the growth of ROS17/2.8 cells on porous calcium polyphosphate scaffolds *Biomaterials* 27 1277-1286

[147] Turner N J, Kielty C M, Walker M G, Canfield A E 2004 A novel hyaluronan-based biomaterial (Hyaff-11((R))) as a scaffold for endothelial cells in tissue engineered vascular grafts *Biomaterials* 25 5955-5964

[148] Patz T M, Doraiswamy A, Narayan R J, He W, Zhong Y, Bellamkonda R, Modi R, Chrisey D B 2006 Three-dimensional direct writing of B35 neuronal cells *Journal of Biomedical Materials Research Part B-Applied Biomaterials* 78B 124-130

[149] Balgude A P, Yu X, Szymanski A, Bellamkonda R V 2001 Agarose gel stiffness determines rate of DRG neurite extension in 3D cultures *Biomaterials* 22 1077-1084

[150] Sorensen A, Alekseeva T, Katechia K, Robertson M, Riehle M O, Barnett S C 2007 Long-term neurite orientation on astrocyte monolayers. aligned by microtopography *Biomaterials* 28 5498-5508

[151] Luo Y, Shoichet M S 2004 A photolabile hydrogel for guided three-dimensional cell growth and migration *Nature Materials* 3 249-253

[152] Wosnick J H, Shoichet M S 2008 Three-dimensional chemical Patterning of

transparent hydrogels *Chemistry of Materials* 20 55-60

[153] Labbe A, Liang H, Martin C, Brignole-Baudouin F, Warnet J M, Baudouin C 2006 Comparative anatomy of laboratory animal corneas with a new-generation high-resolution in vivo confocal microscope *Current Eye Research* 31 501-509

[154] Lagali N S, Griffith M, Shinozaki N, Fagerholm P, Munger R 2007 Innervation of tissue-engineered corneal implants in a porcine model: A 1-year in vivo confocal microscopy study *Investigative Ophthalmology & Visual Science* 48 3537-3544

[155] Lagali N, Griffith M, Fagerholm P, Merrett K, Huynh M, Munger R 2008 Innervation of tissue-engineered recombinant human collagen-based corneal substitutes: A comparative in vivo confocal microscopy study *Investigative Ophthalmology & Visual Science* 49 3895-3902

[156] White N S, Errington R J 2005 Fluorescence techniques for drug delivery research: theory and practice *Advanced Drug Delivery Reviews* 57 17-42

[157] Pygall S R, Whetstone J, Timmins P, Melia C D 2007 Pharmaceutical applications of confocal laser scanning microscopy: The physical characterisation of pharmaceutical systems *Advanced Drug Delivery Reviews* 59 1434-1452

[158] Ballios B G, Cooke M J, van der Kooy D, Shoichet M S 2010 A hydrogel-based stem cell delivery system to treat retinal degenerative diseases *Biomaterials* 31 2555-2564

[159] Fu K, Pack D W, Klibanov A M, Langer R 2000 Visual evidence of acidic

environment within degrading poly(lactic-co-glycolic acid) (PLGA) microspheres *Pharmaceutical Research* 17 100-106

[160] Du T, Wasser M 2009 3D image stack seconstruction in live cell microscopy of drosophila muscles and its validation *Cytometry Part A* 75A 329-343

[161] Stuart G J, Palmer L M 2006 Imaging membrane potential in dendrites and axons of single neurons *Pflugers Archiv-European Journal of Physiology* 453 403-410

[162] Bonse U, Busch F 1996 X-ray computed microtomography (mu CT) using synchrotron radiation (SR) *Progress in Biophysics & Molecular Biology* 65 133-169

[163] Halligan S, Fenlon H M 1999 Science, medicine, and the future - Virtual colonoscopy *British Medical Journal* 319 1249-1252

[164] Komlev V S, Peyrin F, Mastrogiacomo M, Cedola A, Papadimitropoulos A, Rustichelli F, Cancedda R 2006 Kinetics of in vivo bone deposition by bone marrow stromal cells into porous calcium phosphate scaffolds: An X-ray computed microtomography study *Tissue Engineering* 12 3449-3458

[165] Lane M J, Liu D M, Huynh M D, Jeffrey R B, Mindelzun R E, Katz D S 1999 Suspected acute appendicitis: Nonenhanced helical CT in 300 consecutive patients *Radiology* 213 341-346

[166] Barrere F, Mahmood T A, de Groot K, van Blitterswijk C A 2008 Advanced biomaterials for skeletal tissue regeneration: Instructive and smart functions *Materials Science & Engineering R-Reports* 59 38-71

[167] Balto K, Muller R, Carrington D C, Dobeck J, Stashenko P 2000 Quantification of periapical bone destruction in mice by micro-computed tomography *Journal of Dental Research* 79 35-40

[168] Graichen H, Lochmuller E M, Wolf E, Langkabel B, Stammberger T, Haubner M, Renner-Muller I, Englmeier K H, Eckstein F 1999 A non-destructive technique for 3-D microstructural phenotypic characterisation of bones in genetically altered mice: preliminary data in growth hormone transgenic animals and normal controls *Anatomy and Embryology* 199 239-248

[169] Yamashita T, Nabeshima Y, Noda M 2000 High-resolution micro-computed tomography analyses of the abnormal trabecular bone structures in klotho gene mutant mice *Journal of Endocrinology* 164 239-245

[170] Nuzzo S, Peyrin F, Cloetens P, Baruchel J 2002 Quantification of the degree of mineralization of bone in three dimensions using synchrotron radiation microtomography *Medical Physics* 29 2672-2681

[171] Salome M, Peyrin F, Cloetens P, Odet C, Laval-Jeantet A M, Baruchel J, Spanne P 1999 A synchrotron radiation microtomography system for the analysis of trabecular bone samples *Medical Physics* 26 2194-2204

[172] Landis E N, Nagy E N, Keane D T 2003 Microstructure and fracture in three dimensions *Engineering Fracture Mechanics* 70 911-925

[173] Lin A S P, Barrows T H, Cartmell S H, Guldberg R E 2003 Microarchitectural and mechanical characterization of oriented porous polymer scaffolds *Biomaterials* 24 481-489

[174] Wang F, Shor L, Darling A, Khalil S, Sun W, Guceri S, Lau A 2004 Precision extruding deposition and characterization of cellular poly-epsilon-caprolactone tissue scaffolds *Rapid Prototyping Journal* 10 42-49

[175] Karande T S, Ong J L, Agrawal C M 2004 Diffusion in musculoskeletal tissue engineering scaffolds: Design issues related to porosity, permeability, architecture, and nutrient mixing *Annals of Biomedical Engineering* 32 1728-1743

[176] Ishaug S L, Crane G M, Miller M J, Yasko A W, Yaszemski M J, Mikos A G 1997 Bone formation by three-dimensional stromal osteoblast culture in biodegradable polymer scaffolds *J. Biomed. Mater. Res.* 36 17-28

[177] Silva N A, Salgado A J, Sousa R A, Oliveira J T, Pedro A J, Leite-Almeida H, Cerqueira R, Almeida A, Mastronardi F, Mano J F, Neves N M, Sousa N, Reis R L 2010 Development and characterization of a novel hybrid tissue engineering-based scaffold for spinal cord injury repair *Tissue Eng. Part A* 16 45-54

[178] Mano J F, Hungerford G, Ribelles J L G 2008 Bioactive poly(L-lactic acid)-chitosan hybrid scaffolds *Materials Science & Engineering C-Biomimetic and Supramolecular Systems* 28 1356-1365

[179] Ashammakhi N, Papp A, Sayed R, Ruuskanen M, Kallioinen M, Kellomaki M, Waris T, Seppala J, Tormala P 1999 Histological evaluation of poly(L-lactide/epsiloncaprolactone) membrane implanted subcutaneously in rats *Annales Chirurgiae et Gynaecologiae* 88 313-317

[180] Schuknecht H F (1974) The pathology of the ear. Harvard University Press, Boston

[181] Hagenmueller H, Hofmann S, Kohler T, Merkle H P, Kaplan D L, Vunjak-Novakovic G, Mueller R, Meinel L 2007 Non-invasive time-lapsed monitoring and quantification of engineered bone-like tissue *Annals of Biomedical Engineering* 35 1657-1667

[182] Peyrin F, Mastrogiacomo M, Cancedda R, Martinetti R 2007 SEM and 3D synchrotron radiation micro-tomography in the study of bioceramic scaffolds for tissue-engineering applications *Biotechnology and Bioengineering* 97 638-648

[183] Williams J M, Adewunmi A, Schek R M, Flanagan C L, Krebsbach P H, Feinberg S E, Hollister S J, Das S 2005 Bone tissue engineering using polycaprolactone scaffolds fabricated via selective laser sintering *Biomaterials* 26 4817-4827

[184] Zeltinger J, Sherwood J K, Graham D A, Mueller R, Griffith L G 2001 Effect of pore size and void fraction on cellular adhesion, proliferation, and matrix deposition *Tissue Engineering* 7 557-572

[185] Cartmell S, Huynh K, Lin A, Nagaraja S, Guldberg R 2004 Quantitative microcomputed tomography analysis of mineralization within three-dimensional scaffolds in vitro *Journal of Biomedical Materials Research Part A* 69A 97-104

[186] Heinzer S, Krucker T, Stampanoni M, Abela R, Meyer E P, Schuler A,

Schneider P, Muller R 2006 Hierarchical microimaging for multiscale analysis of large vascular networks *Neuroimage* 32 626-636

[187] Uzun H, Curthoys I S, Jones A S 2007 A new approach to visualizing the membranous structures of the inner ear - high resolution X-ray micro-tomography *Acta Oto-Laryngologica* 127 568-573

[188] Lareida A, Beckmann F, Schrott-Fischer A, Glueckert R, Freysinger W, Muller B 2009 High-resolution X-ray tomography of the human inner ear: synchrotron radiation-based study of nerve fibre bundles, membranes and ganglion cells *Journal of Microscopy-Oxford* 234 95-102

[189] Uebersax L, Hagenmueller H, Hofmann S, Gruenblatt E, Mueller R, Vunjak-Novakovic G, Kaplan D L, Merkle H P, Meinel L 2006 Effect of scaffold design on bone morphology in vitro *Tissue Engineering* 12 3417-3429

[190] Muller B, Fischer J, Dietz U, Thurner P J, Beckmann F 2006 Blood vessel staining in the myocardium for 3D visualization down to the smallest capillaries *Nuclear Instruments & Methods in Physics Research Section B-Beam Interactions with Materials and Atoms* 246 254-261

[191] Toyota E, Fujimoto K, Ogasawara Y, Kajita T, Shigeto F, Matsumoto T, Goto M, Kajiya F 2002 Dynamic changes in three-dimensional architecture and vascular volume of transmural coronary microvasculature between diastolic- and systolic-arrested rat hearts *Circulation* 105 621-626

[192] Duvall C L, Taylor W R, Weiss D, Guldberg R E 2004 Quantitative microcomputed tomography analysis of collateral vessel development after

ischemic injury *American Journal of Physiology-Heart and Circulatory Physiology* 287 H302-H310

[193] Bolland B, Kanczler J M, Ginty P J, Howdle S M, Shakesheff K M, Dunlop D G, Oreffo R O C 2008 The application of human bone marrow stromal cells and poly(DL-lactic acid) as a biological bone graft extender in impaction bone grafting *Biomaterials* 29 3221-3227

[194] Thurner P, Muller B, Beckmann F, Weitkamp T, Rau C, Muller R, Hubbell J A, Sennhauser U 2003 Tomography studies of human foreskin fibroblasts on polymer yarns *Nuclear Instruments & Methods in Physics Research Section B-Beam Interactions with Materials and Atoms* 200 397-405

[195] Thurner P, Muller R, Raeber G, Sennhauser U, Hubbell J 2005 3D Morphology of cell cultures: A quantitative approach using micrometer synchrotron light tomography *Microscopy Research and Technique* 66 289-298

[196] Thurner P, Muller B, Sennhauser U, Hubbell J, Muller R 2004 Tomography studies of biological cells on polymer scaffolds *Journal of Physics-Condensed Matter* 16 S3499-S3510

[197] Juurlink B H J, Devon R M 1991 Colloidal gold as a permanent marker of cells *Experientia* 47 75-77

[198] Hall C J, Schultke E, Rigon L, Ataelmannan K, Rigley S, Menk R, Arfellie F, Tromba G, Pearson S, Wilkinson S, Round A, Crittell S, Griebel R, Juurlink B H J 2008 Synchrotron-based in vivo tracking of implanted mammalian cells *European Journal of Radiology* 68 S156-S159

[199] Beckmann F, Bonse U, Busch F, Gunnewig O 1997 X-ray microtomography (mu CT) using phase contrast for the investigation of organic matter *Journal of Computer Assisted Tomography* 21 539-553

[200] Beckmann F, Heise K, Kolsch B, Bonse U, Rajewsky M F, Bartscher M, Biermann T 1999 Three-dimensional imaging of nerve tissue by x-ray phase-contrast microtomography *Biophysical Journal* 76 98-102

[201] Kim B I, Kim K H, Youn H S, Jheon S, Kim J K, Kim H 2008 High resolution X-ray phase contrast synchrotron imaging of normal and ligation damaged rat sciatic nerves *Microscopy Research and Technique* 71 443-447

[202] Zehbe R, Haibel A, Riesemeier H, Gross U, Kirkpatrick C J, Schubert H, Brochhausen C 2010 Going beyond histology. Synchrotron micro-computed tomography as a methodology for biological tissue characterization: from tissue morphology to individual cells *Journal of the Royal Society Interface* 7 49-59

[203] Bravin A 2003 Exploiting the x-ray refraction contrast with an analyser: the state of the art *Journal of Physics D-Applied Physics* 36 A24-A29

[204] Chapman D, Thomlinson W, Johnston R E, Washburn D, Pisano E, Gmur N, Zhong Z, Menk R, Arfelli F, Sayers D 1997 Diffraction enhanced x-ray imaging *Physics in Medicine and Biology* 42 2015-2025

[205] Hasnah M O, Zhong Z, Oltulu O, Pisano E, Johnston R E, Sayers D, Thomlinson W, Chapman D 2002 Diffraction enhanced imaging contrast mechanisms in breast cancer specimens *Medical Physics* 29 2216-2221

[206] Li H, Zhang L, Wang X Y, Wang T L, Wang B E, Zhao X Y, Luo S Q 2009

Investigation of hepatic fibrosis in rats with x-ray diffraction enhanced imaging *Applied Physics Letters* 94 124101

[207] Peng Y F, Chen S L, Tang G Y, Chen Y S, Shen R J, Chenb A P, Zhu P P, Huang W X, Yuan Q X 2007 Diffraction-enhanced imaging with synchrotron radiation X-ray for liver *Journal of X-Ray Science and Technology* 15 97-100

[208] Liu C L, Zhang Y, Zhang X Y, Yang W T, Peng W J, Shi D R, Zhu P P, Huang W X, Yuan Q X 2005 Diffraction enhanced imaging of breast tissue *High Energy Physics and Nuclear Physics-Chinese Edition* 29 130-132

[209] Connor D M, Sayers D, Sumner D R, Zhong Z 2006 Diffraction enhanced imaging of controlled defects within bone, including bone-metal gaps *Physics in Medicine and Biology* 51 3283-3300

[210] Li J, Zhong Z, Lidtke R, Kuettner K E, Peterfy C, Aliyeva E, Muehleman C 2003 Radiography of soft tissue of the foot and ankle with diffraction enhanced imaging *Journal of Anatomy* 202 463-470

[211] Bravin A, Keyrilainen J, Fernandez M, Fiedler S, Nemoz C, Karjalainen-Lindsberg M L, Tenhunen M, Virkkunen P, Leidenius M, von Smitten K, Sipila P, Suortti P 2007 High-resolution CT by diffraction-enhanced x-ray imaging: mapping of breast tissue samples and comparison with their histo-pathology *Physics in Medicine and Biology* 52 2197-2211

[212] Zhong Z, Thomlinson W, Chapman D, Sayers D 2000 Implementation of diffraction-enhanced imaging experiments: at the NSLS and APS *Nuclear Instruments & Methods in Physics Research Section a-Accelerators*

Spectrometers Detectors and Associated Equipment 450 556-567

[213] Mooney D J, Baldwin D F, Suh N P, Vacanti L P, Langer R 1996 Novel approach to fabricate porous sponges of poly(D,L-lactic-co-glycolic acid) without the use of organic solvents *Biomaterials* 17 1417-1422

[214] Freed L E, Vunjaknovakovic G, Biron R J, Eagles D B, Lesnoy D C, Barlow S K, Langer R 1994 Biodegradable polymer scaffolds for tissue engineering *Bio-Technology* 12 689-693

[215] Kim G E, Kim H D, Lee D S 2002 Effect of added Pluronics on fabrication of poly(L-lactic acid) scaffold via thermally-induced phase separation *Polymer-Korea* 26 821-828

[216] Chen X B, Li M G, Ke H 2008 Modeling of the flow rate in the dispensing-based process for fabricating tissue scaffolds *Journal of Manufacturing Science and Engineering-Transactions of the Asme* 130 21003

[217] Geng L, Feng W, Hutmacher D W, Wong Y S, Loh H T, Fuh J Y H 2005 Direct writing of chitosan scaffolds using a robotic system *Rapid Prototyping Journal* 11 90-97

[218] Xu W, Wang X H, Yan Y N, Zhang R J 2008 Rapid prototyping of polyurethane for the creation of vascular systems *Journal of Bioactive and Compatible Polymers* 23 103-114

[219] Nie Z H, Kumacheva E 2008 Patterning surfaces with functional polymers *Nature Materials* 7 277-290

[220] Di Martino A, Sittinger M, Risbud M V 2005 Chitosan: A versatile biopolymer

for orthopaedic tissue-engineering *Biomaterials* 26 5983-5990

[221] Chupa J M, Foster A M, Sumner S R, Madihally S V, Matthew H W T 2000 Vascular cell responses to polysaccharide materials: in vitro and in vivo evaluations *Biomaterials* 21 2315-2322

[222] Elcin Y M, Dixit V, Gitnick G 1998 Hepatocyte attachment on biodegradable modified chitosan membranes: In vitro evaluation for the development of liver organoids *Artificial Organs* 22 837-846

[223] Boryniec S, Ratajska M, Strobin G 1996 Biodegradation of chitosan *Polimery* 41 564-567

[224] VandeVord P J, Matthew H W T, DeSilva S P, Mayton L, Wu B, Wooley P H 2002 Evaluation of the biocompatibility of a chitosan scaffold in mice *J. Biomed. Mater. Res.* 59 585-590

[225] Yang F, Li X H, Cheng M Y, Gong Y D, Zhao N M, Zhang X F, Yang Y Y 2002 Performance modification of chitosan membranes induced by gamma irradiation *Journal of Biomaterials Applications* 16 215-226

[226] Madihally S V, Matthew H W T 1999 Porous chitosan scaffolds for tissue engineering *Biomaterials* 20 1133-1142

[227] Gingras M, Paradis I, Berthod F 2003 Nerve regeneration in a collagen-chitosan tissue-engineered skin transplanted on nude mice *Biomaterials* 24 1653-1661

[228] Zhu N, Cui F Z, Hu K, Zhu L 2007 Biomedical modification of poly(L-lactide) by blending with lecithin *Journal of Biomedical Materials Research Part A* 82A 455-461

[229] GarciaAlonso L, Fetter R D, Goodman C S 1996 Genetic analysis of laminin A in drosophila: Extracellular matrix containing laminin A is required for ocellar axon pathfinding *Development* 122 2611-2621

[230] Itoh S, Takakuda K, Samejima H, Ohta T, Shinomiya K, Ichinose S 1999 Synthetic collagen fibers coated with a synthetic peptide containing the YIGSR sequence of laminin to promote peripheral nerve regeneration in vivo *Journal of Materials Science-Materials in Medicine* 10 129-134

[231] Lindsay R M 1988 Nerve growth-factors (NGF, BDNF) enhance axonal regeneration but are not required for survival of adult sensory neurons *Journal of Neuroscience* 8 2394-2405

[232] Schreyer D J, Andersen P L, Williams K, Kosatka I, Truong T N 1997 Quantitative analysis of GAP-43 expression by neurons in microcultures using cell-ELISA *Journal of Neuroscience Methods* 72 137-145

[233] Schreyer D J, Skene J H P 1991 Fate of GAP-43 in ascending spinal axons of drg neurons after peripheral-nerve injury - delayed accumulation and correlation with regenerative potential *Journal of Neuroscience* 11 3738-3751

[234] Britland S, Morgan H, WojiakStodart B, Riehle M, Curtis A, Wilkinson C 1996 Synergistic and hierarchical adhesive and topographic guidance of BHK cells *Experimental Cell Research* 228 313-325

[235] Johansson F, Carlberg P, Danielsen N, Montelius L, Kanje M 2006 Axonal outgrowth on nano-imprinted patterns *Biomaterials* 27 1251-1258

[236] Bonner J, O'Connor T P 2001 The permissive cue laminin is essential for

growth cone turning in vivo *Journal of Neuroscience* 21 9782-9791

[237] Renaudin A, Lehmann M, Girault J A, McKerracher L 1999 Organization of point contacts in neuronal growth cones *Journal of Neuroscience Research* 55 458-471

[238] Arregui C O, Carbonetto S, McKerracher L 1994 Characterization of neural cell-adhesion sites - point contacts are the sites of interaction between integrins and the cytoskeleton in PC12 cells *Journal of Neuroscience* 14 6967-6977

[239] Rangappa N, Romero A, Nelson K D, Eberhart R C, Smith G M 2000 Laminin-coated poly(L-lactide) filaments induce robust neurite growth while providing directional orientation *J. Biomed. Mater. Res.* 51 625-634

[240] Francisco H, Yellen B B, Halverson D S, Friedman G, Gallo G 2007 Regulation of axon guidance and extension by three-dimensional constraints *Biomaterials* 28 3398-3407

[241] Oliva A A, James C D, Kingman C E, Craighead H G, Banker G A 2003 Patterning axonal guidance molecules using a novel strategy for microcontact printing *Neurochemical Research* 28 1639-1648

[242] Von Philipsborn A C, Lang S, Bernard A, Loeschinger J, David C, Lehnert D, Bastmeyer M, Bonhoeffer F 2006 Microcontact printing of axon guidance molecules for generation of graded patterns *Nature Protocols* 1 1322-1328

[243] Zein I, Hutmacher D W, Tan K C, Teoh S H 2002 Fused deposition modeling of novel scaffold architectures for tissue engineering applications *Biomaterials* 23 1169-1185

[244] Owen S C, Shoichet M S 2010 Design of three-dimensional biomimetic scaffolds *Journal of Biomedical Materials Research Part A* 94A 1321-1331

[245] Yang S F, Leong K F, Du Z H, Chua C K 2001 The design of scaffolds for use in tissue engineering. Part 1. Traditional factors *Tissue Engineering* 7 679-689

[246] Hutmacher D W, Sittinger M, Risbud M V 2004 Scaffold-based tissue engineering: rationale for computer-aided design and solid free-form fabrication systems *Trends in Biotechnology* 22 354-362

[247] Kim J Y, Cho D W 2009 The optimization of hybrid scaffold fabrication process in precision deposition system using design of experiments *Microsystem Technologies-Micro-and Nanosystems-Information Storage and Processing Systems* 15 843-851

[248] Lee J H, Park S A, Park K, Kim J H, Kim K S, Lee J, Kim W 2010 Fabrication and characterization of 3D scaffold using 3D plotting system *Chinese Science Bulletin* 55 94-98

[249] Shor L, Guceri S, Wen X J, Gandhi M, Sun W 2007 Fabrication of three-dimensional polycaprolactone/hydroxyapatite tissue scaffolds and osteoblast-scaffold interactions in vitro *Biomaterials* 28 5291-5297

[250] Landers R, Pfister A, Hubner U, John H, Schmelzeisen R, Mulhaupt R 2002 Fabrication of soft tissue engineering scaffolds by means of rapid prototyping techniques *Journal of Materials Science* 37 3107-3116

[251] Pham C B, Leong K F, Lim T C, Chian K S 2008 Rapid freeze prototyping technique in bio-plotters for tissue scaffold fabrication *Rapid Prototyping*

Journal 14 246-253

[252] Yan Y N, Xiong Z, Hu Y Y, Wang S G, Zhang R J, Zhang C 2003 Layered manufacturing of tissue engineering scaffolds via multi-nozzle deposition *Materials Letters* 57 2623-2628

[253] Hu J A, Sun X A, Ma H Y, Xie C Q, Chen Y E, Ma P X 2010 Porous nanofibrous PLLA scaffolds for vascular tissue engineering *Biomaterials* 31 7971-7977

[254] Morelli S, Salerno S, Piscioneri A, Papenburg B J, Di Vito A, Giusi G, Canonaco M, Stamatialis D, Drioli E, De Bartolo L 2010 Influence of micro-patterned PLLA membranes on outgrowth and orientation of hippocampal neurites *Biomaterials* 31 7000-7011

[255] Zhang Q W, NeitzeI I, Mochalin V N, Knoke I, Wotton D M, Gogotsi Y, Lelkes P I, Zhou J G, Asme (2010) PLLA-nanodiamond composites and their application in bone tissue engineering

[256] Abarrategi A, Lopiz-Morales Y, Ramos V, Civantos A, Lopez-Duran L, Marco F, Lopez-Lacomba J L 2010 Chitosan scaffolds for osteochondral tissue regeneration *Journal of Biomedical Materials Research Part A* 95A 1132-1141

[257] Guo B F, Dong M M 2009 Application of neural stem cells in tissue-engineered artificial nerve *Otolaryngology-Head and Neck Surgery* 140 159-164

[258] Zeng R, Tu M, Liu H W, Zhao J H, Zha Z G, Zhou C R 2009 Preparation, structure, drug release and bioinspired mineralization of chitosan-based nanocomplexes for bone tissue engineering *Carbohydrate Polymers* 78 107-111

[259] Denkbas E B, Ottenbrite R M 2006 Perspectives on: Chitosan drug delivery systems based on their geometries *Journal of Bioactive and Compatible Polymers* 21 351-368

[260] Nagpal K, Singh S K, Mishra D N 2010 Chitosan nanoparticles: A promising system in novel drug delivery *Chemical & Pharmaceutical Bulletin* 58 1423-1430

[261] Li M G, Tian X Y, Chen X B 2009 Modeling of flow rate, pore size, and porosity for the dispensing-based tissue scaffolds fabrication *Journal of Manufacturing Science and Engineering-Transactions of the Asme* 131 034501

[262] Zhu N, Li M G, Yuan Y J, Schreyer D J, Chen X B 2010 Effects of laminin blended with chitosan on axon guidance on patterned substrates *Biofabrication* 2 045002

[263] Karageorgiou V, Kaplan D 2005 Porosity of 3D biornaterial scaffolds and osteogenesis *Biomaterials* 26 5474-5491

[264] Dong H Y, Meng B, Zhu N, Cui F Z 2006 Biomineralization of five polymers in human bile *Materials Science & Engineering C-Biomimetic and Supramolecular Systems* 26 670-674

[265] Li X M, Feng Q L 2005 Porous poly-L-lactic acid scaffold reinforced by chitin fibers *Polymer Bulletin* 54 47-55

[266] Wang X H, Li D P, Wang W J, Feng Q L, Cui F Z, Xu Y X, Song X H, van der Werf M 2003 Crosslinked collagen/chitosan matrix for artificial livers *Biomaterials* 24 3213-3220

[267] Kim H, Tator C H, Shoichet M S 2008 Design of protein-releasing chitosan channels *Biotechnology Progress* 24 932-937

[268] Bhumkar D R, Pokharkar V B 2006 Studies on effect of pH on cross-linking of chitosan with sodium tripolyphosphate: A technical note *Aaps Pharmscitech* 7 E138-143

[269] Yuan Y, Chesnutt B M, Utturkar G, Haggard W O, Yang Y, Ong J L, Bumgardner J D 2007 The effect of cross-linking of chitosan microspheres with genipin on protein release *Carbohydrate Polymers* 68 561-567

[270] Lee S H, Shin H 2007 Matrices and scaffolds for delivery of bioactive molecules in bone and cartilage tissue engineering *Advanced Drug Delivery Reviews* 59 339-359

[271] Cheung H Y, Lau K T, Lu T P, Hui D 2007 A critical review on polymer-based bio-engineered materials for scaffold development *Composites Part B-Engineering* 38 291-300

[272] Katti D S, Lakshmi S, Langer R, Laurencin C T 2002 Toxicity, biodegradation and elimination of polyanhydrides *Advanced Drug Delivery Reviews* 54 933-961

[273] Ma Z W, Gao C Y, Gong Y H, Shen J C 2005 Cartilage tissue engineering PLLA scaffold with surface immobilized collagen and basic fibroblast growth factor *Biomaterials* 26 1253-1259

[274] Chen V J, Smith L A, Ma P X 2006 Bone regeneration on computer-designed nano-fibrous scaffolds *Biomaterials* 27 3973-3979

[275] Cam D, Hyon S H, Ikada Y 1995 Degradation of high-molecular-weight poly(L-lactide) in alkaline-medium *Biomaterials* 16 833-843

[276] Tsuji H, Nakahara K, Ikarashi K 2001 Poly(L-lactide), 8 - High-temperature hydrolysis of poly(L-lactide) films with different crystallinities and crystalline thicknesses in phosphate-buffered solution *Macromolecular Materials and Engineering* 286 398-406

[277] Grizzi I, Garreau H, Li S, Vert M 1995 Hydrolytic degradation of devices based on poly(DL-lactiv acid) size-dependence *Biomaterials* 16 305-311

[278] Li X M, Feng Q L, Cui F Z 2006 In vitro degradation of porous nano-hydroxyapatite/collagen/PLLA scaffold reinforced by chitin fibres *Materials Science & Engineering C-Biomimetic and Supramolecular Systems* 26 716-720

[279] Alves N M, Mano J F 2008 Chitosan derivatives obtained by chemical modifications for biomedical and environmental applications *International Journal of Biological Macromolecules* 43 401-414

[280] Duarte A R C, Mano J F, Reis R L 2010 Novel 3D scaffolds of chitosan-PLLA blends for tissue engineering applications: Preparation and characterization *Journal of Supercritical Fluids* 54 282-289

[281] Zhu N, Li M G, Cooper D, Chen X B 2011 Development of novel hybrid poly(l-lactide)/chitosan scaffolds using the rapid freeze prototyping technique *Biofabrication* 3 034105

[282] Miyata T, Masuko T 1998 Crystallization behaviour of poly(L-lactide) *Polymer*

39 5515-5521

[283] Widjaja E, Lee W L, Loo S C J 2010 Application of raman microscopy to biodegradable double-walled microspheres *Analytical Chemistry* 82 1277-1282

[284] Bertoluzza A, Fagnano C, Mietti N, Tinti A, Giannini S, Giardino R, Cacciari G L (1998) Vibrational spectroscopy of biodegradable polymers. In: New Biomedical Materials: Basic and Applied Studies, Haris PI, Chapman D (eds), pp. 45-52

[285] Taddei P, Monti P, Simoni R 2002 Vibrational and thermal study on the in vitro and in vivo degradation of a poly(lactic acid)-based bioabsorbable periodontal membrane *Journal of Materials Science-Materials in Medicine* 13 469-475

[286] Fischer E W, Sterzel H J, Wegner G 1973 Investigaion of structure of solution grown crystals of lactide copolymers by means of chemical-reactions *Kolloid-Zeitschrift and Zeitschrift Fur Polymere* 251 980-990

[287] Jiao H S, Yao J, Yang Y M, Chen X, Lin W W, Li Y, Gu X S, Wang X D 2009 Chitosan/polyglycolic acid nerve grafts for axon regeneration from prolonged axotomized neurons to chronically denervated segments *Biomaterials* 30 5004-5018

[288] Vonrecum H A, Cleek R L, Eskin S G, Mikos A G 1995 Degradation of polydispersed poly(L-lactic acid) to modulate lactic-acid release *Biomaterials* 16 441-447

[289] Castner D G, Guldberg R E 2007 Imaging techniques for biomaterials characterization *Biomaterials* 28 2379-2379

[290] Renghini C, Komlev V, Fiori F, Verne E, Baino F, Vitale-Brovarone C 2009 Micro-CT studies on 3-D bioactive glass-ceramic scaffolds for bone regeneration *Acta Biomaterialia* 5 1328-1337

[291] Jones A C, Arns C H, Sheppard A P, Hutmacher D W, Milthorpe B K, Knackstedt M A 2007 Assessment of bone ingrowth into porous biomaterials using micro-CT *Biomaterials* 28 2491-2504

[292] Schmidt C, Bezuidenhout D, Beck M, Van der Merwe E, Zilla P, Davies N 2009 Rapid three-dimensional quantification of VEGF-induced scaffold neovascularisation by microcomputed tomography *Biomaterials* 30 5959-5968

[293] Ford N L, Thornton M M, Holdsworth D W 2003 Fundamental image quality limits for microcomputed tomography in small animals *Medical Physics* 30 2869-2877

[294] Sun W, Lal P 2002 Recent development on computer aided tissue engineering - a review *Computer Methods and Programs in Biomedicine* 67 85-103

[295] Wang G, Yu H Y, De Man B 2008 An outlook on x-ray CT research and development *Medical Physics* 35 1051-1064

[296] Davis T J, Gureyev T E, Gao D, Stevenson A W, Wilkins S W 1995 X-ray image-contrast from a simple phase object *Physical Review Letters* 74 3173-3176

[297] Komlev V S, Mastrogiacomo M, Peyrin F, Cancedda R, Rustichelli F 2009 X-ray synchrotron radiation pseudo-holotomography as a new imaging technique to investigate angio- and microvasculogenesis with no usage of

contrast agents *Tissue Engineering Part C-Methods* 15 425-430

[298] Wilkins S W, Gureyev T E, Gao D, Pogany A, Stevenson A W 1996 Phase-contrast imaging using polychromatic hard X-rays *Nature* 384 335-338

[299] Lewis R A, Hall C J, Hufton A P, Evans S, Menk R H, Arfelli F, Rigon L, Tromba G, Dance D R, Ellis I O, Evans A, Jacobs E, Pinder S E, Rogers K D 2003 X-ray refraction effects: application to the imaging of biological tissues *British Journal of Radiology* 76 301-308

[300] Yuasa T, Hashimoto E, Maksimenko A, Suglyama H, Arai Y, Shimao D, Ichihara S, Ando M 2008 Highly sensitive detection of the soft tissues based on refraction contrast by in-plane diffraction-enhanced imaging CT *Nuclear Instruments & Methods in Physics Research Section a-Accelerators Spectrometers Detectors and Associated Equipment* 591 546-557

[301] Shu H, Zhu P P, Chen B, Liu B, Yin H X, Li E R, Liu Y J, Wang J Y, Yuan Q X, Huang W X, Fang S X, Wu Z Y 2007 Investigation of biomedical inner microstructures with hard X-ray phase-contrast imaging *Nuclear Instruments & Methods in Physics Research Section a-Accelerators Spectrometers Detectors and Associated Equipment* 580 610-613

[302] Bomford C K, Kunkler I H (2002) Walter & Miller's textbook of radiotherapy: Radiation physics, therapy and oncology. Churchill Livingstone, Edinburgh, New York

[303] Pagot E, Fiedler S, Cloetens P, Bravin A, Coan P, Fezzaa K, Baruchel J, Hartwig J 2005 Quantitative comparison between two phase contrast techniques:

diffraction enhanced imaging and phase propagation imaging *Physics in Medicine and Biology* 50 709-724

[304] Parham C, Zhong Z, Connor D M, Chapman L D, Pisano E D 2009 Design and implementation of a compact low-dose diffraction enhanced medical imaging system *Academic Radiology* 16 911-917

[305] Faulconer L, Parham C, Connor D M, Zhong Z, Kim E, Zeng D L, Livasy C, Cole E, Kuzmiak C, Koomen M, Pavic D, Pisano E 2009 Radiologist evaluation of an x-ray tube-based diffraction-enhanced imaging prototype using full-thickness breast specimens *Academic Radiology* 16 1329-1337

[306] Als-Nielsen J, McMorrow D (2001) Elements of modern x-ray physics. John Wiley & Sons Ltd., New York